Dynamics of natural satellites

On the modelling of the influence of tidal effects in natural satellites' dynamics

Master Aerospace Engineering

Soufyan Roubiou

Delft University of Technology

TU Delft

Dynamics of natural satellites

On the modelling of the influence of tidal effects in natural satellites' dynamics

by

Soufyan Roubiou

Student Name	Student Number
Soufyan Roubiou	4954866

Supervisor:	D. Dirkx
Secondary Supervisor:	S. Fayolle
Project Duration:	December, 2023 - November, 2024
Faculty:	Faculty of Aerospace Engineering, Delft

Cover: Canadarm 2 Robotic Arm Grapples SpaceX Dragon by NASA under CC BY-NC 2.0 (Modified)

Style: TU Delft Report Style, with modifications by Daan Zwaneveld

TU Delft

Preface

After 20 years of studying, this thesis is the culmination of all I have worked for. Just like that, a huge chapter of my life is closing and a new one is starting.

I want to thank my supervisor, Dominic, for his invaluable input, assistance and guidance throughout this work. Without your creative ideas, insightful discussions and support this work would not have been what it is. I also want to thank my second supervisor, Sam, for his invaluable insights and extensive feedback on all my work. While it was a lot to work through, I could not have asked for someone better to guide me through the difficulties and intricacies I encountered along the way, which were many more than expected... I cannot express in words how much I learned from you two, and how much it shaped my way of thinking and working. I am excited to see what you come up with when continuing with this topic!

I am also deeply grateful to all my friends in Amsterdam and Delft for their continued support throughout this journey, and helping me take my mind off working when it was necessary. I will never forget the beautiful memories that were formed in Japan and Korea.

Last, and definitely not least, I want to thank my family and parents for their continued support and unconditional love. They are the reason I was provided opportunities they did not have in their childhood, and I hope they can be proud of what I achieved. A special shoutout to my little brother, Adam, who could take my mind off this work like no other and has always been able to make me laugh.

All praise to God.

Soufyan Roubiou
Delft, November 2024

Abstract

It is a well-known fact that the Moon is receding from the Earth due to tidal interactions between the two bodies (if other Solar System bodies were to be neglected). What is less well-known, but just as interesting, is the long-term evolution of planetary systems, especially for icy moons such as those of Jupiter and Saturn. Future missions like JUICE and Europa Clipper will yield extremely accurate radio-science measurements, resulting in possibly better orbit determination and physical parameter estimation. This would however require more accurate dynamical models. To model the long-term evolution of planetary systems properly, and get consistent estimates of related physical parameters (e.g. tidal dissipation parameters) from spacecraft tracking data, it is imperative to ensure that the modelling of the orbit, rotation and tidal deformation of tidally-locked satellites is entirely consistent. Currently used models, however, cannot ensure this.

In order to analyse the effect of tides on a planetary system's orbital evolution, this work propagates the dynamics of the Earth-Moon system in two different ways. A first - simplified and 'uncoupled' - manner, and the current-day standard in the field of natural satellites' dynamics, concurrently propagates the translational and rotational dynamics, while modelling the influence of tidal effects as a tidal force. This model works fine to model the dynamics of natural satellites, but fails when trying to model the full dynamics of spacecrafts too, resulting in possible inconsistencies in the estimation of physical parameters. Hence, a second manner, introduced by Correia et al. (2014) and novel for the field of natural satellites' dynamics, is introduced. This 'coupled' model offers a complete and consistent of a satellite's orbit, rotation and tidal deformation of its gravity field, automatically ensuring consistency between the dynamics of natural satellites and spacecrafts. The first part of the results focuses on analysing the difference between these two solutions in terms of position and Keplerian elements.

A second part of the results considers the evolution of gravity field coefficients and tidal parameters of the body and the evolution of the semi-major axis a and eccentricity e of the orbit due to the influence of tides. The results of both models are compared against each other and against approximations found in literature. Notably, the coupled model performs well for the tides raised on the Moon by itself, dissipating the right amount of orbital energy and predicting values for the evolution of a and e in agreement with the simplified, uncoupled model, although tidal dissipation manifests itself differently. This work finds that the time-variations in the gravity field coefficients cause tidal dissipation, whereas the 'static' part of the coefficients causes tidal dissipation in simplified, uncoupled approaches. This demonstrates the suitability of the proposed coupled implementation for future missions, which has the advantage of circumventing most of the practical and theoretical limitations of the uncoupled model.

Contents

List of Figures

Nomenclature

Symbols

Symbol	Definition
m	Mass.
U	Gravitational potential.
R	Radius.
$\boldsymbol{\omega}$	Angular velocity vector.
$\boldsymbol{r}$	Position vector.
n	Mean motion.
a	Semi major axis.
e	Eccentricity
$\bar{C}_{l,m}$	Normalized cosine coefficients of degree l and order m.
μ	Gravitational parameter.
$\ddot{\boldsymbol{r}}$	Acceleration.
$\boldsymbol{I}$	Inertia tensor.
Γ	Torque.
$\boldsymbol{q}$	Rotation quaternion.
$\boldsymbol{R}$	Rotation matrix.
δ	Rotation angle.
M	Mean anomaly.
ν	True anomaly.
$k_{l,m}$	Love number of degree l and order m.
Q	Quality factor.
τ_e	Maxwell relaxation time.
τ_l	Global relaxation time.
T	Tidal forcing period.
Δt	Tidal time lag.

1

Introduction

Throughout developments in physics and astronomy, dynamical models have been developed to accurately determine the positions of natural satellites, from Newton's laws of motion in his Principia to the current dynamical models used for ephemerides estimations by, for example, NASA's Jet Propulsion Laboratory (e.g., Park et al. 2021). Ephemerides are created by combining dynamical models with observations from scientific instruments, such as instruments on-board of satellites and ground-based tracking stations and telescopes (e.g., Fienga et al. (2019); Park et al. (2021); Fayolle et al. (2023)). Accurate natural satellite ephemerides carry importance with it for scientific missions; knowing the positions of celestial bodies currently, and, more importantly, knowing where they *will* be at a later time, is relevant for mission design (for example, for flyby's) and orbit navigation of satellites. Furthermore, ephemerides provide information about the formation and evolution of planetary systems (e.g., Dirkx et al. (2016); Lainey et al. (2007); Lainey et al. (2012); Folkner et al. (2014)) by extracting key information on the orbital evolution of planetary systems and the properties of the bodies in it, such as their composition, interior structure and rheology. As technological improvements lead to more accurate observations and new methods for observations get developed, such as discussed in Dirkx et al. (2019), the accuracy of these observations increase. Ideally, the dynamical model's error will be well below the error of the observations, resulting in improved statistical significance and consistency of ephemerides. If the dynamical model's error would be at the same level of the observations, it would be hard to validate its statistical significance as there is no way to confidently state whether the error is caused by the dynamical model or the observations.

Celestial bodies are not completely rigid. As a result, a body experiences deformations due to differential gravitational forces from other bodies and centrifugal forces due to its own rotation. These deformations cause small variations in the gravity field of the relevant bodies generating internal friction, which results in dissipation of orbital and rotational energy; this is known as tidal dissipation, which drives the orbital migration of natural satellites and also influences their rotation, and thus plays a crucial role in planetary system evolution. The impact of tidal deformations on the orbital and rotational dynamics are also referred to as the tidal dynamics of a system. They are parts of the dynamical modelling of celestial bodies that can still be improved upon.

Up until now, various developments throughout history have seen the tidal dynamics be modelled in various ways: Kant (1754) noted that tidal dissipation is a real effect that would slow the Earth's rotation, from which Darwin started modelling the dissipation and used a Fourier expansion for the tidal potential (Darwin (1880)). Bodies do not instantly deform under this gravitational forcing; rather, it takes time for them to deform due to their viscoelastic properties. This 'delay', while varying throughout the orbit of a satellite, can be approximated by a constant 'time lag' depending on simplifying, and much disputed, assumptions(e.g., Efroimsky et al. 2013). Kaula (1964) extended this to allow frequency dependence of the tidal lag.

Current dynamical models often numerically integrate only the translational dynamics, while using pre-defined models for the rotational dynamics and/or using simplified formulations for the tides; they are *uncoupled*. For example, Dirkx et al. (2019) couples the translational and rotational part, but leaves out the tides by assuming a rigid body. Another example is Lari (2018), where they only integrate the translational part of the model and model the rotation with a kinematic solution a priori and the tides

are included with a simplified formulation. These simplified approaches have been preferred so far, because the errors of the underlying dynamical models remained well below the errors of observations. They are however limited in their use. By using a simplified expression for the tides - which depends on the rotation rate -, it and the rotation of a satellite are not consistently modelled. Any inconsistency will break the conservation of angular momentum, generating a secular along-track drift. To circumvent this issue, Murray et al. (1999) uses a simplified expression for the tides independent of the rotation rate. While this has been a very useful strategy until now for natural satellites, it raises issues for future missions. This model is applicable to natural satellites, but fails to properly model the dynamics acting on a spacecraft by neglecting the tidal influence of the moon's varying gravity field on the spacecraft. In order to obtain good estimates of tidal dissipation parameters from these missions, it is vital to consistently model the influence of the moon's orbit as well as the moon's varying gravity field on the spacecraft; this is not possible with the current, simplified approaches, but calls for a coupled modelling approach of the orbit, rotation and tidal deformation of the gravity field.

To this end, Correia et al. (2014) modelled the instantaneous change in the gravity field coefficients using a differential equation, where the celestial bodies are assumed to have a certain rheology (i.e. how the body responds to applied forces). Boué et al. (2016) extends this model to a more general formulation to create a fully consistent model capable of concurrently integrating the translational and rotational dynamics while accounting for tidal deformation of the gravity field. This model is a suitable candidate for a more accurate, and general, dynamical model. Correia et al. (2014) and Boué et al. (2016) only test this model for long-term evolution and outside the solar system. For planetary landers and missions, short-term evolutions of synchronous (tidally-locked) satellites are much more interesting, as it is these moons missions like JUICE and Europa Clipper will be sensitive to.

Hence, it is beneficial to apply the coupled model on a shorter timescale to systems closer to home. In this work, the Earth-Moon system will be investigated using the coupled model. The tidal parameters for the Moon are determined quite well (e.g., Lainey 2016) and thus serves as a good test case to validate the coupled model, next to gaining additional insights from the coupled model. Furthermore, since the coupled model does not have limiting underlying assumptions, the model can easily be extended to other planetary systems regardless of the specifics of the orbit (ecccentricity and inclination of the orbit, rotation rate of satellite, etc.), making the specifics of the planetary system considered less relevant to a certain extent, and the general manifestation of tidal dissipation more so. Numerically integrating the rotational equations of motion gives rise to rotational normal modes, which arise due to the internal properties, but have long been damped for Solar System bodies. As a result, it is imperative to damp these normal modes when using the coupled model to initialize a realistic initial state. Concluding, this work provides an extensive analysis of the coupled model applied to the Earth-Moon system, with and without perturbations, with the goal of determining to which extent it is a worthwhile improvement of current dynamical models in light of future missions.

1.1. Research questions

Following the discussion raised in the introduction, the following main research question is set up:

- What is the effect of using a fully coupled model compared to current-day models in natural satellites' dynamics modelling in planetary systems?

In order to facilitate the research and provide structure to the work, the following subquestions have been formulated:

- Can proper initialization reliably be achieved for the system(s) in question?
- What are the effects for an unperturbed and perturbed system of the tides raised on the primary as predicted by the coupled model?
- What are the effects for an unperturbed and perturbed system of the tides raised on the secondary as predicted by the coupled model?

1.2. Thesis outline

The thesis is structured in as follows: Chapter 2 will contain the literature study performed at the start of the thesis, along with the thesis planning made at this point in time - unmodified and with a short discussion comparing it to how the thesis actually went. Chapter 3 contains a stand-alone paper highlighting

the main research and discussing the results. Lastly, Chapter 4 answers the research question(s) and formulates recommendations based on the results obtained in this work. Complementary appendices are included, discussing material that was not deemed suitable to be included in the main content.

2

Literature Study

2.1. Introduction

The goal of this literature study is not to answer the research question. Rather, it will serve as a basis in order to dive into implementing the coupled model for (part of) the systems described before with the eventual goal of creating more accurate dynamical models than what is available right now. To this end, the literature study is structured as follows: Section 2.2.1 will describe the translational dynamics that govern the translational motion of celestial bodies. Section 2.2.2 will discuss the rotational dynamics that govern the rotation of celestial bodies. Section 2.3 will describe current-day methods and literature approximations commonly used to to model the influence of tidal effects on the dynamics of planetary systems. Section 2.4 will introduce the coupled model and will set up a full set of equations of motion governing the translational, rotational and tidal dynamics of celestial bodies. Finally, Section 2.5 will discuss methods of verification, validation and testing the coupled model by comparing it against literature approximations and current-day approximations such as in Section 2.3, as well as testing it for unique edge cases. Lastly, Section 2.6 shows the thesis planning as was created at the end of the literature study, and will also discuss how this played out in reality.

2.2. Dynamical model

In this chapter, a natural satellite's translational and rotational dynamics are described using equations of motions. Most natural satellites in the solar system are caught in synchronous rotational states (e.g., Murray et al. 1999). This allows for a-priori kinematic descriptions to be introduced, circumventing the need to numerically integrate the orientation of a natural satellite using torques. Small deviations from these states - referred to as librations - will also be discussed.

This chapter first introduces some nomenclature that will be used throughout the rest of this work, proceeding with defining a two-dimensional formulation for the equations of motion applicable to a planet and its moon. This will then be extended to a more general three-dimensional formulation allowing for perturbations. Finally, the chapter concludes with an analysis of the kinematic description of the rotation and librations.

2.2.1. Translational dynamics

Nomenclature

The motion of the Earth and the Moon will be described with respect to the other; if the Moon is propagated, a quasi-inertial reference frame will be centered on the Earth and vice versa. The orientation of this reference frame, known as *J2000*, is based on the Earth's equator and equinox, with the x-axis pointing along the vernal equinox, the z-axis pointing along the Earth's rotation vector as it was at the epoch of J2000 and the y-axis completing the frame. Each body is also assigned a body-fixed reference frame, with its origin at the center of mass and its axes aligned with the principal axes of inertia, with the z-axis aligned with the axis of maximal inertia. In the remainder, vectors may be expressed in any of these reference frames.

A vector $\boldsymbol{x}$ going from a body i to a body j in the body-fixed frame of i is expressed as $\boldsymbol{x}_{ij}$. Similarly,

a vector going from j to i in the body-fixed frame of j is expressed as $\boldsymbol{x}_{ji}$. A subscript i in the gradient ∇_i indicates that the gradient is taken with respect to coordinates associated with the body-fixed frame of body i, thus requiring a rotation matrix $\boldsymbol{R}^{I/i}$ to convert results to a common, inertial frame. Lastly, a gradient in the inertial reference frame is written as ∇.

Gravity field modelling

Following Correia et al. (2014), a simplified Earth-Moon system is considered with no perturbations. Consider a body-fixed reference frame $(\boldsymbol{I}, \boldsymbol{J}, \boldsymbol{K})$ centered on body i, where $\boldsymbol{K}$ is the axis of maximum inertia, the largest of the three principle axes of inertia of a rigid body. It is assumed that the rotation rate Ω of the body is along $\boldsymbol{K}$ and that $\boldsymbol{K}$ is orthogonal to the orbital plane, implying zero obliquity (i.e. the equatorial plane and the orbital plane coincide). The setting of this problem is displayed in Fig. 2.1 and discussed in Correia et al. (2014). Note that the inertial frame and body-fixed frame have the same origin.

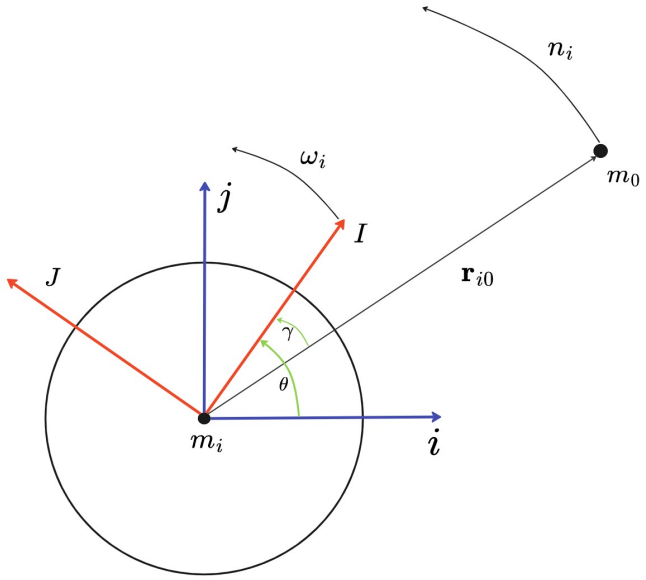

Figure 2.1: Schematic overview of the extended two-body problem with central body 0 and satellite i. The reference frames $\boldsymbol{F_I} = (\boldsymbol{i}, \boldsymbol{j}, \boldsymbol{k})$ and $\boldsymbol{F_i} = (\boldsymbol{I}, \boldsymbol{J}, \boldsymbol{K})$ are introduced, where $\boldsymbol{F_i}$ is fixed to body i and rotating with angular velocity $\boldsymbol{\omega}_i$. $\boldsymbol{r}_{i0}$ is the position vector going from i to 0, n_i is the mean motion of body 0 in the frame of body i and θ and γ are the rotation angle between the reference frames and the angular direction of body 0 as seen from F_i respectively.

In the following equations, U_k is the gravitational potential of body k and is expressed using spherical harmonic expansions. This gravitational potential U_k can, outside its smallest circumscribing sphere, be expressed such that (e.g., Dirkx et al. 2019)

$$U_k(\boldsymbol{r}) = U_k(r, \vartheta, \phi) = \frac{\mu_k}{r} \sum_{l=0}^{\infty} \sum_{m=0}^{l} \left(\frac{R_k}{r} \right)^l P_{l,m} \sin(\phi) (C_{l,m}^k \cos(m\vartheta) + S_{l,m}^k \sin(m\vartheta)). \tag{2.1}$$

r, ϑ and ϕ are the distance to the origin, the body-fixed longitude and body-fixed latitude of the position vector $\boldsymbol{r}$. They express the position at which the potential is evaluated in a body-fixed frame attached to body k in spherical coordinates. μ_k and R_k are the gravitational parameter and the reference radius of body k. $P_{l,m}$ are the associated unnormalized Legendre polynomials of degree l and order m and $C_{l,m}^k$ and $S_{l,m}^k$ are the associated unnormalized cosine and sine coefficients. The spherical harmonic expansion can also be written in terms of normalized coefficients. Then, $C_{l,m}^k = \bar{C}_{l,m}^k \bar{N}_{l,m}$, $S_{l,m}^k = \bar{S}_{l,m}^k \bar{N}_{l,m}$ and $\bar{P}_{l,m} = P_{l,m} \bar{N}_{l,m}$ with (e.g., Dirkx et al. 2019)

$$\bar{N}_{l,m} = \sqrt{\frac{(2 - \delta_{0,m})(2l + 1)(l - m)!}{(l + m)!}}, \tag{2.2}$$

where $\delta_{0,m}$ is the Kronecker delta, equal to 1 if $m = 0$ and 0 otherwise. The $m = 0$ coefficients $C^k_{l,0}$ (the $S^k_{l,0}$ coefficients do not exist as $m = 0$ gives $\sin(0) = 0$) are sometimes expressed as *zonal* coefficients:

$$J^k_l = -C^k_{l,0} = -\bar{C}^k_{l,0}\sqrt{2l+1}. \tag{2.3}$$

The normalized coefficients $\bar{C}^k_{l,m}$ and $\bar{S}^k_{l,m}$ are related to the internal density distribution through (e.g., Lambeck 1988):

$$\begin{pmatrix} \bar{C}^k_{l,m} \\ \bar{S}^k_{l,m} \end{pmatrix} = \frac{1}{M_k(2l+1)} \int_{V_k} \rho_k(r,\phi,\vartheta) \left(\frac{r}{R_k}\right)^l \bar{P}_{l,m}(\sin(\phi)) \begin{pmatrix} \cos(m\vartheta) \\ \sin(m\vartheta) \end{pmatrix} dV, \tag{2.4}$$

where the integral is taken over the volume of the complete body and $\rho_k(r,\phi,\vartheta)$ describes the internal density at those coordinates.

It is common to truncate the spherical harmonic expansion to a degree l_{max}. For the problem at hand, the chosen l_{max} is two, as for most natural satellites (such as the Galilean moons) only the degree 2 gravity field coefficients are known. They furthermore also have the largest contribution aside from the point mass contribution. Lastly, their effects are crucial to incorporate accurately when modelling tides, as the $S_{2,2}$ coefficient has a similar effect on orbital migration of natural satellites as tidal dissipation (see section 2.4). For $l_{max} = 2$, the body is considered an oblate ellipsoid. The terms for $l = 1$ drop off provided that the body-fixed reference frame is centered on the center of mass of the body, which will be assumed to be the case (Murray et al. (1999)). The $l = 1$ terms describe the deviation of the body's mass distribution from the body-fixed center; if the reference frame is centered on the center of mass, then by definition it is symmetrically distributed about this point and thus $C_{1,m}$ and $S_{1,m}$ are equal to 0. Furthermore, $S_{2,1}$ and $C_{2,1}$ are equal to 0 when the body has a rotational symmetry about its polar axis, which is assumed to be the case. Similarly, $S_{2,2}$ is also equal to 0 when the equatorial axes of the body-fixed reference frame align with the equatorial principal axes of inertia; it represents asymmetry in the mass distribution relative to the equatorial plane. If there is no such asymmetry, it is 0 by definition. However, due to $S_{2,2}$ and tidal dissipation having very similar signatures in natural satellites' dynamics, this coefficient is still included. This will be elaborated upon in section 2.4.

For the simplified situation depicted in Fig. 2.1 and assuming the above assumptions, the following simplified expression for the gravitational potential $U_i(\boldsymbol{r})$ holds for a body i:

$$U_i(\boldsymbol{r}) = \frac{\mu_i}{r} - \frac{\mu_i R_i^2 J_2^i}{r^3} P_{2,0}(\sin(\phi)) + \frac{\mu_i R_i^2 P_{2,2}(\sin(\phi))}{r^3}(C^i_{2,2}\cos(2\vartheta) + S^i_{2,2}\sin(2\vartheta)). \tag{2.5}$$

Assuming the body-fixed latitude at which the potential is evaluated is equal to 0 (i.e., natural satellite with zero inclination), this can be further simplified to (e.g. Correia et al. (2013); Correia et al. (2014))

$$U_i(\boldsymbol{r}) = \frac{\mu_i}{r} + \frac{\mu_i R_i^2 J_2^i}{2r^3} + \frac{3\mu_i R_i^2}{r^3}(C^i_{2,2}\cos(2\vartheta) + S^i_{2,2}\sin(2\vartheta)). \tag{2.6}$$

Note that this requires the secondary body (i.e., the body that exerts a force on the oblate ellipsoid) to be a point mass. This is a reasonable simplification because the figure-figure interactions can be considered sufficiently small for the purpose at hand; that is to create a dynamical model fulfilling the accuracy requirements created by development of new measurement techniques (e.g., Lainey et al. (2007), Dirkx et al. (2016)).

Translational equations of motion

Fundamentally, the acceleration exerted on body 0 by the gravitational potential of body i in a common inertial frame can be described by Newton's second law:

$$\ddot{\boldsymbol{r}}_{i0} = R^{I/i}\nabla_i U_i(\boldsymbol{r}_{i0}), \tag{2.7}$$

where $\ddot{\boldsymbol{r}}_{i0}$ is the second time-derivative of $\boldsymbol{r}_{i0}$. Assuming the potential as defined in Eq. 2.5, $\ddot{\boldsymbol{r}}_{i0}$ then evaluates to (e.g., Correia et al. 2014)

$$\ddot{\boldsymbol{r}}_{i0} = R^{I/i}\cdot(-\frac{\mu_i}{r_{i0}^2}\hat{\boldsymbol{r}} - \frac{3\mu_i R_i^2}{2r_{i0}^4}J_2^i\hat{\boldsymbol{r}} - \frac{9\mu_i R_i^2}{r_{i0}^4}(C^i_{2,2}\cos 2\gamma_0 - S^i_{2,2}\sin 2\gamma_0)\hat{\boldsymbol{r}} + \frac{6\mu_i R_i^2}{r_{i0}^4}(C^i_{2,2}\sin 2\gamma_0 + S^i_{2,2}\cos 2\gamma_0)\boldsymbol{K}\times\hat{\boldsymbol{r}}), \tag{2.8}$$

where the substitution $\vartheta = -\gamma$ has been performed, where $\mu_i = Gm_i$, $\hat{\boldsymbol{r}}$ is the radial unit vector and $\hat{\boldsymbol{\gamma}} = \boldsymbol{K} \times \hat{\boldsymbol{r}}$ is the tangential unit vector, both in the body-fixed frame.

The acceleration in Eq. 2.8 is the acceleration the extended body k exerts on the point mass j. In practice, both bodies are extended, in which case the acceleration of an extended body j due to gravitational interaction with an extended body k is given as (e.g., Lainey et al. 2004)

$$\ddot{\boldsymbol{r}}_{kj} = \ddot{\boldsymbol{r}}_{\bar{k}\bar{j}} + \ddot{\boldsymbol{r}}_{\hat{k}\bar{j}} + \ddot{\boldsymbol{r}}_{\bar{k}\hat{j}} + \ddot{\boldsymbol{r}}_{\hat{k}\hat{j}}, \tag{2.9}$$

where the bar and hat notations indicate the contributions of the center of mass and extended gravitational potential terms of a body to the acceleration respectively. The first two terms thus describe the acceleration of body k's point mass and extended body on body j, while the third term accounts for the acceleration due to interaction of point mass k with extended body j. The fourth term describes the figure-figure interaction between both extended bodies. As mentioned before, they can be safely neglected for this application and are generally left out in natural body dynamics (e.g., Lainey et al. (2007), Dirkx et al. (2016), Magnanini et al. (2024)). Rewriting the third term using Newton's third law to $\ddot{\boldsymbol{r}}_{\bar{k}\hat{j}} = -\frac{\mu_j}{\mu_k}\ddot{\boldsymbol{r}}_{\hat{j}\bar{k}}$ then yields (e.g., Dirkx et al. 2016)

$$\ddot{\boldsymbol{r}}_{kj} = \ddot{\boldsymbol{r}}_{\bar{k}\bar{j}} + \ddot{\boldsymbol{r}}_{\hat{k}\bar{j}} - \frac{\mu_j}{\mu_k}\ddot{\boldsymbol{r}}_{\hat{j}\bar{k}}. \tag{2.10}$$

Eq. 2.10 holds for an inertial origin and in general, body k is not an inertial origin. It thus also experiences an acceleration that must be accounted for. In the case that body k exerts an acceleration on body j with the reference frame centered in k, the acceleration is simply $(\ddot{\boldsymbol{r}}_{kj})_k = \ddot{\boldsymbol{r}}_{kj} - \ddot{\boldsymbol{r}}_{jk}$, where the second term takes into account the fact that body j can also apply an acceleration on body k. The resulting acceleration is then given as (e.g., Dirkx et al. 2014):

$$(\ddot{\boldsymbol{r}}_{kj})_k = (\mu_k + \mu_j)\left(-\frac{\hat{\boldsymbol{r}}}{r^2} + \frac{\ddot{\boldsymbol{r}}_{\hat{k}\bar{j}}}{\mu_k} - \frac{\ddot{\boldsymbol{r}}_{\hat{j}\bar{k}}}{\mu_j} \right). \tag{2.11}$$

Consequently, Eq. 2.11 evaluates to Eq. 2.8 with μ_i replaced by $\mu = \mu_i + \mu_0$.

A second, more complex situation arises when the effect of perturbations on the Earth-Moon system are included. This work includes the point mass accelerations exerted on the Earth-Moon system by the Sun and Jupiter. Since the body-fixed latitude at which the potential is evaluated is now not equal to 0, Eq. 2.6 does not hold and Eq. 2.5 must be used to derive the mutual acceleration. It is worth noting that the equations derived in this section are general and do not only hold for the introduced specific case, until the gravitational potential is replaced by a simplified version, such as Eq. 2.6. Substituting Eq. 2.5 into Eq. 2.11 leads to

$$\begin{aligned}\ddot{\boldsymbol{r}} = \frac{-\mu R_i^2}{r^2}\Bigg(&\left(\frac{1}{R_i^2} - \frac{3J_2^i}{r^2}P_{2,0}(\sin(\phi_0)) + \frac{3P_{2,2}(\sin(\phi_0))}{r^2}(C_{2,2}^i\cos(2\vartheta_0) + S_{2,2}^i\sin(2\vartheta_0))\right)\hat{\boldsymbol{r}} \\ &+ \left(\frac{3\sin(\phi_0)\cos(\phi_0)J_2^i}{r^2} + \frac{6\sin(\phi_0)\cos(\phi_0)}{r^2}(C_{2,2}^i\cos(2\vartheta_0) + S_{2,2}^i\sin(2\vartheta_0))\right)\hat{\boldsymbol{\phi}} \\ &- \left(\frac{2P_{2,2}(\sin(\phi_0))}{r^2\cos(\phi_0)}(-C_{2,2}^i\sin(2\vartheta_0) + S_{2,2}^i\cos(2\vartheta_0))\right)\hat{\boldsymbol{\vartheta}}\Bigg).\end{aligned} \tag{2.12}$$

Third-body accelerations

Having discussed both mutual spherical harmonics and the possibility of having a non-inertial origin, it is also possible that a non-inertial origin is situated on a body j: the acceleration $(\ddot{\boldsymbol{r}}_{i0})_j = \ddot{\boldsymbol{r}}_{i0} - \ddot{\boldsymbol{r}}_{ij}$, which is the acceleration on body 0 due to body i with the frame origin at some other body j, which is now a third-body pertubation. Up until now the Earth-Moon system has been treated as a two body problem. Although a good approximation, more realistic orbits are obtained using more extensive dynamics of the system, which will include third body perturbations. The expressions are easily obtained by switching the necessary subscripts in Eq. 2.11, which can yield the following expression for a third-body pertubation:

$$(\ddot{\boldsymbol{r}}_{i0})_j = -\mu_i \left(\left(\frac{\hat{\boldsymbol{r}}_{i0}}{r_{i0}^2} - \frac{\ddot{\boldsymbol{r}}_{\hat{i}\hat{0}}}{\mu_i} + \frac{\ddot{\boldsymbol{r}}_{\hat{0}\hat{i}}}{\mu_0} \right) - \left(\frac{\hat{\boldsymbol{r}}_{ij}}{r_{ij}^2} - \frac{\ddot{\boldsymbol{r}}_{\hat{i}\hat{j}}}{\mu_i} + \frac{\ddot{\boldsymbol{r}}_{\hat{j}\hat{i}}}{\mu_j} \right) \right). \tag{2.13}$$

Then, a full expression for the acceleration any body k experiences in a planetary system can be given. Consider the case of a moon k orbiting a central body 0 along with other bodies j, the total acceleration exerted on body k can then be given as

$$\ddot{\boldsymbol{r}}_k = R^{I/0} \left((\ddot{\boldsymbol{r}}_{0k})_0 + \sum_j^{j \neq k,0} (\ddot{\boldsymbol{r}}_{jk})_0 \right), \tag{2.14}$$

where a central body 0 exerts an acceleration on body k along with a number of third bodies j. Putting everything together, the acceleration acting on the Moon including perturbations is given by

$$\begin{aligned} \ddot{\boldsymbol{r}} = \frac{-\mu R_i^2}{r^2} \Bigg(& \left(\frac{1}{R_i^2} - \frac{3J_2^i}{r^2} P_{2,0}(\sin(\phi_0)) + \frac{3P_{2,2}(\sin(\phi_0))}{r^2} (C_{2,2}^i \cos(2\vartheta_0) + S_{2,2}^i \sin(2\vartheta_0)) \right) \hat{\boldsymbol{r}} \\ & + \left(\frac{3\sin(\phi_0)\cos(\phi_0) J_2^i}{r^2} + \frac{6\sin(\phi_0)\cos(\phi_0)}{r^2} (C_{2,2}^i \cos(2\vartheta_0) + S_{2,2}^i \sin(2\vartheta_0)) \right) \hat{\boldsymbol{\phi}} \\ & - \left(\frac{2P_{2,2}(\sin(\phi_0))}{r^2 \cos(\phi_0)} (-C_{2,2}^i \sin(2\vartheta_0) + S_{2,2}^i \cos(2\vartheta_0)) \right) \hat{\boldsymbol{\vartheta}} \Bigg) - \sum_j \mu_j \left(\frac{\hat{\boldsymbol{r}}_{ji}}{r_{ji}^2} - \frac{\hat{\boldsymbol{r}}_{j0}}{r_{j0}^2} \right) \end{aligned} \tag{2.15}$$

The translational equations of motion can then be summarized as follows (e.g., Dirkx et al. 2019):

$$\dot{\boldsymbol{x}}_t = \begin{bmatrix} \dot{\boldsymbol{r}}_k \\ \dot{\boldsymbol{v}}_k \end{bmatrix} = \begin{bmatrix} \boldsymbol{v}_k \\ \ddot{\boldsymbol{r}}_k \end{bmatrix}, \tag{2.16}$$

with $\boldsymbol{v}_k$ the velocity of body k and $\ddot{\boldsymbol{r}}_k$ given by Eq. 2.8 or 2.15, depending on the case discussed. Note that all the accelerations discussed depend on $U_k(\boldsymbol{r})$ for each body k. Here, U_k only depends on $\boldsymbol{r}$. In reality, U_k can also be time-dependent. The formulation $U_k(\boldsymbol{r})$ as given in Eq. 2.1 assumes that the internal mass distribution is invariant over time, but this is generally not the case. Changes in mass distribution can be due to various reasons, the biggest of which are rotation of the body (causing flattening) and tidal deformations. These variations in mass distribution are expressed through time-dependency via $C_{l,m}^k$ and $S_{l,m}^k$. After all, they relate to the internal mass (and density) distribution through Eq. 2.4. In order to understand where this time-dependency comes from, it is important to dive into rotational and tidal dynamics, which Sections 2.2.2 and 2.3 will do.

2.2.2. Rotational dynamics

Inertia tensor

The inertia tensor $\boldsymbol{I}$ is a 3×3 symmetric matrix that describes the internal mass distribution relative to an axis of rotation. A convenient set of axes is given by the body-fixed frame, for which the off-diagonal elements of $\boldsymbol{I}$ are 0. The axes of the body-fixed frame correspond to the principal axes of inertia, which are defined by the internal mass distribution. They furthermore pass through the body's center of mass and are oriented such that angular momentum about one axis is not transferred to another. The inertia tensor for an arbitrary mass distribution is defined as (e.g., Dehant et al. 2015):

$$\boldsymbol{I}_k = \int_{V_k} \rho_k(\boldsymbol{r})((\boldsymbol{r} \cdot \boldsymbol{r}) 1_{3\times 3} - \boldsymbol{r} \cdot \boldsymbol{r}^T) dV, \tag{2.17}$$

where the integral is taken over the volume of the complete body k, ρ_k is the density distribution of the body as a function of $\boldsymbol{r}$ and $1_{3\times 3}$ is the 3×3 identity matrix. The separate components of $\boldsymbol{I}$ are typically referred to as:

$$\boldsymbol{I}_k = \begin{pmatrix} I_{xx} & I_{xy} & I_{xz} \\ I_{yx} & I_{yy} & I_{yz} \\ I_{zx} & I_{zy} & I_{zz} \end{pmatrix} \tag{2.18}$$

where the diagonal elements are the moments of inertia and the off-diagonal elements the products of inertia. Since both the inertia and the gravity field coefficients depend on the internal mass distribution per Eq. 2.4 and 2.17, a relationship exists between the inertia tensor components and the degree 2 gravity field coefficients (e.g., Lambeck 1980):

$$\boldsymbol{I}_k = m_k R_k^2 \begin{pmatrix} \frac{C_{20}^k}{3} - 2C_{22}^k & -2S_{22}^k & -C_{21}^k \\ -2S_{22}^k & \frac{C_{20}^k}{3} + 2C_{22}^k & -S_{21}^k \\ -C_{21}^k & -S_{21}^k & -\frac{2C_{20}^k}{3} \end{pmatrix} + \bar{I}_k \mathbf{1}_{3x3}, \tag{2.19}$$

where $S_{2,1}^k = 0$ and $C_{2,1}^k = 0$ given that the inertia tensor is evaluated in the body-fixed frame, in which it is defined to have a rotational symmetry about its polar axis (also see section 2.2.1), and $\bar{I}_k$ is the normalized mean moment of inertia, which is equal to the average value of the diagonal of $\boldsymbol{I}_k$. Hence, knowing the degree 2 gravity field coefficients and the normalized mean moment of inertia uniquely defines the inertia tensor of a body.

Gravitational torque

The main torque driving the rotational evolution of the satellite i is the gravitational torque exerted by the central body 0 on the non-spherical shape of the satellite. For the general case of an extended body k, the gravitational torque exerted by a point mass 0 can be described as

$$\bar{\boldsymbol{\Gamma}}_{0k}^{(k)} = -m_0 \boldsymbol{r}_{k0} \times \left(\nabla_k U_k \left(\boldsymbol{r}_{k0} \right) \right), \tag{2.20}$$

where $\bar{\boldsymbol{\Gamma}}_{0k}^{(k)}$ is the gravitational torque exerted by the point mass body 0 on body k, in the reference frame of body k. Note that if $\boldsymbol{r}_{k0} = 0$, then so is $\bar{\boldsymbol{\Gamma}}_{0k}^{(k)}$, implying that forces acting on the center of mass of a body do not induce torques. For the specific case of the Earth-Moon system with no perturbations applied, $\nabla_k U_k \left(\mathbf{r}_{k0} \right)$ is given by Eq. 2.8. Under these assumptions, one can derive - and it is insightful to do so - an explicit expression for $\bar{\boldsymbol{\Gamma}}_{0k}^{(k)}$. Writing out $\nabla_k U_k \left(\mathbf{r}_{k0} \right)$ gives

$$\bar{\boldsymbol{\Gamma}}_{0k}^{(k)} = -m_0 \boldsymbol{r}_{k0} \times \frac{6\mu_k R_k^2}{r_{k0}^4} (C_{2,2}^k \sin 2\gamma + S_{2,2}^k \cos 2\gamma) \boldsymbol{K} \times \hat{\boldsymbol{r}}_{k0}, \tag{2.21}$$

where the terms pointing along $\hat{\boldsymbol{r}}_{k0}$ are left out, as they would drop off due to the cross product anyway. The cross product $\boldsymbol{r}_{k0} \times (\boldsymbol{K} \times \hat{\boldsymbol{r}_{k0}})$ simplifies with the vector triple product identity to $(\boldsymbol{r}_{k0} \cdot \hat{\boldsymbol{r}}_{k0}) \boldsymbol{K} - (\boldsymbol{r}_{k0} \cdot \boldsymbol{K}) \hat{\boldsymbol{r}}_{k0}$, where the first dot product simply yields r_{k0}, while the second dot product is 0, as by definition $\boldsymbol{K}$ will always be perpendicular to $\boldsymbol{r}_{k0}$ for this case. From this result, Eq. 2.21 simplifies to (e.g., Correia et al. 2014)

$$\bar{\boldsymbol{\Gamma}}_{0k}^{(k)} = -\frac{6Gm_0 m_k R_k^2}{r_{k0}^3} (C_{2,2}^k \sin(2\gamma) + S_{2,2}^k \cos(2\gamma)) \boldsymbol{K}. \tag{2.22}$$

As expected, $\bar{\boldsymbol{\Gamma}}_{0k}^{(k)}$ is perpendicular to the orbital plane and points along the rotation axis of body k. In other words, if the potential is given by Eq. 2.8, which specifically only holds for the situation described in Fig. 2.1, $\bar{\boldsymbol{\Gamma}}_{0k}^{(k)}$ is along the orbital angular momentum vector. Note furthermore that there is no dependency on $C_{2,0}^k$, as this gravity coefficient describes the flattening of the body, which occurs perpendicular to the orbital plane, and hence has no influence on the gravitational torque exerted; it is independent of longitude and dependent on latitude, and since the problem is two-dimensional, the latitude plays no role and hence due to symmetry about the rotation axis it induces no torque. The gravitational torque $\bar{\boldsymbol{\Gamma}}_{0k}^{(k)}$ can also be written as (e.g., Williams et al. 2001):

$$\bar{\boldsymbol{\Gamma}}_{0k}^{(k)} = \frac{3\mu_0}{r_{k0}^5} \boldsymbol{r}_{k0} \times \left(\boldsymbol{I}_k \boldsymbol{r}_{k0} \right), \tag{2.23}$$

where the dependency on the internal mass distribution of body k is now expressed through $\boldsymbol{I}_k$. Here $\bar{I}_k$ drops off, because its dot product with $\boldsymbol{r}_{k0}$ will still point in the direction of $\hat{\boldsymbol{r}}_{k0}$. Working out the cross product in Eq. 2.23 with $\boldsymbol{r}_{k0} = r_I \boldsymbol{I} + r_J \boldsymbol{J}$ gives

$$\bar{\boldsymbol{\Gamma}}_{0k}^{(k)} = \frac{3Gm_0 m_k R_k^2}{r_{k0}^5} (2S_{2,2}^k (r_J^2 - r_I^2) + 4C_{2,2}^k r_I r_J) \boldsymbol{K}, \tag{2.24}$$

where r_I and r_J can be related to γ through the following relations derived from Fig. 2.1 (e.g., Correia et al. 2014):

$$\cos 2\gamma = (\boldsymbol{I}\cdot\hat{r})^2 - (\boldsymbol{J}\cdot\hat{r})^2 \quad \text{and} \quad \sin 2\gamma = -2(\boldsymbol{I}\cdot\hat{r})(\boldsymbol{J}\cdot\hat{r}). \tag{2.25}$$

Using these relations, one finds that $\sin 2\gamma = -2\frac{r_I r_J}{r^2}$ and $\cos 2\gamma = \frac{r_I^2 - r_J^2}{r^2}$, and then, indeed, Eq. 2.22 and Eq. 2.23 are equal.

A second component of the external torque applied on body k is the gravitational torque exerted by the oblateness of body 0. This torque is formally expressed as (e.g., Schutz (1981), Bois et al. (1992), Rambaux et al. (2012)):

$$\boldsymbol{\Gamma}^{(k)}_{0k,J2} = -\int_{M_0'} l_{0k} \times \nabla_k U_k\left(\boldsymbol{r}_{k0}\right)\, dm_0', \tag{2.26}$$

where M_0' represents the distribution of the mass inside body 0 and the integration is performed over its volume and l_{0k} is the distance between the mass element dm_0' and the center of mass of body k. Following Rambaux et al. (2012), this effect is exacerbated at short distances between bodies k and 0 (for example Mars and Phobos), and as distance increases this effect decays quite rapidly. As is visible in Table 7 of Rambaux et al. (2012), for the Mars-Phobos system the impact of the additional source of torque on librations (see Section 3.3) is quite small and only has a significant effect once degree 3 terms are being considered, which they are not in the models discussed in this work. Bois et al. (1992) performed a similar analysis, concluding that the impact of the additional source of torque on librations in the Earth-Moon system has a comparable magnitude to degree 5 terms, albeit with different behaviour. This value is sufficiently small for the general case that the external torque applied on a body k by body 0 can be simplified to Eq. 2.21, thus stating that $\boldsymbol{\Gamma}^{(k)} \approx \bar{\boldsymbol{\Gamma}}^{(k)}_{0k}$.

In the perturbed case, the torques induced by perturbing bodies will behave slightly differently than accelerations. As mentioned before, from Eq. 2.20 it follows that forces acting on the center of mass of a body do not induce torques. Hence, the perturbing bodies will only exert torques on the extended body k, and not on 0's point mass. Analogously to Eq. 2.20, the gravitational torque acting on an extended body k exerted by a point mass 0 and N perturbations is given by

$$\bar{\boldsymbol{\Gamma}}^{(k)}_{0k} = -m_0 \boldsymbol{r}_{k0} \times \left(\nabla_k U_k\left(\boldsymbol{r}_{k0}\right)\right) - \sum_i^N m_i \boldsymbol{r}_{ki} \times \left(\nabla_k U_k\left(\boldsymbol{r}_{ki}\right)\right) \tag{2.27}$$

Quaternions

Generally, extended bodies have an asymmetrical mass distribution, requiring a description of their orientation to properly propagate the rotational equations of motion. Multiple methods are available to do so. In this work, a quaternion $\boldsymbol{q}$ is used to express the orientation of a body because it is singularity-free, whereas, for example, Euler angles do have singularities at the poles. Furthermore, Fukushima (2008) has shown that using quaternions to propagate the rotational dynamics is an optimal choice in terms of numerical error. Note that in this context, a quaternion does not refer to the mathematical concept (e.g., Goldman 2011), but rather as a vector that describes the orientation of the body, where the convention is followed as in Fukushima (2008). Quaternions have also been used before for similar purposes in natural body dynamics (e.g., Dirkx et al. (2019)). The quaternion vector is given as $\boldsymbol{q} = (q_0, q_1, q_2, q_3)$, where, following Altman (1972), q_i are the Euler parameters. In order to ensure numerical stability during integration, the Euler parameters adhere to the following normalization condition:

$$\sum_{i=0}^{3} q_i^2 = 1. \tag{2.28}$$

Following Fukushima (2008), the time derivative of $\boldsymbol{q}$ is given as

$$\dot{\boldsymbol{q}}_k = \boldsymbol{Q}(\boldsymbol{q}_k)\boldsymbol{\omega}_k, \tag{2.29}$$

$$\boldsymbol{Q}(\boldsymbol{q}) = \frac{1}{2}\begin{bmatrix} -q_1 & -q_2 & -q_3 \\ q_0 & -q_3 & q_2 \\ q_3 & q_0 & -q_1 \\ -q_2 & q_1 & q_0 \end{bmatrix}. \tag{2.30}$$

Rotational equations of motion

Fundamentally, the equation of motion that governs the rotation of a rigid body is given in the body-fixed frame by the Euler-Liouville equation:

$$\frac{d}{dt}(\boldsymbol{I}_k\boldsymbol{\omega}_k) + \boldsymbol{\omega}_k \times (\boldsymbol{I}_k\boldsymbol{\omega}_k) = \boldsymbol{\Gamma}_k, \tag{2.31}$$

where $\boldsymbol{\omega}_k$ is the rotation rate of a body k and $\boldsymbol{\Gamma}_k$ the sum of all external torques acting on it. $\boldsymbol{I}_k\boldsymbol{\omega}_k$ defines the angular momentum $\boldsymbol{L}_k$ of the body. The term $\boldsymbol{\omega}_k \times (\boldsymbol{I}_k\boldsymbol{\omega}_k)$ arises from the transport theorem, stating that a derivative taken in a rotating reference frame (which the body-fixed reference frame is) must also account for the rotation of the reference frame itself (e.g., Rao 2006):

$$\frac{d}{dt}\mathbf{f} = \left(\left(\frac{d}{dt}\right)_r + \boldsymbol{\omega}\times\right)\mathbf{f}, \tag{2.32}$$

where $\left(\frac{d}{dt}\right)$ is the rate of change of $\mathbf{f}$ as observed in the body-fixed reference frame. Working out the derivative, Eq. 2.31 evaluates to

$$\dot{\boldsymbol{I}}_k\boldsymbol{\omega}_k + \boldsymbol{I}_k\dot{\boldsymbol{\omega}}_k + \boldsymbol{\omega}_k \times (\boldsymbol{I}_k\boldsymbol{\omega}_k) = \boldsymbol{\Gamma}_k. \tag{2.33}$$

For a rigid body in rotation, $\dot{\boldsymbol{I}}$ evaluates to 0, because it will experience no mass deformations. In practice, celestial bodies experience (small) mass deformations, which in turn result in small rate of changes of $\boldsymbol{I}$. While this simplification can still be made and justified, it will not be done in this work as the bodies considered here will, in later sections, not be considered rigid anymore, at which point it will be of interest to see how a body's deformation influences $\dot{\boldsymbol{I}}$ and through it the rotation rate. Rewriting Eq. 2.31 for $\dot{\boldsymbol{\omega}}_i$ then gives (e.g., Dirkx et al. 2019)

$$\dot{\boldsymbol{\omega}}_i = \boldsymbol{I}_i^{-1} \cdot (\bar{\boldsymbol{\Gamma}}_{0i}^{(i)} - \dot{\boldsymbol{I}}_i\boldsymbol{\omega}_i - \boldsymbol{\omega}_i \times (\boldsymbol{I}_i\boldsymbol{\omega}_i)). \tag{2.34}$$

The rotational equations of motion $\dot{\boldsymbol{x}}_r$ can then be set up:

$$\dot{\boldsymbol{x}}_r = \begin{bmatrix} \dot{\boldsymbol{q}}_i \\ \dot{\boldsymbol{\omega}}_i \end{bmatrix} = \begin{bmatrix} \boldsymbol{Q}(\boldsymbol{q}_i)\boldsymbol{\omega}_i \\ \boldsymbol{I}_i^{-1} \cdot (\bar{\boldsymbol{\Gamma}}_{0i}^{(i)} - \dot{I}_i\boldsymbol{\omega}_i - \boldsymbol{\omega}_i \times (\boldsymbol{I}_i\boldsymbol{\omega}_i)) \end{bmatrix}. \tag{2.35}$$

2.2.3. Librations

Averaged over time, the Moon's rotation rate, as that of many other large (natural) satellites, is synchronous with its mean motion, implying that its rotational and orbital period are equal (e.g., Henrard 2006), also known as a spin-orbit resonance. Such an equilibrium, that is achieved over long timescales, and which follows from the fact that a body's rotation is governed by Eq. 2.35, is known as a Cassini state (Peale (1969)). A perfectly circular orbit would imply that the body-fixed longitude of the central body as seen from the satellite is always zero. However, orbital eccentricities, torques and accelerations exerted by bodies and inclinations of the orbit prevent the satellite's long axis (i.e., principal axis of minimum inertia) from pointing towards the central body at all times; superimposed on the once-per-orbit rotation around its spin axis, these effects cause the satellite to oscillate and wobble around its three axes (e.g., Hoolst et al. 2020). These deviations are known as librations. It is reiterated here that librations are an 'artificial' concept required for a kinematic formulation of the synchronous rotation of a satellite. Concurrently integrating the translational and rotational equations would omit the need of such a formulation, since the underlying dynamics are then numerically integrated, whereas a kinematic description *observes* the motion of a body and then describes it.

Librations can be discerned into two (body-fixed) components: longitudinal and latitudinal librations. Longitudinal librations represent oscillations about the satellite's rotation axis, describing ω's oscillatory deviations around the mean motion (e.g., Hoolst et al. 2020). As a result, the body-fixed longitude of the central body as seen from the satellite is not always zero, but oscillates in the East-West direction in

the satellite's sky. Note that longitudinal libration and body-fixed longitude are thus equal in magnitude. On the other hand, latitudinal librations represent oscillations of the satellite's rotation axis about the body's x- and y-axis. Latitudinal librations are caused by the inclination of an orbit, and for most natural satellites they are small and their effect on the satellite's orbit limited, as it does not influence the rotation rate in such a way that the longitudinal libration does.

As this work is interested in the orbital migration of a satellite over time, the latitudinal librations are of lesser importance. Hence, longitudinal librations will be the focus of this section, following other authors who have done the same (e.g., Rambaux et al. 2010). These librations can be further decomposed into *optical* and *physical* librations. The former is caused due to the geometry of the orbit, specifically the orbit's eccentricity, while the latter can even occur for circular orbits as it is a result of the internal properties of a satellite (e.g., Hurford et al. 2009). The total longitudinal libration λ can then be expressed as

$$\lambda = \phi + \gamma \tag{2.36}$$

with ϕ and γ the optical and physical librations respectively.

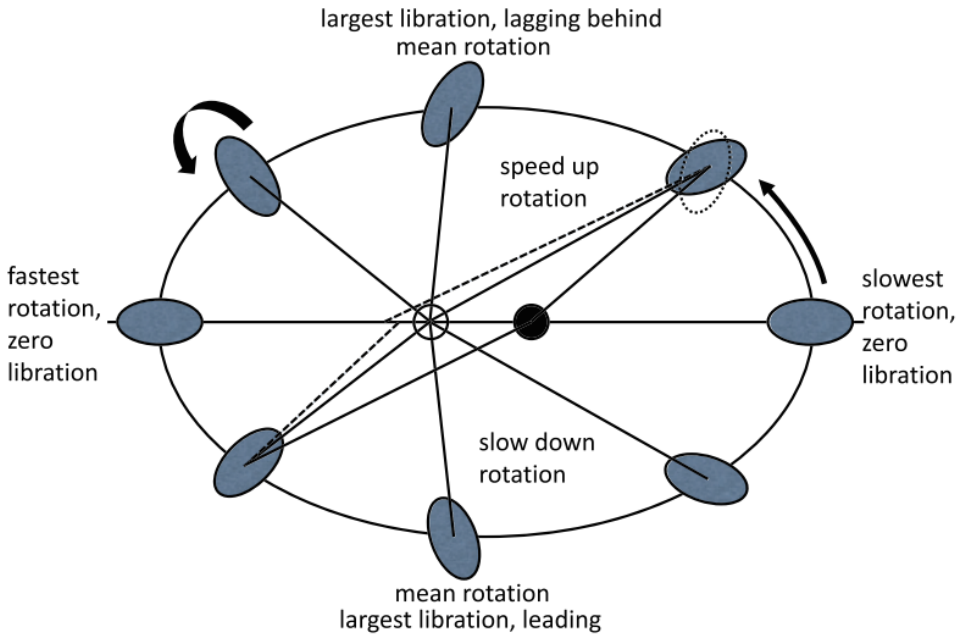

Figure 2.2: A schematic overview of longitudinal libration as displayed and discussed in Hoolst et al. (2020), with the hollow circle the empty focus, the solid circle the central body, the solid lines the equilibrium orientation of the long axis of the satellite, which corrects up to first order towards the empty focus (Murray et al. (1999)), the dashed lines the direction of the long axis of the satellite body at two given mean anomalies and the solid lines indicating the direction of the translation and rotation of the satellite. Note the dotted ellipse at a mean anomaly of 45°, indicating the orientation of one of the periodic tidal bulges, which will be discussed more in Chapter 4. Note that the tidal bulge as well as the librations are highly exaggarated.

Optical libration

Fig. 2.2 gives a schematic representation of how the longitudinal libration can be described by the body's long axis fluctuating around the empty focus (Hoolst et al. (2020)) in such a way that the long axis is always pointing further away from the central body than the direction to the empty focus (e.g., Tiscareno et al. 2009). Assuming pure synchronous rotation and considering the geometrical effects of the eccentricity, the satellite's rotation angle δ can be related to the mean anomaly M through (see Fig. 2.3)

$$\delta = M - \gamma. \tag{2.37}$$

In the absence of physical librations and pure synchronous rotation, the satellite's long axis then seemingly points towards the empty focus of the orbit. This is however only true up to $O(e^2)$ (e.g., Murray et al. 1999), which is one of the reasons this work chooses to concurrently integrate the equations of motion. From Eq. 2.37 the optical libration angle ϕ can be expressed as (e.g., Lainey et al. 2019)

$$\phi = \nu - M = 2e\sin(M) + O(e^3), \tag{2.38}$$

with ν the satellite's true anomaly. While offering a straightforward kinematic expression for the observed behaviour of natural satellites, such approximations are too inaccurate for the accuracy requirements laid out by future missions, and hence show the importance of concurrently integrating the equations of motion for the dynamics of the Earth-Moon system.

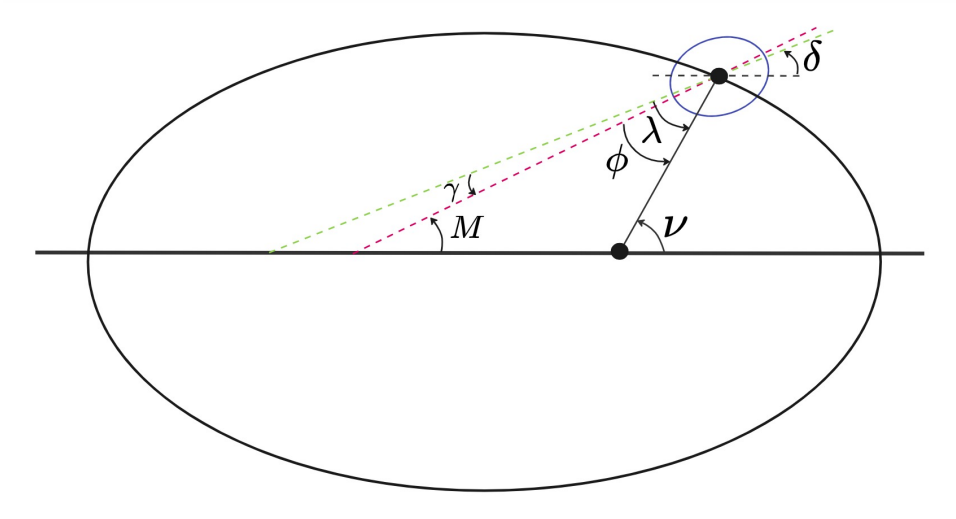

Figure 2.3: A schematic overview of the effect of the physical libration on the pointing direction of the satellite towards the central planet; the dashed lines indicate the inclusion (green) and exclusion (red) of the physical libration respectively. ν and M represent the true and mean anomaly of the orbit, while δ represents the satellite's rotation angle. ϕ and γ are the optical and physical librations respectively.

Physical libration

Physical librations consists of a combination of free and forced librations (e.g., Hurford et al. 2009). Forced librations are caused by external torques acting on the body, while free librations are caused by an internal excitation mechanism, or they have been excited at some point in time but have never been fully damped out. For small libration angles, the rotational equations of motion governing the longitudinal libration can be approximated using a linearized differential equation, giving a first order approximation for the longitudinal libration angle (e.g., Danby (1988); Williams et al. (2001)). The linearized differential equation is given as (Rambaux et al. (2010)):

$$\ddot{\gamma} + 3n^2\sigma\gamma = f, \tag{2.39}$$

with the triaxiality parameter $\sigma = (B - A)/C$ with $A \leq B \leq C$ the principal moments of inertia defined by Eq. 2.19 and reiterated here for convenience:

$$A = -2C_{2,2} - \frac{1}{3}J_2 + \bar{I}, \tag{2.40}$$

$$B = 2C_{2,2} - \frac{1}{3}J_2 + \bar{I}, \tag{2.41}$$

$$C = \frac{2}{3}J_2 + \bar{I}, \tag{2.42}$$

and f the appropriate component of the torque (e.g. the z-component in this case), also called the forcing. A satellite's forced libration responds at the frequency of the forcing (e.g., Hurford et al. 2009). For most satellites, this will likely be at the mean motion n, giving rise to the aforementioned dominant once-per-orbit libration.

Note that in the case when no external torques are applied, e.g. $f = 0$, Eq. 2.39 will still have a solution with frequency ω_0, called the *normal mode* of the system. This is the frequency at which

free librations occur if they have not yet been damped out. In this case, the body's natural resonant frequency ω_0 can be defined as $\sqrt{3n^2\sigma}$ (e.g., Rambaux et al. 2010). The fact that ω_0 is a function of the mean motion and the triaxiality of the body means it says something about the properties of the body itself, since no external forces are in play. Generally, f will not have a closed expression due to the many perturbations acting on a satellite's orbit, moving away from an idealized Keplerian orbit. Instead, following Rambaux et al. (2010) it can be expanded as a Fourier series:

$$f = \sum_i H_i \sin(\omega_i t + \alpha_i), \tag{2.43}$$

with H_i, ω_i and α_i the magnitude, frequency and phase of the oscillations respectively. Assuming the normal modes to have been damped, the inhomogeneous part of the differential equation yields the following solution (Rambaux et al. (2010)):

$$\gamma = \sum_i \frac{\omega_0^2 H_i}{\omega_0^2 - \omega_i^2} \sin(\omega_i t + \alpha_i), \tag{2.44}$$

where the summation over i represent all periodic variations of the orbit over an infinite range of frequencies. An important implication that follows from Eq. 2.44 is the edge case of $\omega_0 \approx \omega_i$, note that if there is such a system where there is a frequency component very close to the normal mode, the solution will blow up. The solution will start to resonate and linearization assumptions may fail to hold. While this is not relevant for the Earth-Moon system, it can be important for bodies if they, for example, have a mean motion with a frequency close to their normal modes.

Up until now, bodies have been assumed to be completely rigid. In reality, this is often not the case; bodies deform under (for example) differential gravitational forces and third body pertubations. A point on a moon facing a planet will experience a slightly larger gravitational pull from the planet than a point on the other side of the moon. This will cause the body to slightly deform, which is called a tidal deformation. An important consequence is that it is vital that a body's rotation (both orientation and rotation rate) is determined accurately, as a slight deviation from the actual rotation rate or orientation would have a similar effect on the moon's orbit as tidal effects. Tidal forces and the time-variability of the mass distribution of bodies will be discussed in depth in Section 2.3.

2.3. Tides

As discussed in last section, the translational and rotational equations provided assumed rigid bodies in their derivations, thus neglecting tidal effects that have an influence on the time-variability of the gravity field of an extended body. Tides drive long-term orbital evolution of natural satellites, and hence are a key part of natural satellite dynamics in the context of future missions. To this end, this section will introduce the concept of the tidal potential and tidal force. Furthermore, the shortcomings of the current model and the effects thereof will be discussed, which will help in providing context for the introduction of the coupled model and help validating it.

2.3.1. Time-variability of the mass distribution

As mentioned briefly at the end of section 2.2, gradients of gravitational potentials induce (slightly) different forces depending on the position in space with respect to this potential. As a result, an extended body will deform slightly under this differential gravitational force. This is most commonly observed in the tides of the oceans induced by the Moon. Similarly, solid bodies also experience tides. The magnitude of the resulting deformation is dependent on the body's properties, such as its rheology (see Section 2.4). Tidal deformations express themselves in variations in the mass distribution, and thus the gravity field, shape and rotation. They can induce a variation in the rotation due to the fact that a changing mass distribution and shape will induce a different torque (which in itself is already highly dependent on the rotation rate) which in turn results in a different rate of change of the rotation rate. It is reiterated that this is why the rotation rate of a body must be determined precisely.

For the body i, the tidal deformations induced by the perturbing body j are determined by the tidal potential $U_j^T(\boldsymbol{r})$ and the so-called tidal Love numbers $k_{l,m}^i$ of i - not to be confused with the Love numbers $h_{l,m}^i$ and $l_{l,m}^i$, which describe the body's deformation under the effects of tides - where l and m are the usual degree and order of the spherical harmonic expansion. Note that the tidal potential is

explicitly different from the gravitational potential as given in Eq. 2.1. The gradient of the tidal potential yields the tidal force, which dictates the relative motion between two points on body i, resulting in tides. The Love numbers, without the subscripts, were first introduced by Love (1911). The subscripts were added later (e.g., Petit et al. 2010). Love numbers translate the body's deformation under tidal forcing to gravity field variations, where the body's deformation depends on a body's interior properties, such as size, temperature, forcing frequency and its rheology (e.g., Efroimsky 2012), and thus are integral parameters to determine the body's gravitational tidal deformation. It is common practice to simplify the Love numbers to k_l (e.g., Zhang (1992); Williams et al. (2015)), because variations of k in m for a set l are typically small. Furthermore, in the general case Love numbers consist of a real and imaginary part (e.g., Williams et al. 2015) which will be discussed in depth later.

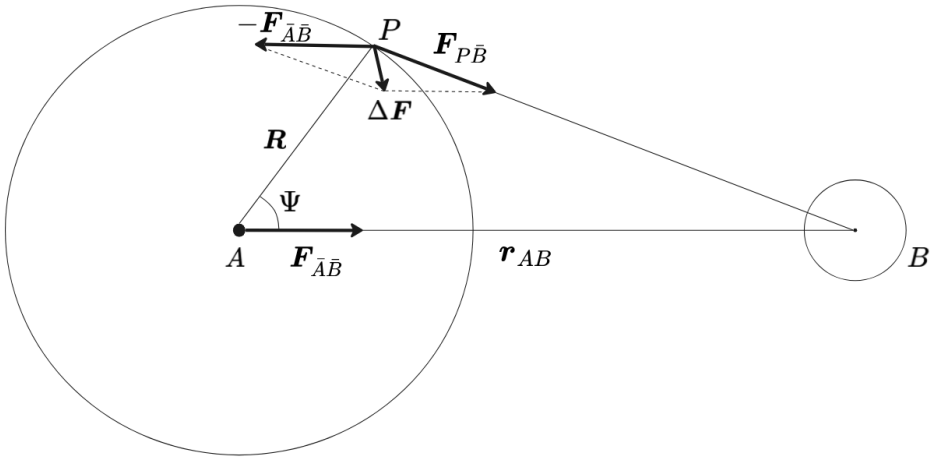

Figure 2.4: Schematic decomposition of the gravitational force exerted by body B, where the difference between $\boldsymbol{F}_{P\bar{B}}$ and $\boldsymbol{F}_{\bar{A}\bar{B}}$ is responsible for the tidal force $\Delta\boldsymbol{F}$. $\boldsymbol{R}$ is the position vector pointing to point P and $\boldsymbol{r}_{AB}$ is the vector connecting the centers of A and B, and Ψ is the angle between $\boldsymbol{R}$ and $\boldsymbol{r}_{AB}$.

Approximating body j as a point mass allows the tidal potential of body j to be given as (See Appendix A) (e.g., Kaula 1964):

$$U_j^T(\boldsymbol{r}) = \frac{Gm_j}{r_{ij}} \sum_{l=2}^{\infty} \left(\frac{|\boldsymbol{R}|}{r_{ij}} \right)^l P_l(\cos(\Psi)), \tag{2.45}$$

where $\boldsymbol{R}$ is a position vector from the center of the body to a surface point and Ψ is the angle beween $\boldsymbol{R}$ and $\boldsymbol{r}_{ij}$, see Fig. 2.4. P_l are the Legendre polynomials of degree l. Any angle Ψ can be expanded into the body-fixed longitude and latitude, allowing Eq. 2.45 to be expanded to the following formulation at $|\boldsymbol{r}| = |\boldsymbol{R}|$ from the body center (Munk et al. (1975)):

$$U_j^T(\boldsymbol{r}) = \sum_{l=2}^{\infty} \sum_{m=0}^{l} U_{j,l,m}^T(\boldsymbol{r}), \tag{2.46}$$

where $U_j^T(\boldsymbol{r})$ is expanded into $U_{j,l,m}^T(\boldsymbol{r})$. The deformations on body i are thus induced by the external tidal potential of body j. The other source of deformation considered in this work is the centrifugal potential of body i itself, caused by its own rotation (e.g., Boué et al. 2016). Any point P on the surface of a rotating body (for simplicity, assume a spherical, rigid planet rotating at an angular rate $\boldsymbol{\omega} = \omega\boldsymbol{K}$), experiences a centrifugal acceleration $\ddot{\boldsymbol{r}}_{cf}$ in both the $\boldsymbol{I}$- and $\boldsymbol{J}$-direction with magnitudes $\omega^2 I$ and $\omega^2 J$ respectively (Murray et al. (1999)). Therefore, any arbitrary point on the surface at position ($\boldsymbol{I}$, $\boldsymbol{J}$, $\boldsymbol{K}$) experiences an additional acceleration

$$\ddot{\boldsymbol{r}}_{cf} = \omega^2(I\boldsymbol{I}, J\boldsymbol{J}) \tag{2.47}$$

in the body-fixed frame. Now, for simplicity consider a global ocean on the surface of body i (note: this was also a core assumption in the derivation of the tide-generated perturbing potential expanded as a Fourier series by Darwin (1880)). In equilibrium, this ocean must lie on an equipotential surface

perpendicular to the net acceleration of body i, which consists of the centrifugal acceleration, among others, resulting in flattening at the poles Murray et al. (1999). Realizing that acceleration is the gradient of the potential then can result in an expression for the centrifugal potential of body i at a point (r, ϑ, ϕ), (Murray et al. (1999), Correia et al. (2013)):

$$U_i^{cf}(\boldsymbol{r}) = -\frac{1}{3}\omega^2 r^2 P_2(\cos(\phi)) = -\frac{1}{3}\omega^2 r^2, \tag{2.48}$$

where ϕ is now the angle between the radius vector and the rotation axis (e.g. different from previous definitions). Note that U_i^{cf} is independent of ϑ, indicating symmetry of the equipotential surface about the rotation axis (Murray et al. (1999)). Note furthermore that since $\phi = 0$, the Legendre polynomial $P_2(\cos(\phi))$ simplifies to 1. The induced gravitational potential on body i, $\delta U_{i,l}(\boldsymbol{r})$, and, when expanded, $\delta U_{i,l,m}(\boldsymbol{r})$ then depends on both $U_i^{cf}(\boldsymbol{r})$ and $U_j^T(\boldsymbol{r})$:

$$\delta U_{i,l,m}(\boldsymbol{r}) = \left(\frac{|\boldsymbol{R}|}{|\boldsymbol{r}|}\right)^{l+1} k_{l,m}^i U'_{l,m}(\boldsymbol{r}) = \left(\frac{|\boldsymbol{R}|}{|\boldsymbol{r}|}\right)^{l+1} k_{l,m}^i (U_{i,l,m}^{cf}(\boldsymbol{r}) + U_{j,l,m}^T(\boldsymbol{r})), \tag{2.49}$$

where $U'_{l,m}$ denotes the total tide-inducing potential acting on body i, body j's tidal potential and body i's centrifugal and induced gravitational potential now depend on the degree l and order m. Notice furthermore that $k_{l,m}^i$ quantifies the magnitude of body i's induced gravitational potential by acting as a proportionality constant. Eq. 2.1 and Eq. 2.46 substituted in Eq. 2.49, neglecting the centrifugal potential, can be expanded into a series, yielding the time-variable spherical harmonic coefficients (e.g., Petit et al. 2010):

$$\Delta\bar{C}_{l,m}^i - i\Delta\bar{S}_{l,m}^i = \frac{k_{l,m}^i}{2l+1} \sum_j \frac{\mu_j}{\mu_i} \left(\frac{R_i}{r_j}\right)^{l+1} \bar{P}_{l,m}(\sin\phi_j) e^{-im\vartheta_j}, \tag{2.50}$$

where the summation runs over j bodies that raise a tide on body i, but can easily be simplified to one body. Eq. 2.50 describes the evolution of the $C_{l,m}^i(t)$ and $S_{l,m}^i(t)$ coefficients of a body i under the tidal influence of j other bodies.

The time-variability of the mass distribution is expressed through the gravity field coefficients $C_{l,m}^i(t)$ and $S_{l,m}^i(t)$, where they are now both dependent on time. For (almost) synchronous bodies, the coefficients consist of a large static component and a small varying component, where $C_{l,m}^i(t)$ and $S_{l,m}^i(t)$ can be decomposed as $C_{l,m}^i(t) = C_{l,m}^{i,0} + \Delta C_{l,m}^i$ and $S_{l,m}^i(t) = S_{l,m}^{i,0} + \Delta S_{l,m}^i$, giving rise to a large permanent tide and a relatively small varying tide, since θ and ϕ are constant to first-order approximation. For synchronously rotating bodies specifically, this effect is, as mentioned before, quite small; deviations from the rotation rate due to librations result in the variations. Hence, measuring varying tides is more difficult for synchronously rotating bodies than it is for non-synchronously rotating bodies.

2.3.2. Tidal force formulation

Since $U_j^T(\boldsymbol{r})$ scales with $\frac{R}{r_{ij}}$, with R the radius of body j, and generally $r_{ij} >> R$, (there exist exceptions, such as the Mars-Phobos system), rapid convergence of the series is guaranteed. Furthermore, from Eq. 2.1 it follows that degree 2 terms will have the largest contribution, as the potential scales with $\frac{1}{r^l}$. Limiting the tidal force (which follows from the tidal potential) to degree 2 is common practice in dynamical studies of natural satellites (e.g., Lainey et al. (2007), Lari (2018)), though it must be noted that for the Moon k_3 is observable (e.g., Konopliv et al. (2013), Lemoine et al. (2013)). Then, degree two Love number k_2 will represent the total variation of the degree two gravity field and by extension the entire truncated gravity field (The gravity field is already limited to $l = 2$ in section 2.2). The resulting deformation results in two tidal bulges, one pointing towards body j and one on the other side of body i, see Fig. 2.5. Generally, this is a good approximation, but it is important to realize that spherical asymmetries can cause variations in the degree two Love numbers (Bills et al. (2005)). Since these variations are however small and difficult to track (e.g., Konopliv et al. 2011), it is common practice to assume that $k_{2,0} \approx k_{2,1} \approx k_{2,2} \approx k_2$ and work with k_2 instead.

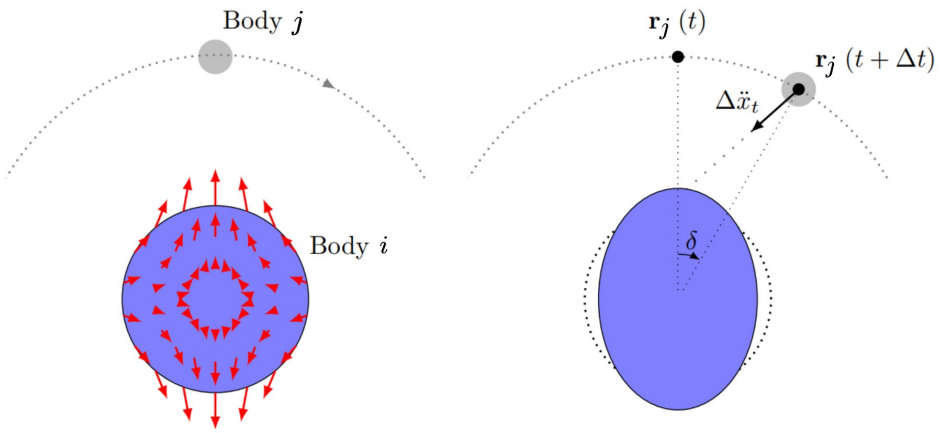

Figure 2.5: Left: Schematic overview of tide-generating body j and the tidal deformation of body i. Right: Time-lag between pertubing potential and the raised tide on body i, quantified by a lag angle δ. This gives raise to an additional acceleration $\Delta\ddot{x}_t$ exerted on j by the induced gravitational potential of i. This figure has been adopted from Dirkx (2015).

The response to the perturbing potential as in Fig. 2.5 is the actual tidal deformation. This tidal deformation generates an additional tidal potential as in Eq. 2.49, which again exerts an influence on body j. In reality, body i's response to this perturbing potential is not instantaneous, but rather, it takes time for it to deform due to its viscosity; its response is visco-elastic. As a result, the tidal bulge raised by the perturbing potential does not exactly point along the vector $\boldsymbol{r}_{ij}$. Instead, there will be a so called time-lag between the perturbing potential and the raised tide, which in turns gives raise to a tidal geometric lag angle δ. An exaggerated depiction is shown in Fig. 2.5.

This effect is commonly expressed through a quality factor Q, which is defined as (e.g., Khan et al. 2004):

$$Q_i^j = \frac{|k_2^i|}{\mathrm{Im}(k_2^i)}, \tag{2.51}$$

where $\mathrm{Im}(k_2^i)$ specifies the imaginary part of k_2^i. It was briefly mentioned before that Love numbers consist of a real and imaginary part. The imaginary part quantifies the tidal lag δ, resulting in tidal dissipation. Q is frequency-dependent and depends on the body's rheology, and is used to signify what a body's tidal response may look like (e.g. it defines the amount of energy dissipated in the system) (e.g., Efroimsky et al. 2007). Q_i^j then denotes the quality factor of body i at the forcing frequency of the tides raised by body j. For a full and consistent modelling of the tidal response, however, bodies would have to be assigned rheologies to properly extract tidal parameters, especially given the frequency-dependence of Q. This will be elaborated upon in Section 2.4. The time lag in raising the tidal bulge due to the visco-elastic response is dependent on Q and given as (e.g., Lainey et al. 2007):

$$\Delta t_i^j = \frac{T_i^j \sin^{-1}(1/Q_i^j)}{2\pi}, \tag{2.52}$$

where Δt_i^j is the time lag and T_i^j refers to the period of the forcing. For the tides raised on the central body 0 by the satellite i, T_i^j depends on the satellite's orbital and rotational period, T_i^{orb} and T_i^{rot} respectively, where

$$T_i^{orb} = \frac{2\pi}{n_i} \tag{2.53}$$

$$T_i^{rot} = \frac{2\pi}{\omega_i}, \tag{2.54}$$

resulting in (e.g., Lainey et al. (2007), Efroimsky et al. (2007))

$$T_0^i = \frac{T_i^{orb} T_i^{rot}}{2|T_i^{rot} - T_i^{orb}|} = \frac{2\pi}{2|\boldsymbol{\omega}_i - \boldsymbol{n}_i|}, \tag{2.55}$$

which is the time that the satellite takes to pass from a point over the planet to its antipode (e.g., Lari 2018). For the tides raised on a synchronous satellite, the tidal forcing period is simply

$$T_i^0 = \frac{2\pi}{n_i}. \tag{2.56}$$

Due to this time lag, an additional torque is exerted on both bodies. Depending on whether body i's mean motion is smaller or greater than body 0's rotation rate, the tidal bulge is raised in front or behind the vector connecting both bodies, resulting in an along-track acceleration or deceleration respectively. In turn, this additional torque results in body 0's rotation rate decreasing or increasing, and finally, by conservation of angular momentum, increasing or decreasing body i's semi-major axis respectively. This also explains why the Moon is slowly drifting away from the Earth (e.g., Krasinsky 2002).

A time lag also has a consequence for the induced gravitational potential on a body. As mentioned before, Eq. 2.49 makes the implicit assumption that body i is 'elastic', meaning that any stress applied to it instantly deforms the body, indicating no time lag and an instantaneous response. Since there is a time lag between the perturbing potential and the tide raised, past perturbations (more specifically, deformations caused by past perturbations) must be taken into account to accurately determine the induced gravitational potential at time t. Assuming that the body's tidal response is linear (e.g. no higher order terms are considered) and isotropic in its body-fixed frame (e.g., Boué et al. 2016) (more details about how a body reponds to an applied stress are discussed in Section 2.4), one can state that body i's induced gravitational potential at time t, $\delta U_i(\boldsymbol{r}, t)$ (note the explicit time-dependence now) depends linearly on all past tidal pertubations with $t' \leq t$, $U_0^{'}(\boldsymbol{r}, t')$, giving raise to a convolution (e.g., Boué et al. 2016):

$$\delta U_i(\boldsymbol{r}, t) = \sum_{l=2}^{\infty} \delta U_{0,l}(\boldsymbol{r}, t) \tag{2.57}$$

$$= \sum_{l=2}^{\infty} \left(\frac{|\boldsymbol{R}|}{|\boldsymbol{r}|}\right)^{l+1} k_l(t) * U_{0,l}^{'}(\boldsymbol{r}, t) \tag{2.58}$$

$$= \sum_{l=2}^{\infty} \left(\frac{|\boldsymbol{R}|}{|\boldsymbol{r}|}\right)^{l+1} \int_{-\infty}^{t} k_l(t - t') U_{0,l}^{'}(\boldsymbol{r}, t') \mathrm{d}t', \tag{2.59}$$

where the ratio $\left(\frac{|\boldsymbol{R}|}{|\boldsymbol{r}|}\right)^{l+1}$ comes from the Dirichlet theorem for external potential if $|\boldsymbol{r}| > |\boldsymbol{R}|$ (Souchay et al. (2013)), where $\boldsymbol{r}$ is the position vector from the center of body i to the point at which the potential is calculated. Consequently, the external potential drops off very fast as a function of distance. Comparing Eq. 2.58 to Eq. 2.49, it is apparent that Eq. 2.58 is a generalization that allows for a more realistic representation of tidal responses. Note that Eq. 2.49 follows from Eq. 2.58 if one assumes that for $t' < t$, $U_0^{'}(\boldsymbol{r}, t') = 0$. Note that if the potential is considered at the surface, $|\boldsymbol{r}| = |\boldsymbol{R}|$ and the ratio becomes equal to 1. Eq. 2.58 can be limited to degree 2:

$$\delta U_i(\boldsymbol{r}, t) = \left(\frac{|\boldsymbol{R}|}{r}\right)^{3} \int_{-\infty}^{t} k_2(t - t') U_{0,2}^{'}(\boldsymbol{r}, t') \mathrm{d}t', \tag{2.60}$$

$$U_{0,2}^{'}(\boldsymbol{r}, t') = U_i^{cf}(\boldsymbol{r}) + U_{0,2}^{T}(\boldsymbol{r}) = -\frac{1}{3}\omega^2(t) r^2 + \frac{G m_0}{r_{i0}} \left(\frac{|\boldsymbol{R}|}{r}\right)^{3} \left(\frac{|\boldsymbol{R}|}{r_{i0}}\right)^{2} P_2(\cos(\Psi)) \tag{2.61}$$

where $k_l(t)$ is a Love distrbution as described by Efroimsky (2012) such that $k_l(t) = 0 \forall t > 0$ (e.g. causality is ensured). Similar to Love numbers, the Love distribution is also a property of the body through its dependence on the internal structure and composition (e.g., Boué et al. 2016). It is essentially a distribution of proportionality constants that scale the perturbing potentials at times $t' < t$ to the tidal potential at time t. Given that the perturbing potential is already determined in Eq. 2.45 and 2.48, only the Love distribution needs to be the determined in order to derive an expression for the induced tidal potential.

The simplest model possible (apart from an instantaneous response) would be to consider a constant time lag, meaning that the induced tidal potential at time t is generated by a perturbing potential at $t - \Delta t$, with Δt the time lag (e.g., Efroimsky et al. 2013). The Love distribution is then given as $k_l(t) = k_l \delta(t - \Delta t)$, with $\delta(t)$ the Dirac-Delta function. Current day ephemeris determination express the tidal potential induced due to the tidal deformation through the direct tidal force F_i^j, which, when reduced to degree $l = 2$, as discussed before, is given as (see Appendix A) (e.g., Lainey et al. 2007):

$$\boldsymbol{F}_i^0 = -\frac{3Gm_i k_2^0 R_i^5}{|\boldsymbol{r}_{i0}|^8}\left(r + \Delta t_0^i\left(\boldsymbol{r}_{i0}\times\boldsymbol{\omega}_0 + \boldsymbol{v}_i + \frac{2}{|\boldsymbol{r}_{i0}|^2}(\boldsymbol{r}_{i0}\cdot\boldsymbol{v}_i)\boldsymbol{r}_{i0}\right)\right) \tag{2.62}$$

for the tides raised on the central body 0 by the satellite i, where $\boldsymbol{v}_i$ denotes the velocity vector of body i. By Newton's third law, the bulge raised on the satellite will also affect its own orbit, with the magnitude of the force being same but the direction opposite of the force in Eq. 2.61:

$$\boldsymbol{F}_i^i = -\frac{3Gm_0 k_2^i R_i^5}{|\boldsymbol{r}_{i0}|^8}\left(\boldsymbol{r}_{i0} + \Delta t_i^0\left(\boldsymbol{r}_{i0}\times\boldsymbol{\omega}_i + \boldsymbol{v}_i + \frac{2}{|\boldsymbol{r}_{i0}|^2}(\boldsymbol{r}_{i0}\cdot\boldsymbol{v}_i)\boldsymbol{r}_{i0}\right)\right). \tag{2.63}$$

While Eq. 2.63 can in principle be applied to model the tides raised on the satellite by its own tidal bulge, there is a consideration to be taken into account. In order to rewrite Eq. 2.63 into a more convenient form, it is assumed that $\boldsymbol{\omega} = \omega\boldsymbol{K}$. Note that this assumption breaks down in the case perturbations are added. Under this assumption, $\boldsymbol{v}_i$ can be decomposed into its radial and tangential components such that (e.g., Hut 1981):

$$\boldsymbol{F}_i^i = -\frac{3Gm_0 k_2^i R_i^5}{|\boldsymbol{r}_{i0}|^7}\left(\left(1 + 3\Delta t_i^0\frac{2}{|\boldsymbol{r}_{i0}|^2}(\boldsymbol{r}_{i0}\cdot\boldsymbol{v}_i)\boldsymbol{r}_{i0}\right)\hat{\boldsymbol{r}} + \Delta t_i^0(\dot{\theta}_i - \omega_i)\hat{\boldsymbol{\phi}}\right), \tag{2.64}$$

where $\dot{\theta}_i$ is the angular velocity of the satellite. The benefit of rewriting the tidal force like this is twofold: first of all, it decomposes the tidal force into a radial and tangential component, respectively known as the radial and librational tides. Second, the dependency on the difference between $\dot{\theta}_i$ and ω_i is made explicit, which will be convenient when discussing the effect of tidal torques on the satellite's orbit. Note that Eq. 2.64 also makes it explicit that, if $\dot{\theta}_i = \omega_i$, the tangential component of the tidal force equals zero. Hence, satellites that are in a circular, synchronous orbit do not experience librational tides.

Eq. 2.63 can be simplified by following Murray et al. (1999), who state that the librational tides dissipate exactly 4/3 times as much energy as the radial tides. Then, in order to determine the tidal force raised by the satellite, this detail is used to simplify the calculation (e.g., Lari 2018). The tidal force due to the radial tides is retrieved by substituting $\boldsymbol{\omega}_i = \boldsymbol{r}_{i0}\times\boldsymbol{v}_i/|\boldsymbol{r}_{i0}|^2$ in Eq. 2.63

$$\boldsymbol{F}_{i,rad}^i = -\frac{3Gm_0 k_2^i R_i^5}{|\boldsymbol{r}_{i0}|^8}\left(\boldsymbol{r}_{i0} + \Delta t_i^0\left(\frac{3}{|\boldsymbol{r}_{i0}|^2}(\boldsymbol{r}_{i0}\cdot\boldsymbol{v}_i)\boldsymbol{r}_{i0}\right)\right), \tag{2.65}$$

where this component is now considered to be the tidal force induced by the radial component of the tides. Adding 4/3 times this force from the librational component results in

$$\boldsymbol{F}_i^i = -\frac{3Gm_0 k_2^i R_i^5}{|\boldsymbol{r}_{i0}|^8}\left(\boldsymbol{r}_{i0} + \Delta t_i^0\left(\frac{7}{|\boldsymbol{r}_{i0}|^2}(\boldsymbol{r}_{i0}\cdot\boldsymbol{v}_i)\boldsymbol{r}_{i0}\right)\right). \tag{2.66}$$

The beauty in this simplification lies in that this formulation does not depend on the rotation rate of the satellite anymore as it does in Eq. 2.63 and 2.64. Since the modelling of the tides raised on the satellite due to itself is extremely sensitive to the rotation rate, as will follow from the discussion in the remainder of this section, Eq. 2.66 is an attractive alternative to model the satellite's natural dynamics and is done so in both ephemeris and natural satellite dynamics studies (e.g., Lainey et al. (2007), Lari (2018)). It is furthermore relatively straightforward to implement and computationally cheaper than the alternative, which is using an appropriate rheology model. Since ephemeris studies usually have shorter timescales, this model is, despite its simplifications, a suitable model to use for modelling tidal responses.

However, for long-term dynamical modelling, this fails to hold. Since the orbit expands or shrieks due to tidal dissipation, as mentioned earlier, the frequency of the tidal forcing, and thus Q_i^j, will change, which is apparent from analyzing the expression in Eq. 2.52. As a result, the amount of tidal energy the system will dissipate also changes over time. This, combined with the fact that Eq. 2.66 is already a simplification itself, calls for the need of a more sophisticated model to properly model the frequency-dependency of the tidal forcing, as well as the body's response to this forcing, on longer timescales. This will be discussed in more depth in Section 2.4.

The additional torque induced by the tidal bulge raised on the satellite influences the rotational dynamics of the system (more specifically, it induces a transfer in energy and angular momentum between the two bodies), and can be expressed as:

$$\boldsymbol{\Gamma}_i^i = \boldsymbol{r}_{i0} \times \boldsymbol{F}_i^i = -\frac{3Gm_i k_2^0 R_i^5}{|\boldsymbol{r}_{i0}|^8} \Delta t((\boldsymbol{r}_{i0} \cdot \boldsymbol{r}_{i0})\boldsymbol{\omega}_i - \boldsymbol{r}_{i0}(\boldsymbol{r}_{i0} \cdot \boldsymbol{\omega}_i) - \boldsymbol{v}_i|\boldsymbol{r}_{i0}|^2 + \boldsymbol{r}_{i0} \times \boldsymbol{v}_i). \tag{2.67}$$

This is the torque that is generated due to the lag angle previously mentioned. It gives rise to a change in $\boldsymbol{\omega}_i$ while simultaneously also depending on $\boldsymbol{\omega}_i$. This again reiterates the importance of accurately modelling the rotation rate of the satellite for accurate propagation of the satellite's dynamics.

These expressions will be useful in the process of verifying and validating the results of the coupled model introduced in Section 2.4. To incorporate the effect of tides into the dynamics of the system, the tidal acceleration following from Eq. 2.61 can simply be added to the translational equations of motion derived in Section 2.2.1. Similarly, adding or subtracting this additional torque from the rotational equations of motion described in Section 2.2.2 incorporates the tidal effect into the rotational dynamics.

With all this in mind, it is clear that the incorporation of tidal dynamics into the equations of motion is important in order to accurately perform long-term propagations of natural satellites. Current state-of-the-art methods used rely on severe simplifications (e.g., Efroimsky et al. 2013) and rely on consistently modelling the rotation rate of the satellite and tides raised on the satellite, which proved to be difficult to do for synchronously rotating bodies (see section 2.3.1). Furthermore, they are unable to properly capture the body's frequency-dependent response to tidal forcing, as well as how it evolves over time, by implicitly assuming a static Q_i^j. To this end, it may be beneficial to instead model the gravity field coefficients as a differential equations, and introduce a fully coupled model between the translational, rotational and tidal dynamics.

2.4. Coupled model

In the previous section, the direct tidal force is introduced, which approximates the effect of the tides on the translational and rotational dynamics. In this section, a new way ('new' for the field of natural satellites' dynamics) of incorporating the tides will be introduced; a differential equation that governs the evolution of the gravity field coefficients is introduced, removing the need for a direct tidal force expression. Through this differential equation the translational and rotational dynamics are influenced, directly incorporating any influence tides would have on the dynamics of the relevant bodies. The problems mentioned in last section, such as the extreme sensitivity of the tidal force expressions to the rotation rate of the satellite, the approximations necessary to apply it to the satellite's dynamics, are circumvented using this method, while it also allows for a more complete modelling of the body's frequency-dependent response to tidal forcing over long timescales.

2.4.1. Rheology

A core assumption made in deriving the translational and rotational equations of motion in section 2.2.2. is that all bodies were assumed to be rigid. Solar system bodies are of course not rigid and deform under the presence of forces, which has been accounted for in section 2.3. by introducing tides, which allows for the variation of the gravity field coefficients $C_{l,m}^k(t)$ and $S_{l,m}^k(t)$ through Eq. 2.50. As mentioned repeatedly, using the tidal force to express tides is an approximation (e.g., Efroimsky et al. 2013) and to properly model the response of a body to tidal forcing an adequate rheology model is necessary. A rheology model is a way to model the body's deformation and response to any stresses applied.

One way of doing this is by adopting a linear model where the phase lag is proportional to the tidal frequency: a *viscous* model (e.g., Correia et al. 2014). The downside of adopting this model is that, circling back to the discussion about the rotation rate in section 2.3, the ratio between the rotational and orbital period will have an excess proportional to the eccentricity squared (e.g., Mignard (1979), Fayolle (2025)), with the aforementioned pseudo-synchronous rotation as a result. From observations of solar system satellites, it is however known that most are in a synchronous orbit, and as discussed in section 2.3, one way to get to this realization is by assuming an additional torque due to a small shift in the pointing vector of the moon (e.g., Colombo (1965), Goldreich et al. (1966), Fayolle (2025)).

With this in mind, a more realistic approach is laid down by Correia et al. (2014), where for natural satellites in a spin-orbit resonance, such as the Moon and the Galilean moons, a *viscoelastic* model is used to model their response to stress. Viscoelastic materials are materials that exhibit both viscous and elastic properties when undergoing a deformation induced by a stress; the material resists deformation linearly with time when a stress is applied (a viscous response), but it also immediately deforms

under a stress and goes back to its original response when the stress is removed (an elastic response). Whether the body responds as a viscous fluid or elastic solid then depends on the frequency of the perturbation (e.g., Correia et al. 2014). Viscoelastic rheologies have been used before in the context of natural satellites' dynamics, since they are able to reproduce the main features of tidal dissipation, providing a good basis for developing the coupled model (e.g., Correia et al. (2014), Boué et al. (2016), Henning et al. (2009)). One of the simplest forms is to consider that the body behaves like a Maxwell material (e.g., Correia et al. 2014), i.e., the material is represented by a purely viscous damper and a purely elastic spring connected in series (e.g., Turcotte et al. 2002).

The Maxwell model relies on the assumption that the bodies are modelled as homogeneous. A complete modelling of the tides would consider the variation in layers that bodies usually have, as well as consider full three-dimensional stress and strain tensors to compute tides as a function of the longitude and latitude (e.g., Peale et al. (1978), Segatz et al. (1988), Henning et al. (2009)). The Maxwell model is, however, good enough to describe the main features of tidal evolution (e.g., Henning et al. (2009), Correia et al. (2014)). With this in mind, it is reiterated that the Maxwell model is well suited for bodies that are in spin-orbit resonance, such as the Moon.

An alternative to the Maxwell model is the Andrade model (Andrade (1910)). The Andrade model can be thought of as the Maxwell model with an extra term describing the hereditary reaction of strain to stress (Efroimsky (2012), Correia et al. (2014)). Efroimsky (2012) describes the rheology of a planet using an empirical power scaling law for the phase lag consistent with accumulated geophysical, seismological, and geodetic observational data (Mitchell (1995), Stachnik et al. (2004), Shito et al. (2004)), where the results show that the best fitted laws are in conformity with the Andrade model. Despite these results, the Andrade model is not used in this work, as it is extremely complex and the main features of the tidal dissipation are similar to other viscoelastic models such as the Maxwell model (e.g., Correia et al. 2014), which makes the Maxwell model a good first choice for the rheology of a satellite in spin-orbit resonance.

The Maxwell model has been used numerous times before to describe a planetary body's structure and its response to forces applied to it (e.g. Correia et al. (2014), Ferraz-Mello (2015), Boué et al. (2016)), making it a relatively well known and established model. Following Turcotte et al. (2002), the Maxwell model describes the body's response by the following relation (e.g., Henning et al. 2009):

$$\frac{d\epsilon}{dt} = \frac{1}{\mu_0}\frac{d\sigma}{dt} + \frac{\sigma}{\eta}, \tag{2.68}$$

which describes the body's response by a purely viscous damper with viscosity η and a purely elastic spring with modulus μ_0 connected in series, with ϵ the strain and σ the stress applied to the body. The body's response is dependent on the frequency of the forcing, which can have a frequency in either the fully elastic or viscous regimes, or the transient regime between these two (e.g., Bagheri et al. 2022). So, if a stress with a frequency in the elastic regime is applied, the body instantly deforms dependent on μ_0. If this stress is removed, the body instantly returns to its equilibrium shape. On the other hand, if the stress has a frequency in the viscous regime, the body will act like a viscous damper and will ensure a linear deformation rate dependent on η. If this stress is removed, the deformation is held in place and the body will over time return to its equilibrium shape. When these components are connected in parallel instead of in series, the generalized model of a solid Kelvin-Voigt material is generated (Christensen (1971)). The main difference between these models is that a Kelvin-Voigt material will not instantly deform under applied stresses, making it rather unsuitable for modelling tidal deformations. A more extensive discussion is provided in Henning et al. (2009).

2.4.2. Gravity field coefficients in a differential equation

This section will now look at deriving a differential equation for the tidal potential, from which a differential equation for the gravity field coefficients can be derived. The following derivations will follow the methods laid out in Correia et al. (2014) and Boué et al. (2016). The convolution in Eq. 2.59 is very general, only assuming that the body's response is linear and isotropic in its body-fixed frame (e.g. Remus et al. (2012), Boué et al. (2016)). When a body's response is assumed to behave like a Maxwell model, e.g. the planet is considered to be a homogeneous viscoelastic body with Maxwell rheology, one can simplify the convolution by transforming the equation into the Fourier domain, yielding a point-wise multiplication:

$$\delta U_i(\boldsymbol{r},\nu) = k_l(\nu) U'_{0,l}(\boldsymbol{r},\nu). \tag{2.69}$$

Under these assumptions, the Love distribution $k_l(\nu)$ with frequency ν is of the form (e.g., Henning et al. (2009), Boué et al. (2016)):

$$k_l(\nu) = k_l^0 \frac{1 + i\tau_e \nu}{1 + i\tau_l \nu}, \tag{2.70}$$

where k_l^0 is the fluid Love number of degree l. For a homogeneous incompressible viscous sphere it holds that $k_l^0 = 3/2(l-1)$, but in general k_l^0 depends on the internal differentiation of the body and can be obtained from the Darwin-Radau equation (e.g., Jeffreys (1976), Correia et al. (2014)), which relies on several assumptions to derive its result:

$$k_l^0 = 5\left(1 + \left[\frac{5}{2} - \frac{15C}{4mR^2}\right]^2\right)^{-1} - 1, \tag{2.71}$$

with m the mass of the body, R its equatorial radius and $C = (2/3J_2 + \bar{I})mR^2$ its principal moment of inertia, which is the moment along the $\boldsymbol{K}$-axis. $\tau_e = \eta/\mu_0$ is the elastic or Maxwell relaxation time and the global relaxation time τ_l is defined as (e.g., Boué et al. 2016)

$$\tau_l = (1 + A_l)\tau_e \tag{2.72}$$

with (e.g., Boué et al. 2016):

$$A_l \tau_e = \frac{3\left(2l^2 + 4l + 3\right)\eta}{4\pi G \rho^2 R^2} \tag{2.73}$$

the fluid relaxation time, with η the viscosity and ρ the density of the body. τ_e, τ_l and A_l all say something about time it takes for the body to respond to applied stresses. It then follows from Eq. 2.70 that, if $\tau_e = \tau_l = 0$, the body's response is instantaneous (e.g., Correia et al. 2014). The obtained potential under this condition is the so-called equilibrium potential. It also must be stressed that τ_l as defined only holds for a homogeneous incompressible viscous sphere. In reality, many celestial bodies are stratified and τ_l and τ_e become parameters that have to be fitted to reproduce the response of more complex internal structures (e.g., Peltier (1974), Boué et al. (2016)).

Given the Fourier transform of $k_l(t)$ as in Eq. 2.70, the convolution in Eq. 2.59 can be transformed into a first order differential equation (see Appendix A of Correia et al. (2014)). This results in a differential equation for the l-th term of the induced gravitational potential as in Eq. 2.59 (Correia et al. (2014)):

$$\delta U_l + \tau_l \delta \dot{U}_l = k_l^0 (U'_l + \tau_e \dot{U}'_l). \tag{2.74}$$

Here the induced potential δU is again caused by the perturbing tidal potential U', where U' is as defined in Eq. 2.49. Eq. 2.74 shows that when $\tau_l = \tau_e = 0$, the raised potential reduces to an equilibrium potential δU_l^e - i.e. the response is instaneneous or there is a static perturbation - defined as (e.g., Correia et al. 2014):

$$\delta U_l^e = k_l^0 U'_l. \tag{2.75}$$

Substituting Eq. 2.75 in Eq. 2.74 then expresses the instanteneous variation of the induced potential as a function of the equilibrium potential:

$$\delta U_l + \tau_l \delta \dot{U}_l = \delta U_l^e + \tau_e \delta \dot{U}_l^e. \tag{2.76}$$

The relaxation times τ_l and τ_e can be related to k_2 and Q as introduced in section 2.3 - for $l = 2$, so it follows that τ_l simplifies to τ_2 - and (Correia et al. (2014)):

$$k_2 = k_2^0 \sqrt{\frac{1 + \tau_e^2 \chi^2}{1 + \tau_2^2 \chi^2}}, \tag{2.77}$$

$$\tan\left(\arcsin\left(\frac{1}{Q}\right)\right) = \tan\delta = \frac{(\tau_2 - \tau_e)\chi}{1 + \tau_2\tau_e\chi^2}, \tag{2.78}$$

$$\frac{k_2}{Q} = k_2^0 \frac{(\tau_2 - \tau_e)\chi}{1 + (\tau_2\chi)^2}. \tag{2.79}$$

From Eq. 2.76, it follows that $\delta = 0$ for $\chi = 0$ and $\chi \to \infty$, while its maximum value is obtained for $\chi = \sqrt{\tau_2\tau_e}$, implying that a perturbation with no frequency (e.g. no perturbation) or an infinite frequency (e.g. a static perturbation) do not result in phase lags. Since $\tau_l = (1 + A_l)\tau_e$, and $A_l > 0 \forall l$, it follows that $\tau_l > \tau_e \forall l$, indicating that k_2 is monochromatically decreasing per Eq. 2.77 (Correia et al. (2014).

The differential equation as defined in Eq. 2.76 governs the instantaneous change in the induced gravitational potential that follows from any perturbing potential. Consequently, the change in the gravity field coefficients is also governed by this equation since any variations in the induced gravitational potential follow from these coefficients. Since these gravity field coefficients are decomposed in spherical harmonics and the spherical harmonic functions form an orthogonal basis, the differential equation as defined for the full induced potential must also hold for the gravity field coefficients, thus yielding (e.g., Correia et al. 2014):

$$J_2 + \tau_l \dot{J}_2 = J_2^e + \tau_e \dot{J}_2^e, \tag{2.80}$$

$$C_{2,2} + \tau_l \dot{C}_{2,2} = C_{2,2}^e + \tau_e \dot{C}_{2,2}^e, \tag{2.81}$$

$$S_{2,2} + \tau_l \dot{S}_{2,2} = S_{2,2}^e + \tau_e \dot{S}_{2,2}^e. \tag{2.82}$$

For convenience, these differential equations can also be noted down as one equation by introducing the notation (e.g., Correia et al. 2014):

$$Z_{l,m} = C_{l,m} - iS_{l,m} \quad \text{and} \quad Z_{l,m}^e = C_{l,m}^e - iS_{l,m}^e. \tag{2.83}$$

Since the differential equation holds for $C_{l,m}$ and $S_{l,m}$, it will also hold for any linear combination of them, thus (e.g., Boué et al. 2016):

$$Z_{l,m} + \tau_l \dot{Z}_{l,m} = Z_{l,m}^e + \tau_e \dot{Z}_{l,m}^e, \tag{2.84}$$

where $Z_{l,m}^e$ is the coefficient at equilibrium. Following Ferraz-Mello (2015) and Boué et al. (2016), Eq. 2.84 can be conveniently reordered to

$$Z_{l,m} = \left(1 - \frac{\tau_e}{\tau_l}\right) Z_{l,m}^\nu + \frac{\tau_e}{\tau_l} Z_{l,m}^e, \quad \text{with} \quad Z_{l,m}^\nu + \tau_l \dot{Z}_{l,m}^\nu = Z_{l,m}^e, \tag{2.85}$$

ensuring that there is no more dependency on $\dot{Z}_{l,m}^e$. As will be shown shortly, $\dot{Z}_{l,m}^e$ can contain parameters that are not straightforward to calculate and may rely on (numerical) approximations. Thus, Eq. 2.84 and Eq. 2.85 are completely equal and both represent the instantaneous variation of the gravity field coefficients, but Eq. 2.85 is somewhat easier to implement.

Note that this differential equation, inherently describing the induced tidal potential, only depends on the body's own rotation vector and the position of the perturbing body, meaning that Eq. 2.85 should hold for any trajectory (both 2-dimensional and 3-dimensional - the formulation of the perturbing potential simply differs); whether it be chaotic, periodic or highly eccentric (Boué et al. (2016)), as long as the initial conditions are valid (see section 2.4). Similarly to Eq. 2.76, the equilibrium coefficient $Z_{l,m}^e$ is given for a static perturbation or instantaneous response, suggesting that the induced gravitational potential simplifies to Eq. 2.60 and the equilibrium coefficients are then fully defined by Eq. 2.50, which is reiterated here for the unnormalized gravity field coefficients:

$$\Delta\bar{C}_{l,m}^i - i\Delta\bar{S}_{l,m}^i = \frac{k_{l,m}^i}{2l+1} \sum_j \frac{\mu_j}{\mu_i} \left(\frac{R_i}{r_j}\right)^{l+1} \bar{P}_{l,m}(\sin\phi_j) e^{-im\vartheta_j}, \tag{2.86}$$

For the J_2, $S_{2,2}$ and $C_{2,2}$ coefficients, it then follows that their equilibrium values are given as (e.g., Correia et al. 2013):

$$J_2^e = k_2^0 \left[\frac{\omega_i^2 R_i^3}{3\mu_i} + \frac{1}{2}\frac{m_0}{m_i}\left(\frac{R_i}{|\boldsymbol{r}_{i0}|}\right)^3 \right], \tag{2.87}$$

$$C_{2,2}^e = k_2^0 \frac{m_0}{4m_i}\left(\frac{R_i}{|\boldsymbol{r}_{i0}|}\right)^3 \cos(2\gamma_0), \tag{2.88}$$

$$S_{2,2}^e = -k_2^0 \frac{m_0}{4m_i}\left(\frac{R_i}{|\boldsymbol{r}_{i0}|}\right)^3 \sin(2\gamma_0), \tag{2.89}$$

and for their time derivatives, respectively (e.g., Correia et al. 2014):

$$\dot{J}_2^e = k_2^0 \left[\frac{2\omega_i^2 R_i^3}{3\mu_i}\dot{\omega}_i - \frac{3}{2}\frac{m_0}{m_i}\left(\frac{R_i}{|\boldsymbol{r}_{i0}|}\right)^3 \frac{\dot{\boldsymbol{r}}_{i0}\cdot\boldsymbol{r}_{i0}}{r_{i0^2}} \right], \tag{2.90}$$

$$\dot{C}_{2,2}^e = -k_2^0 \frac{m_0}{4m_i}\left(\frac{R_i}{|\boldsymbol{r}_{i0}|}\right)^3 \left[3\frac{\dot{r}_{i0}}{r_{i0}}\cos(2\gamma_0) + 2\dot{\gamma}_0 \sin(2\gamma_0) \right], \tag{2.91}$$

$$\dot{S}_{2,2}^e = k_2^0 \frac{m_0}{4m_i}\left(\frac{R_i}{|\boldsymbol{r}_{i0}|}\right)^3 \left[3\frac{\dot{r}_{i0}}{r_{i0}}\sin(2\gamma_0) - 2\dot{\gamma}_0 \cos(2\gamma_0) \right], \tag{2.92}$$

with $\dot{\omega}_i$ and $\dot{\gamma}_0$ the derivatives of the rotation rate and body-fixed longitude respectively. Instead of deriving expressions for these parameters or calculating them numerically, Eq. 2.85 is used to circumvent the usage of Eq. 2.90-2.92 in calculating the instantaneous variation of the gravity field coefficients. Furthermore, note that the expression for J_2^e has an additional term that explicitly does not follow from Eq. 2.86. That is because Eq. 2.86 has been derived under the assumption that the only perturbing potential acting on i the tidal potential of body j is, while, in reality, body i also experiences a centrifugal acceleration induced due to its own centrifugal potential, which influences the J_2 coefficient. Again, note that, as mentioned in Section 2.3, it is possible to add the centrifugal potential's contribution to this equation by rewriting it in a form similar to the tidal potential, but about a different axis of symmetry (Murray et al. (1999)).

2.4.3. Coupled equations of motion

Now that a differential equation has been created for the gravity field coefficients, the coupled equations of motion can be set up. First, the general expressions will be provided, which are in principle applicable to any system, as long as the assumptions under which the equations have been derived are met. Specifically, in deriving the translational and rotational equations of motion all bodies are considered rigid. In deriving the equations of motion for the gravity field coefficients, the body's rheology is assumed to follow the Maxwell model, i.e. the body is considered to be a homogeneous viscoelastic body with Maxwell rheology. Note that this is a good rheology for satellites in spin-orbit resonance, but may cause unexpected results for bodies that differ from this.

It is also useful to recall that the translational equation of motion will be expressed in the inertial frame, while the rotational equation of motion and the differential equation for the gravity field coefficients will be expressed in the body-fixed reference frame. For the rotational equation of motion, this choice has been made because it results in a convenient expression for the rotation rate of the body (see section 2.2.2.). For the gravity field coefficients, this choice has been made in order to avoid the need to work with Wigner's D matrix (e.g., Boué et al. 2016). In order to express the differential equation for the gravity field coefficients in the inertial frame, the coefficients themselves have to be represented in the inertial frame, which will require either propagating the gravitational potential in the body-fixed frame (e.g., Boué et al. 2016) or converting the body-fixed gravity field coefficients to inertial gravity field coefficients using Wigner's D matrix. Both complicate the problem without any added benefit, thus they are disregarded as options. This then leads to the following set of differential equations for a body k undergoing forces from a body 0 and j additional bodies:

$$\dot{\boldsymbol{x}}_t = \begin{bmatrix} \dot{\boldsymbol{r}}_k \\ \dot{\boldsymbol{v}}_k \end{bmatrix} = \begin{bmatrix} \boldsymbol{v}_k \\ R^{I/0}\left((\ddot{\boldsymbol{r}}_{0k})_0 + \sum_j^{j\neq k,0} (\ddot{\boldsymbol{r}}_{jk})_0 \right) \end{bmatrix}, \tag{2.93}$$

$$\dot{\boldsymbol{x}}_r = \begin{bmatrix} \dot{\boldsymbol{q}}_k \\ \dot{\boldsymbol{\omega}}_k \end{bmatrix} = \begin{bmatrix} \boldsymbol{Q}_k(\boldsymbol{q}_k)\boldsymbol{\omega}_k \\ \boldsymbol{I}_k^{-1} \cdot (\bar{\boldsymbol{\Gamma}}_k^{(0)} - \dot{I}_k\boldsymbol{\omega}_k - \boldsymbol{\omega}_k \times (I_k\boldsymbol{\omega}_k)) \end{bmatrix}, \tag{2.94}$$

$$Z_{l,m} = \left(1 - \frac{\tau_e}{\tau_l}\right) Z^{\nu}_{l,m} + \frac{\tau_e}{\tau_l} Z^{e}_{l,m}, \quad \text{with} \quad Z^{\nu}_{l,m} + \tau_l \dot{Z}^{\nu}_{l,m} = Z^{e}_{l,m}. \tag{2.95}$$

For the sake of completeness, the above equations will be written out for both the unperturbed and perturbed Earth-Moon case, as well as any additional (to the assumptions in the previous paragraph) assumptions that go into both of these cases. For both cases, the gravity field is limited to degree and order 2. For the unperturbed Earth-Moon case, this work assumes that the extended body - whether it be the satellite or the central body - has a rotation rate $\boldsymbol{\omega}$ orthogonal to the orbital plane and along the axis of maximum inertia, thus implying zero obliquity and essentially making the problem two-dimensional in the orbital plane. For the perturbed Earth-Moon case, these assumptions do not hold and the problem becomes three-dimensional.

For the unperturbed Earth-Moon system, the only non-zero acceleration is the component $(\ddot{\boldsymbol{r}}_{0k})_0$, which is given by Eq. 2.8. The quaternion matrix $\boldsymbol{Q}(\boldsymbol{q})$ is given by Eq. 3.17 while its relation to the unit axes of the body fixed frame is given in Eq. 24 of Fukushima (2008) and also reiterated in Appendix A. The torque $\bar{\boldsymbol{\Gamma}}_{0k}^{(k)}$ is defined by Eq. 2.22, while the inertia tensor $\boldsymbol{I}_k$ is defined by Eq. 2.19. The equations of motion can be written out for the unperturbed Earth-Moon case with satellite i and central body 0 (Note that, while these equations will look at the force exerted by the central body on the satellite, it will work equally well the other way around):

$$\dot{\boldsymbol{x}}_t = \begin{bmatrix} \dot{\boldsymbol{r}}_i \\ \dot{\boldsymbol{v}}_i \end{bmatrix} = \begin{bmatrix} \boldsymbol{v}_i \\ R^{I/0}\Big(-\frac{\mu_i}{r_{i0}^2}\hat{\boldsymbol{r}} - \frac{3\mu_i R_i^2}{2r_{i0}^4} J_2^i \hat{\boldsymbol{r}} - \frac{9\mu_i R_i^2}{r_{i0}^4}(C_{2,2}^i \cos 2\gamma_0 - S_{2,2}^i \sin 2\gamma_0)\hat{\boldsymbol{r}} + \\ \frac{6\mu_i R_i^2}{r_{i0}^4}(C_{2,2}^i \sin 2\gamma_0 + S_{2,2}^i \cos 2\gamma_0)\boldsymbol{K} \times \hat{\boldsymbol{r}}\Big) \end{bmatrix}, \tag{2.96}$$

$$\dot{\boldsymbol{x}}_r = \begin{bmatrix} \dot{\boldsymbol{q}}_i \\ \dot{\boldsymbol{\omega}}_i \end{bmatrix} = \begin{bmatrix} \boldsymbol{Q}_i(\boldsymbol{q}_i)\boldsymbol{\omega}_i \\ \boldsymbol{I}_i^{-1} \cdot (-\frac{6Gm_0m_iR_i^2}{r_{i0}^3}(C_{2,2}^i \sin(2\gamma_0) + S_{2,2}^i \cos(2\gamma_0))\boldsymbol{K} - \dot{I}_i\boldsymbol{\omega}_i - \boldsymbol{\omega}_i \times (I_i\boldsymbol{\omega}_i)) \end{bmatrix}, \tag{2.97}$$

$$Z_{l,m} = \left(1 - \frac{\tau_e}{\tau_l}\right) Z^{\nu}_{l,m} + \frac{\tau_e}{\tau_l} Z^{e}_{l,m}, \quad \text{with} \quad Z^{\nu}_{l,m} + \tau_l \dot{Z}^{\nu}_{l,m} = Z^{e}_{l,m}. \tag{2.98}$$

For the perturbed Earth-Moon system, the acceleration is given by Eq. 2.15, while the gravitational torque is described by Eq. 2.27. The remaining parameters are given by the same equations, resulting in the following equations of motion:

$$\dot{\boldsymbol{x}}_t = \begin{bmatrix} \dot{\boldsymbol{r}}_i \\ \dot{\boldsymbol{v}}_i \end{bmatrix} = \begin{bmatrix} \boldsymbol{v}_i \\ R^{I/0}\Big(\frac{-\mu R_i^2}{r^2}\Big(\Big(\frac{1}{R_i^2} - \frac{3J_2^i}{r^2} P_{2,0}(\sin(\phi_0)) + \frac{3P_{2,2}(\sin(\phi_0))}{r^2}(C_{2,2}^i \cos(2\vartheta_0) + S_{2,2}^i \sin(2\vartheta_0))\Big)\hat{\boldsymbol{r}} \\ + \Big(\frac{3\sin(\phi_0)\cos(\phi_0)J_2^i}{r^2} + \frac{6\sin(\phi_0)\cos(\phi_0)}{r^2}(C_{2,2}^i \cos(2\vartheta_0) + S_{2,2}^i \sin(2\vartheta_0))\Big)\hat{\boldsymbol{\phi}} \\ - \Big(\frac{2P_{2,2}(\sin(\phi_0))}{r^2\cos(\phi_0)}(-C_{2,2}^i \sin(2\vartheta_0) + S_{2,2}^i \cos(2\vartheta_0))\Big)\hat{\boldsymbol{\vartheta}}\Big) - \sum_j \mu_j \Big(\frac{\hat{\boldsymbol{r}}_{ji}}{r_{ji}^2} - \frac{\hat{\boldsymbol{r}}_{j0}}{r_{j0}^2}\Big)\Big) \end{bmatrix}, \tag{2.99}$$

$$\dot{\boldsymbol{x}}_r = \begin{bmatrix} \dot{\boldsymbol{q}}_i \\ \dot{\boldsymbol{\omega}}_i \end{bmatrix} = \begin{bmatrix} \boldsymbol{Q}_i(\boldsymbol{q}_i)\boldsymbol{\omega}_i \\ \boldsymbol{I}_i^{-1} \cdot (-m_0\boldsymbol{r}_{i0} \times (\nabla_i U_i(\boldsymbol{r}_{i0})) - \sum_j^N m_j \boldsymbol{r}_{ij} \times (\nabla_i U_i(\boldsymbol{r}_{ij})) \\ -\dot{I}_i\boldsymbol{\omega}_i - \boldsymbol{\omega}_i \times (I_i\boldsymbol{\omega}_i)) \end{bmatrix}, \tag{2.100}$$

$$Z_{l,m} = \left(1 - \frac{\tau_e}{\tau_l}\right) Z^{\nu}_{l,m} + \frac{\tau_e}{\tau_l} Z^{e}_{l,m}, \quad \text{with} \quad Z^{\nu}_{l,m} + \tau_l \dot{Z}^{\nu}_{l,m} = Z^{e}_{l,m}. \tag{2.101}$$

In summary, the state vector of the problem as introduced in Section 2.1 is given as $y = [\boldsymbol{r}, \boldsymbol{v}, \boldsymbol{\omega}, \boldsymbol{q}, \Delta J_2^{\nu}, \Delta S_{2,2}^{\nu}, \Delta C_{2,2}^{\nu}]$. $\boldsymbol{r}$ and $\boldsymbol{v}$ denote the position and velocity of the perturbing body as seen from the inertial reference frame set in the center of the tidal body (the body experiencing the tides). $\boldsymbol{\omega}$ and $\boldsymbol{q}$ denote the rotation rate and the orientation vector of the tidal body and the gravity field coefficients are given by their relations as described in Eq. 2.95. Note that the $Z_{l,m}^{e}$ coefficients are not part of the state vector, as their expressions are retrieved from Eq. 2.87-2.89.

Eq. 2.93-2.95 completely define the motion of an extended body with time-varying gravity field coefficients. In this work, the three equations will be concurrently integrated, thus allowing for a time-variable gravity field that influences the dynamics of the body and results in certain couplings. For the translational dynamics, it is easy to see that varying gravity field coefficients will influence the acceleration. For the rotational dynamics, the inertia tensor becomes time-variable due to its dependency on the degree 2 gravity field coefficients per Eq. 2.19. Note that if more torques are considered than just the gravitational torque, there may be an additional dependency on the inertia tensor. This work does however not consider such torques, see section 2.2.2. for a justification.

Concurrently integrating Eq. 2.93-2.95, while ensuring full consistency between the translational and rotational dynamics and tidal effects, comes with a price tag in the form of computational expense. For this reason, it is traditionally not common to concurrently integrate these equations in natural satellite dynamics (e.g., Lainey et al. (2007), Dirkx et al. (2016)). Usually, only the translational dynamics are numerically propagated, while analytical approximations are used to model the body's rotation (e.g., Dirkx et al. (2016), Magnanini et al. (2024)). Generally, the tidal effects are approximated using the direct tidal force as given in Eq. 2.62 and 2.66 (e.g., Lainey et al. (2007), Lari (2018), Magnanini et al. (2024), Fayolle (2025)). This choice is generally justified based on the necessary accuracy requirements, similar to how figure-figure interactions of the mutual gravitational potential are left out in some natural satellite dynamics papers (e.g., Dirkx et al. 2016). In this field, concurrently integrating the equations of motion is hence a relatively new concept; strengthening the rationale and novelty of this approach, especially as future missions require preciser dynamical modelling of the accelerations acting on bodies (e.g., Dirkx et al. (2016), Magnanini et al. (2024)).

2.4.4. Initialization of the coupled model

In order to propagate the coupled equations of motion, an initial state vector must be defined. Not every state vector will lend itself to this purpose, for the reason that while mathematically any initial state could be valid (e.g. set the full state vector equal to $\mathbf{0}$), they do not necessarily converge to a physically realistic system. An important example are the librations discussed in section 2.2.3. The full solution of the linearized differential equation as given in Eq. 2.39 for the angle of libration contains both the normal mode and modes raised by external excitations. The normal modes have been assumed to be damped out for the Solar System bodies over a long time scale. However, numerically integrating the rotational equations of motion in the fully coupled model will give rise to these normal modes as no damping has been performed.

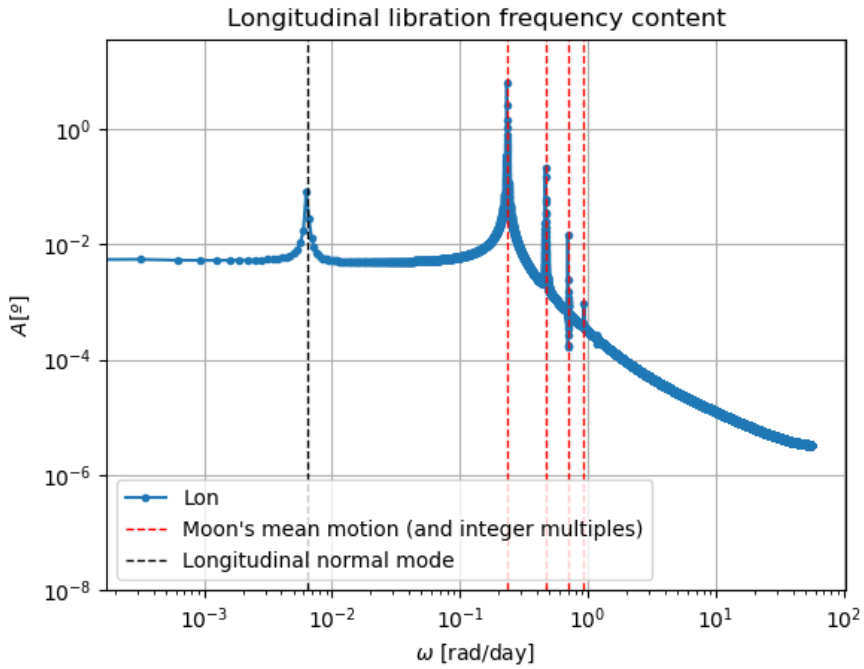

Figure 2.6: Frequency content of the longitudinal libration γ of the Moon using the fully coupled model. The dashed lines represent the frequency of the average mean motion and its integer multiples (red) and the longitudinal normal mode (black).

This is illustrated in Fig. 2.6, where the frequency content of the longitudinal libration γ of the Moon using the fully coupled model has been plotted, along with the frequency content of the mean motion. As expected, the frequency content of γ has its largest peak at the average mean motion, which is one of the reasons why the longitudinal libration is often approximated with a *once-per-orbit* libration at the mean motion (e.g., Fayolle 2025). Next to this peak, multiple smaller peaks are visible at integer multiples of the mean motion, immediately showing that concurrently integrating the rotational equations of motion will likely result in the actual rotational behaviour of the satellite being captured more accurately. Lastly, a peak in the frequency content of γ is also visible at the frequency of the longitudinal normal mode, implying that the Moon's internal excitation mechanism influences its orientation. So unless a physically realistic initial state is used (e.g. a state where the normal modes have been damped out), these normal modes will occur and need to be removed forcefully in order to gain a realistic solution.

There are two steps to determining a physically realistic state for the coupled model. In order to damp the normal modes, an algorithm as introduced by Rambaux et al. (2012) and implemented by Martinez (2023) is used, which introduces a virtual torque into the equations of motion. Conceptually, this additional torque induces a larger tidal dissipation ensuring a faster convergence of the propagation. Mathematically, this virtual torque can be expressed as

$$\boldsymbol{\Gamma}_d = -\frac{1}{\tau_d}\boldsymbol{I}(\boldsymbol{\omega} - \boldsymbol{\omega}_0), \tag{2.102}$$

with τ_d a given dissipation time, $\boldsymbol{\omega}$ the rotation rate of the body expressed in its body-fixed frame and $\boldsymbol{\omega}_0$ its rotation rate in pure synchronous motion (i.e. the desired rotation rate), meaning it will only have a non-zero component along the $\boldsymbol{K}$-axis. In order to damp out the normal modes, the equations of motion in Eq. 2.93-2.95 are propagated with this additional virtual torque. The resulting final state is then propagated backwards in time without the virtual torque, resulting in an initial state that should have damped normal modes. Naturally, this is an iterative process, and as Martinez (2023) points out, it will likely take several iterations to obtain an initial state with a sufficiently damped out normal mode. While this method worked well for Martinez (2023), it is important to realize they considered a fully coupled translational-rotational set of equations of motion, i.e. the bodies analyzed were assumed rigid. Since in this work tidal dissipation is also considered, it is important that the gravity field coefficients

also converge to their true values. This makes it unclear whether this method will be applicable to the problem at hand out of the box, or whether it requires some modification in order to incorporate the fact that tidal dissipation occurs within the system.

To this end, a second step is added to aid in finding a physically realistic initial state, which in itself consists of two steps for redundancy. Analogously to how a virtual torque is introduced to damp the rotation, a similar equation can be used to damp the normal modes in the gravity field coefficients:

$$\dot{Z}^{\nu}_{l,m} = -\frac{1}{\tau_l}(Z_{l,m} - Z^{e}_{l,m}), \tag{2.103}$$

with $Z_{l,m}$ the current value of the gravity field coefficient. The goal of this equation is to aid the process of the gravity field coefficients converging to stable values where the normal modes have been damped out. Since this is a novel method, however, there is no guarantee of it working. To ensure that a proper initial state is still achieved, the second method employed is quite straightforward. Since Eq. 2.102 is proven to work, it should find an initial state that has damped the normal modes significantly, but perhaps not completely. In reality, such a virtual torque does not exist, and damping has taken place due to tidal dissipation. Taking inspiration of how the damping of normal modes have occured in the Solar System, a second method is to simply run the propagation for a long time (far past the relaxation time of the body) and let the remaining normal modes be damped using tidal dissipation. The downside of this method is that it is, beforehand, not clear for how long this propagation should be ran. Instead, a trial-and-error method is employed.

There may be other possible solutions that will lead to the same result of a physically realistic initial state. These are just two possibilities and further in the thesis other methods may be devised. It is however important to be aware of the existence of this problem as it will likely be difficult to properly initialize this model given its natural inclusion of the normal modes and tidal dissipation.

2.5. Verification & Validation

Once implemented, the coupled equations of motion in Eq. 2.93-2.95 can be compared to state-of-the-art approximations for relevant parameters. The goal is to measure the accuracy of the coupled model, but also to investigate possible deviations between the coupled model and the state-of-the-art model, which could possibly indicate that some (coupled) effects are captured better by the coupled model. This includes the orbital evolution for the semi-major axis a as well as the eccentricity e of the satellite. Next to that, comparison of the gravity field coefficients are made in order to see whether the model has properly converged. The inertia tensor's evolution will be compared against the evolution of the gravity field coefficients and the tidal lag and lag angle will also be compared against literature approximations. Lastly, the effects of librations will be discussed. Comparing this work's method against existing approximations is important to ensure that the method is working correctly and to identify where current approximations do not properly capture coupled effects, making it a key component of the research and an important section in the literature study.

2.5.1. Linear approximations for the semi-major axis and eccentricity evolution

The raised tidal torques by the planet and satellite tides as described in section 2.3.2 (Eq. 2.67) induce secular variations in the satellite's semi-major axis a_i and eccentricity e_i (Goldreich et al. (1966)). This can imply either an increase or decrease of a_i depending on whether the satellite's mean motion is greater than the central body's rotation rate or not. For the tides raised by the satellite i on the planet 0, the evolution of the semi-major axis is commonly described as (e.g. Souchay et al. (2013), Boué (2019)):

$$\frac{da^0_i}{dt} = \text{sign}(\omega_0 - n_i)3\frac{k^0_2 m_i}{Q^i_0 m_0}\left(\frac{R_0}{a_i}\right)^5 n_i a_i, \tag{2.104}$$

where all parameters are as defined in previous section. Note that the sign function specifies whether the derivative of a_i is positive or negative, allowing the possibility of the satellite's orbit expanding or shrieking, depending on whether or not it lies beyond the stationary orbit. The derivation of Eq. 2.104 can be found in Souchay et al. (2013)'s section 5.3.2, where it follows from the conservation of angular momentum in the two-body system in combination with several assumptions: the orbit is assumed to be equatorial, prograde and circular, the time lag to be constant and independent of the

tidal frequency (i.e. the constant time lag model is used), the moment of inertia of the central body to be constant, the spin vector of the central body to be aligned with its polar axis and the mass of the central body to be much larger than the mass of the satellite. This further highlights the flexibility of the coupled model, which does not rely on any of these assumptions.

If $e_i \neq 0$, the tides raised by the satellite on the central body also incur a change in the eccentricity of the satellite. This follows from expanding the tidal potential as a Fourier series (the same result can be obtained from the conservation of angular momentum, see Fayolle (2025)), working out the orbital element variations then yields the rate of change of e_i as (e.g. Jeffreys (1976), Souchay et al. (2013)):

$$\frac{de_i^0}{dt} = \text{sign}\left(3\omega_0 - 2n_i\right) \frac{57}{8} \frac{k_2^0 m_i}{Q_0^i m_0} \left(\frac{R_0}{a_i}\right)^5 n_i e_i, \tag{2.105}$$

where the same assumptions hold except for a circular orbit. Notice that the expression that governs the sign function is now more complex due to dependence of e_i on different tidal parameters than a_i (Goldreich et al. (1966)).

Although the underlying physics for the planet and satellite tides as discussed in section 2.3. is the same, the phenomenology is, as discussed in the same section, quite different. For the tides raised by a satellite in spin-orbit resonance on itself, different expressions than Eq. 2.104 and Eq. 2.105 hold for the evolution of a_i and e_i, where they are respectively given as (e.g., Boué 2019):

$$\frac{da_i^i}{dt} = -21 \frac{k_2^i m_0}{Q_i^0 m_i} \left(\frac{R_i}{a_i}\right)^5 n_i a_i e_i^2, \tag{2.106}$$

$$\frac{de_i^i}{dt} = -\frac{21}{2} \frac{k_2^i m_0}{Q_i^0 m_i} \left(\frac{R_i}{a_i}\right)^5 n_i e_i. \tag{2.107}$$

It is useful to note that another expression for the rate of change of a_i exists in literature (e.g., Souchay et al. 2013):

$$\frac{da_i^i}{dt} = -57 \frac{k_2^i m_0}{Q_i^0 m_i} \left(\frac{R_i}{a_i}\right)^5 n_i a_i e_i^2, \tag{2.108}$$

where Eq. 2.108 and Eq. 2.106 differ a factor $57/21$. As explained by Fayolle (2025), Eq. 2.108 is consistent with a perfectly synchronous satellite, while Eq. 2.106 is consistent with a satellite in pseudo-synchronous rotation. Here, an issue arises from many studies assuming that the average tidal torque over one orbit is zero, while using Eq. 2.106 for the secular evolution of a_i. As discussed in Fayolle (2025)'s section 2.3.3, considering an averaged torque of 0 over one orbit implies a pseudo-synchronous satellite for non-circular orbits. This appears to contradict Solar System observations, from which it is known that many satellites are in synchronous rotation (e.g., Efroimsky et al. 2013). This observed synchronous rotation actually would result in a non-zero tidal torque over one orbit Fayolle (2025). However, the non-zero tidal torque can be, as mentioned before, compensated for by a small shift in the pointing direction of the long axis of the satellite (e.g., Yoder (1981), Souchay et al. (2013), Fayolle (2025)). This corresponds to a non-zero $S_{2,2}^i(t)$ coefficient, which would affect the orbit of the satellite similar to tidal dissipation (Fayolle (2025)).

In other words, following Fayolle (2025), Eq. 2.108 accurately models the effect of the satellite tides on the evolution of the semi-major axis. However, the effective semi-major axis evolution follows from the combined effect of tidal dissipation and a non-zero $S_{2,2}^i(t)$ coefficient, which cancels the non-zero tidal torque and leads to Eq. 2.106. This once more highlights the sensitivity of the used models to the rotation rate of the satellite. To conclude, Eq. 2.106 and Eq. 2.107 accurately model the evolution of the satellite's semi-major axis and eccentricity due to its own tides and will be used in this work to compare the results from the coupled model.

2.5.2. Gravity field coefficients

Next to the evolution of the orbital parameters, it will also be interesting to see how the gravity field coefficients, calculated using Eq. 2.95, evolve due to the sudden stresses of the introduced bodies, which will give insight into how, given certain relaxation times, a body deforms under stresses. Furthermore, it will be interesting to see how $S_{2,2}^i(t)$ evolves, especially given the discussion in the previous

subsection. In order to compare the results from this equation, they can be compared to state-of-the-art approximations for the coefficients, which uses a complex Love number to account for tidal lag, assuming a constant phase lag (e.g., Petit et al. 2010):

$$J_2^i = \left(\frac{\omega_i^2 R_i^3}{3\mu_i} + \frac{1}{2}\frac{m_i}{m_0}\left(\frac{R_i}{|\boldsymbol{r}_{i0}|}\right)^3 \right) \mathrm{Re}(k_2^i), \tag{2.109}$$

$$C_{2,2}^i = \frac{1}{4}\frac{m_i}{m_0}\left(\frac{R_i}{|\boldsymbol{r}_{i0}|}\right)^3 \left(\mathrm{Re}(k_2^i)\cos 2\gamma_0 - \mathrm{Im}(k_2^i)\sin 2\gamma_0\right), \tag{2.110}$$

$$S_{2,2}^i = -\frac{1}{4}\frac{m_i}{m_0}\left(\frac{R_i}{|\boldsymbol{r}_{i0}|}\right)^3 \left(\mathrm{Re}(k_2^i)\sin 2\gamma_0 + \mathrm{Im}(k_2^i)\cos 2\gamma_0\right), \tag{2.111}$$

where again the centrifugal potential's effect on J_2^i is accounted for. Here $\mathrm{Re}(k_2^i)$ and $\mathrm{Im}(k_2^i)$ denote the real and imaginary part of k_2^i, accounting for the 'amplitude' and phase lag of the tidal bulge respectively. The following relations can be derived for them assuming a small phase lag δ, also reiterating Eq. 2.51, as it is useful to realize that Eq. 2.109-2.111 can be completely determined using parameters from literature and the uncoupled model:

$$k_2^i = |k_2^i|\exp(-i\cdot 2\delta_i) = \mathrm{Re}(k_2^i) + i\mathrm{Im}(k_2^i), \tag{2.112}$$

$$\mathrm{Re}(k_2^i) = |k_2^i|\cos 2\delta_i \approx |k_2^i|, \tag{2.113}$$

$$\mathrm{Im}(k_2^i) = -|k_2^i|\sin 2\delta_i = -\frac{|k_2^i|}{Q_i^0}. \tag{2.114}$$

Here, the real part of the Love number is assumed equal to the literature value of the Love number.

Since the tidal coefficients completely dictate the gravitational shape of the body through the induced gravitational potential, they can be used to calculate geometric lag angle δ_i by the following relations:

$$\nu_i = \frac{1}{2}\arctan 2\left(\frac{S_{2,2}^i}{C_{2,2}^i}\right), \tag{2.115}$$

$$\gamma_i = (\mathrm{sign}(\hat{e}_A \cdot (\hat{r_{i0}} \times \hat{e}_C)))\cdot \arccos(\hat{e}_A \cdot \hat{r}) \mod 2\pi, \tag{2.116}$$

$$\delta_i = (\nu_i - \gamma_i) \mod \pi. \tag{2.117}$$

The first angle, ν_i, is the angle between the tidal bulge and the body-fixed I-axis, which is only non-zero when $S_{2,2}^i \neq 0$. Two implications follow from this: if $C_{2,2}^i \neq 0$ and $S_{2,2}^i = 0$, the satellite's tidal bulge (and thus long axis) is aligned with the body fixed I-axis, and thus the average evolution of a_i, $\frac{\mathrm{d}\bar{a}_i}{\mathrm{d}t} = 0$. If $C_{2,2}^i \neq 0$ and $S_{2,2}^i \neq 0$, $\frac{\mathrm{d}\bar{a}_i}{\mathrm{d}t} \neq 0$.

The geometic lag angle retrieved from Eq. 2.117 can be compared to the constant lag angle retrieved from Eq. 2.51. Note that since it has been assumed constant, it will fail to capture intricate details that the coupled model might be able to catch, next to being a worse approximation than the constant time lag model (e.g., Efroimsky et al. 2013). Similarly, the time lag Δt is assumed constant in current models, but the coupled model can also capture variations in Δt by realizing it follows from the distance divided by velocity; in this case the distance between the bulge's position and the perturber's position divided by the relative rotational velocity as seen from the body-fixed frame:

$$\Delta t_i = \frac{\delta_i |\boldsymbol{r}_{i0}|}{|\boldsymbol{\omega}_i \times \boldsymbol{r}_{i0} - \boldsymbol{v}_i|}. \tag{2.118}$$

Lastly, the values of the derivative of the inertia tensor may be compared against the values retrieved for the gravity field coefficients as follows from Eq. 2.94 and 2.95 respectively. This should rather serve as a sanity check; if the model is propagated correctly these values should agree with each other as the inertia tensor is completely defined by the J_2, $S_{2,2}$ and $C_{2,2}$ provided we limit the gravitational potential to $l = 2$. Similarly, its derivative $\dot{\boldsymbol{I}}$ is completely defined by $\dot{J}_2$, $\dot{S}_{2,2}$ and $\dot{C}_{2,2}$, see Eq. 2.19.

2.5.3. Librations

Librations have been discussed extensively in Section 3.3, where it has been noted that librations are not a real physical concept, but rather quantify the variations in the rotation angle of the satellite, where the angles are defined as in Eq. 3.19. Important is to note that wrong initial conditions will add to the variations of the rotation angle, which can then yield unphysical librations. Free librations, as discussed before, should be damped out in the numerical simulations. Their main frequency is given by (Maistre et al. (2013)):

$$\nu_f = n_i \frac{B-A}{C}, \tag{2.119}$$

with $A \leq B \leq C$ the principal moments of inertia in the body-fixed axes directions. For the forced librations, generally the largest contribution is made by a once-per-orbit longitudinal libration, where the amplitude can be given by two different approximations, following Willner et al. (2010) and Efroimsky (2018), they respectively state that:

$$\theta_\tau = \frac{2e_i}{1 - \frac{C}{3(B-A)}}, \tag{2.120}$$

$$\theta_\tau = -6e_i \frac{B-A}{C} + \mathcal{O}(e_i^3), \tag{2.121}$$

where Efroimsky (2018) uses a different approximation to get to the result. While Eq. 6.17 is more commonly used in literature, it will be useful to compare against both approximations.

As said before, librations are simply a convenience term describing the variations in the rotation angle. This rotation angle can then, looking at Fig. 2.1, be given as

$$\theta = \text{arctan2}\left(\boldsymbol{I}_y / \boldsymbol{I}_x\right). \tag{2.122}$$

The variation in the rotation angle can then be found by fitting a linear function to the rotation angle; the differences between θ and this linear fit are the (physical) librations.

Efroimsky (2018) states that librations can also cause dissipations similar to tidal dissipations, because they affect tidal torques through the dependency of the rotation rate on librations (see Fayolle (2025) for a more extensive discussion). Efroimsky (2018) gives a relation between this additional dissipation due to librations with respect to the tidally induced powers as if there were no librations. The coupled model should automatically incorporate this, so it will be interesting to see whether this effect can be correctly predicted by the relation proposed by Efroimsky (2018), assuming a once-per-orbit longitudinal libration:

$$\frac{\langle P \rangle_{\text{tide}}^{(\text{lib})}}{\langle P \rangle_{\text{tide}}^{(\text{main})}} = 1 - \frac{4\theta_\tau}{7e_i} + \frac{\theta_\tau^2 + \theta_f^2}{7e_i^2}, \tag{2.123}$$

where θ_f is the amplitude of the free librations, which should be approximately equal to 0 for most Solar System bodies, slightly simplifying the relation and the (lib) and (tide) superscripts indicate the tidal power including librations and the tidal power as if there were no librations. This relation is derived under several assumptions that should be met; it assumes a zero obliquity, $\theta_f < 12^\circ$ and a near-spherical satellite body described by a Maxwell rheology.

Since a_i and e_i are governed by the orbital E_{orb} and rotational energy E_{rot}, their evolution is governed by the generated tidal energy dissipation (assuming that energy dissipation is completely due to tidal dissipation):

$$\dot{E} = -(\dot{E}_{rot} + \dot{E}_{orb}), \tag{2.124}$$

Their relations to $\dot{a}$ and $\dot{e}$ are given as (e.g., Correia et al. 2014):

$$\dot{a}_i = \frac{2\dot{E}_{\text{orb}}}{\beta a_i n_i^2}, \tag{2.125}$$

and

$$\dot{e}_i = \frac{(1-e_i^2)}{\beta n_i a_i^2 e_i} \left(\frac{\dot{E}_{\text{orb}}}{n_A} + \frac{\dot{E}_{\text{rot}}}{\omega_i \sqrt{1-e^2}} \right), \tag{2.126}$$

where β is the reduced mass of the system. Since the orbital energy is generally much larger than the rotational energy, Eq. 2.126 can, but need not, be simplified. Eq. 2.125 and Eq. 2.126 should in theory result in the same values are will be derived from the coupled model and Eq. 2.105 and 2.106. It will serve as a good verification method to compute the total energy that is dissipated by the coupled model and verify the values for the evolution of a_i and e_i, giving extra confidence to the generated results.

Lastly, since the librations result in extra energy dissipation as in Eq. 2.122, the equations 2.105 and 2.106 must account for this additional dissipation, as these equations, and most literature, assume that librations do not induce additional dissipations (e.g., Efroimsky 2018). The approximations for the evolution of a_i and e_i due the satellite tides is then given as

$$\frac{da_i^i}{dt} = \frac{\langle P \rangle_{\text{(lib)}}}{\langle P \rangle_{\text{(main)}}} \frac{da_i^i}{dt}\bigg|_{\text{Literature}}, \tag{2.127}$$

$$\frac{de_i^i}{dt} = \frac{\langle P \rangle_{\text{(lib)}}}{\langle P \rangle_{\text{(main)}}} \frac{de_i^i}{dt}\bigg|_{\text{Literature}}. \tag{2.128}$$

2.6. Thesis Planning

In the previous sections, the theoretical framework has been laid out to understand current state-of-the-art models and literature approximations, and the newer coupled model. Section 4 introduced the direct tidal force that is used in literature, which can miss important interactions that influence the dynamics of bodies. The thesis will aim to couple these effects and incorporate them. The rest of the chapter will outline how this thesis plans to tackle that.

2.6.1. Problem statement

The aim of this thesis will be to implement the coupled model, which combines the translational, rotational and tidal dynamics and propagates them concurrently, and apply it to Earth-Moon system and possibly other systems, such as Jupiter and the Galilean moons. The Earth-Moon system is chosen because it is the most well-known system, compared to more complex systems such as Mars-Phobos or Jupiter and the Galilean moons, allowing to build on existing knowledge (such as in Mol (2021)) to dive deeper into the system. It will also serve as a good benchmark to ensure that the coupled model can accurately produce values for the orbital migration rate of the satellite. Jupiter and the Galilean moons are an interesting system, because this model has to date not yet been applied on it. The application to this system may be of interest for data analysis from future missions headed to this system, such as JUICE and the Europa Clipper. As such, it will be useful to compare the uncoupled and coupled model. The following research question with sub-questions can be defined:

- What is the effect of using a fully coupled model compared to current-day models in natural satellites' dynamics modelling in planetary systems?
  - Can proper initialization reliably be achieved for the system(s) in question?
    - How can physically realistic initialization reliably be achieved for the uncoupled model, where the initial state is given by $y_U = [\boldsymbol{r}, \boldsymbol{v}, \boldsymbol{\omega}, \boldsymbol{q}]$ at $t = 0$?
    - How can physically realistic initialization reliably be achieved for the uncoupled model, where the initial state is given by $y_C = [\boldsymbol{r}, \boldsymbol{v}, \boldsymbol{\omega}, \boldsymbol{q}, \Delta J_2^\nu, \Delta S_{2,2}^\nu, \Delta C_{2,2}^\nu]$ at $t = 0$?
  - What is the effect of the coupled model for an unperturbed and perturbed system with tides raised on the primary?
    - What is the behaviour of the coupled model on the evolution of gravity field coefficients, tidal lag angle and time lag?
    - What is the behaviour of the coupled model on the evolution of the orbital elements a and e?
  - What is the effect of the coupled model for an unperturbed and perturbed system with tides raised on the secondary?
    - What is the behaviour of the coupled model on the evolution of gravity field coefficients?
    - What is the behaviour of the coupled model on the evolution of the orbital elements a and e and librations?

  - How can the coupled model be used to improve current and future data analysis from planetary missions for the measured parameters?
    * How can the coupled model improve current and future data analysis for a system with tides on the primary?
    * How can the coupled model improve current and future data analysis for a system with tides on the secondary?
    * Can the coupled model capture the correct behaviour for a system when analyzing both tides on the primary and secondary simultaneously?

The first sub-question aims to tackle what might be the biggest challenge of the coupled model: a (semi-)random initial state will likely lead to non-realistic systems due to existing normal modes in the rotational dynamics. It is therefore crucial to be able to dampen these normal modes to find an initial state that is physically realistic. Furthermore, the coupled model includes the time-variable gravity field coefficients. It is crucial to have the right static and time-variable parts of these coefficients to ensure no unintended behaviour, which adds another layer of complexity to the initialization problem. To this end, the first sub-question will tackle whether it is possible to come up with a method to reliably find an initial state for planetary systems. This will allow for the coupled model to generate the necessary results and answer the second and third sub-questions.

The second sub-question looks into the effect of the coupled model for the tides on the primary. As will be explained in Section 7.2.1, the tides can be analyzed separately on the primary and secondary body, which is relevant as it is much easier to determine them on the primary than secondary body due to the additional radial tides secondary bodies experience. The question looks into the behaviour of the coupled model on several relevant parameters; the gravity field coefficients, the tidal lag angle, the time lag and the orbital elements a and e. Determining the tides on the primary is expected to be relatively straightforward compared to determining the tides on the secondary.

The third sub-question looks into the effect of the coupled model for the tides on the secondary by looking into the behaviour of the coupled model for the relevant parameters; the gravity field coefficients, the orbital elements a and e and the librations of the body. It is usually (much) harder to determine the tides on the secondary due to the general presence of radial tides, shown by the current-day discussions about correct approximations for the evolution of a, see Eq. 6.3 and Eq. 6.4. As discussed in Section 4.2, there exist some approximations but the combination of longitudinal and radial librations, as well as their induced dissipation, are hard to determine.

The fourth sub-question acts as a follow up question dependent on all three previous sub-questions. Once the coupled model has successfully been applied to the system(s) in question, the gathered results can be analyzed and compared to the uncoupled model and literature estimations of the relevant parameters. The aim is to determine whether the coupled model can be used for improving data analysis of current and future planetary missions for tides on the primary, secondary and perhaps both simultaneously.

Once, and if, the coupled model is validated for the Earth-Moon system, it can be applied to Jupiter and its moons to find approximations for the given parameters of interest. For this system, there is both less data available, and the system itself is also more complex due to containing multiple bodies as well as having the effect of Laplace resonance, adding an extra layer of complexity. It will be interesting to see whether the coupled model can be applied to such a system and whether it can produce reasonable results when compared to the uncoupled model and existing literature approximations.

2.6.2. Thesis planning

In order to answer the research question and the associated sub questions, this section will outline the planning of the thesis.

Tasks

In order to answer the sub-questions, two models will be created for each of the systems: a conventional direct tidal force model, where the translational and rotational dynamics are coupled, but the tidal force is added to both of these as given in Section 4.2, and a fully coupled model. This results in the following set of models that must be set up:

- **Model** U_i: Uncoupled model for system i. This adds the direct tidal force and torque to the translational and rotational dynamics of the system respectively.

- **Model** C_i: The fully coupled model, which propagates the translational, rotational and tidal dynamics together.

Here, the Earth-Moon system is indicated with E and the Jupiter system is indicated with J, resulting in four models: U_E, C_E, U_J, C_J. It will be useful to get a good idea of the parameters that will be estimated for each model. For the uncoupled model, the state vector will consist of $y_U = [\boldsymbol{r}, \boldsymbol{v}, \boldsymbol{\omega}, \boldsymbol{q}]$, while the coupled model's state vector is given by $y_C = [\boldsymbol{r}, \boldsymbol{v}, \boldsymbol{\omega}, \boldsymbol{q}, \Delta J_2^\nu, \Delta S_{2,2}^\nu, \Delta C_{2,2}^\nu]$. In the case of a two-body system, such as the Earth-Moon system, there is the option of analyzing the tides on the primary and secondary body seperately or together. It is useful to first analyze the tides on the bodies seperately and then together, to see whether literature approximations of evolutions of the relevant parameters can simply be added together to acquire the total evolution of the system, or whether more complex coupled relations will appear. To this end, three additional models can be created:

- **Model** X_i^P: Model with the primary body being an extended body and the secondary body being a point mass, thus modelling the tides on the primary body.
- **Model** X_i^S: Model with the secondary body being an extended body and the primary body being a point mass, thus modelling the tides on the secondary body.
- **Model** X_i: Model with both bodies as extended bodies, thus modelling the tides on both bodies at the same time.

This results in six models for each system. Note that for the uncoupled models, the above models refer to adding the direct tidal force correction to the right body in question. The point-mass body will, in both the uncoupled and coupled model, simply experience translational and rotational dynamics and be modelled as a rigid body.

These models are used in answering the first sub-question during the set-up and verification & validation of the models; they will only be functional once initialization is successful. Hence, the successful development of the coupled models will be a direct indication of a successful method applied for initialization of the models. As an initial attempt, the method laid out in Rambaux et al. (2012) and implemented in Martinez (2023) will be used in order to provide a realistic initial state for both the uncoupled and coupled model, as both will propagate the translational and rotational dynamics in a coupled manner. The process is described in Section 5.4. As mentioned there, additional care must be taken in initialization of the coupled model, since it naturally will have some form of dissipation due to the tides raised on the bodies. Seperating this from the additional 'virtual' dissipation has never been done before and thus may prove to be challenging. For the uncoupled model it will be easier since the rigid bodies considered there will have no dissipation.

By propagating the initial state forward with this introduced virtual torque, and then backwards without this virtual torque, and initial state may be obtained where the normal modes of the librations are damped. Indirectly, this may also influence how the static and time-variable part of the gravity field coefficients are 'distributed'. In the case that this only proves to dampen the normal modes, but does not aid in initialization of the gravity field coefficients, an additional form of virtual dissipation must be added, such as tidal dissipation. This may take several iterations until the retrieved initial state satisfies a certain convergence criterium. This initial state is then used as the initial condition. In this work, solutions between initial states where normal modes appear and initial states where they are damped are not compared, since this is not within the scope of the thesis. Instead, focus will be put on finding these initial states where normal modes have been damped out, starting with the Earth-Moon system.

The second and third sub-questions can be answered by retrieving the necessary data from the respective models for the primary and secondary bodies. Once the models have been successfully set up and validated and a successful propagation has been performed, the evolution of the parameters mentioned in the sub-questions can be retrieved from y_C with the proper equations; for the tides on the primary, the tidal lag angle and the time lag can be caclulated using Eq. 6.14 and 6.15; for the tides on the secondary, the librational amplitude can be calculated using Eq. 6.19; for both the primary and the secondary, the gravity field coefficients follow from the state vector in combination with Eq. 5.22 and the evolution of the orbital elements a and e can be calculated by converting the cartesian state in the state vector to keplerian elements.

Finally, the fourth sub-question can be answered by comparing the results generated by the coupled models with the uncoupled models and literature approximations. It will be interesting to see whether

it can reproduce, or improve, state of the art results in the parameters of interest for the primary, secondary or both simultaneously. The evolution of the parameters mentions in the sub-questions can be retrieved from y_U and literature approximations with the following equations; for the tides on the primary, the tidal lag angle and the time lag can be approximated using Eq. 4.9, the orbital elements a and e can be approximated using Eq. 6.1 and 6.2; for the tides on the secondary, the librational amplitude can be approximated using Eq. 6.17 and 6.18, the orbital elements a and e can be approximated using Eq. 6.3-6.5 and Eq. 6.25-6.26; for both the primary and the secondary, the gravity field coefficients can be approximating with Eq. 6.6-6.8.

Ultimately, it must be kept in mind that the scope of analysis may vary between different systems. Since the coupled model has already been applied to the Earth-Moon system (Mol, 2021), it allows for deeper and complexer analysis of this system. On the other hand, this has not been done for the Jupiter system, warranting a more preliminary and global approach, especially considering the added complexity the Jupiter system poses with its Galilean moons and Laplace resonance between these moons. It is therefore not unthinkable that any of the following situations may occur: A deep dive in the Earth-Moon system proves to warrant enough research on its own; a deep dive in the Earth-Moon system and a preliminary analysis of the Jupiter system warrant enough research; and finally, time allows for a deep-dive application of the coupled model to both systems, which would likely be the best case scenario.

The plan

The tasks laid out can be summarized in the following work packages:

- **Workpackage 1: Build and initialize the uncoupled models; retrieve values from propagations and do reporting. Expected duration: 2 month**
  - WP 1.1 - Build U_i^P, U_i^S, U_i. Expected duration: 4 weeks
    - WP 1.1.1 - Build coupled translational & rotational dynamics (Eq. 5.20, 5.21)
    - WP 1.1.2 - Add direct tidal force correction to equations of motion (Eq. 4.15, 4.18)
    - WP 1.1.3 - Reporting
  - WP 1.2 - Initialization. Expected duration: 3 weeks
  - WP 1.3 - Reporting. Expected duration: 1 week
- **Workpackage 2: Build and initialize the coupled models; retrieve values from propagations and do reporting. Expected duration: 3 months**
  - WP 2.1 - Build C_i^P, C_i^S, C_i. Expected duration: 1 month
    - WP 2.1.1 - Incorporate coupled tidal dynamics (Eq. 5.22)
    - WP 2.1.2 - Reporting
  - WP 2.2 - Initialization. Expected duration: 2 months
  - WP 2.3 - Reporting. Expected duration: 1 week
- **Workpackage 3: Verification & Validation of the coupled model. Expected duration: 2 months**
  - WP 3.1 - Propagate uncoupled models. Expected duration: 2 weeks
    - WP 3.1.1 - Retrieve data for tides on the primary
      - WP 3.1.1.1 - Retrieve orbital elements $a(t)$ and $e(t)$ and their derivatives for a range of settings varying the body parameters (k_2, Q)
      - WP 3.1.1.2 - Reporting
    - WP 3.1.2 - Retrieve data for tides on the secondary
      - WP 3.1.2.1 - Retrieve orbital elements $a(t)$ and $e(t)$ and their derivatives for a range of settings varying the body parameters (k_2, Q)
      - WP 3.1.2.2 - Reporting
    - WP 3.1.3 - Retrieve data for tides raised on both bodies
      - WP 3.1.3.1 - Retrieve orbital elements $a(t)$ and $e(t)$ and their derivatives for a range of settings varying the body parameters (k_2, Q)
      - WP 3.1.3.2 - Reporting
  - WP 3.2 - Propagate coupled models. Expected duration: 5 weeks

        - WP 3.2.1 - Retrieve data for tides on the primary
            - WP 3.2.1.1 - Retrieve tidal lag angle, time lag (Eq. 6.14, 6.15)
            - WP 3.2.1.2 - Retrieve orbital elements $a(t)$ and $e(t)$ and their derivatives for a range of settings varying the body parameters (τ_e, τ)
            - WP 3.2.1.3 - Retrieve gravity field coefficients (Eq. 5.22)
            - WP 3.2.1.4 - Validate WP 3.2.1.1-3.2.1.3 against literature approximations in WP 3.3.1
            - WP 3.2.1.5 - Validate WP 3.2.1.2 against uncoupled model results in WP 3.1.1
            - WP 3.2.1.6 - Reporting
        - WP 3.2.2 - Retrieve data for tides on the secondary
            - WP 3.2.2.1 - Retrieve librational amplitudes (Eq. 6.19)
            - WP 3.2.2.2 - Retrieve orbital elements $a(t)$ and $e(t)$ and their derivatives for a range of settings varying the body parameters (τ_e, τ)
            - WP 3.2.2.3 - Retrieve gravity field coefficients (Eq. 5.22)
            - WP 3.2.2.4 - Validate WP 3.2.2.1-3.2.2.3 against literature approximations in WP 3.3.2
            - WP 3.2.2.5 - Validate WP 3.2.2.2 against uncoupled model results in WP 3.1.2
            - WP 3.2.2.4 - Reporting
        - WP 3.2.3 - Retrieve data for tides raised on both bodies
            - WP 3.2.3.1 - Retrieve and validate data as in WP 3.2.1 and 3.2.2
            - WP 3.2.3.2 - Reporting
    - WP 3.3 - Literature approximations. Expected duration: 1 week
        - WP 3.3.1 - Literature approximations for tides on the primary
            - WP 3.3.1.1 - Calculate the tidal lag angle, time lag (Eq. 4.9)
            - WP 3.3.1.2 - Calculate the orbital evolution of $a(t)$ and $e(t)$ for a range of settings varying the body parameters (k_2, Q) (Eq. 6.1, 6.2)
            - WP 3.3.1.3 - Calculate the gravity field coefficients (Eq. 6.6-6.8)
            - WP 3.3.1.4 - Reporting
        - WP 3.3.2 - Literature approximations for tides on the secondary
            - WP 3.3.2.1 - Calculate the librational amplitude (Eq. 6.17, 6.18)
            - WP 3.3.2.2 - Calculate the orbital evolution of $a(t)$ and $e(t)$ for a range of settings varying the body parameters (k_2, Q) (Eq. 6.3-6.5, 6.25, 6.26)
            - WP 3.3.2.3 - Calculate the gravity field coefficients (Eq. 6.6-6.8)
            - WP. 3.3.3.4 - Reporting
    - WP 3.4 - Reporting
- **Workpackage 4: Analyse results of the uncoupled model. Expected duration: 2 weeks**
    - WP 4.1 - Analyse and compare results from WP 3.1
    - WP 4.2 - Reporting
- **Workpackage 5: Analyse results of the model model. Expected duration: 6 weeks**
    - WP 5.1 - Analyse & compare results from WP 3.2 and WP 3.3
    - WP 5.2 - Reporting

The work packages can be split in two main parts: work packages 1 to 3, which consist of building the necessary models and generating the required numbers for later analysis. This includes initialization of the models, validating the models as well as retrieving results from the models, which implicitly answers the first sub-question. The second part, work packages 4 and 5, consist of analyzing the retrieved data and answering the three latter sub-questions, where work package 4 serves as analysis of data that will act as validation for the coupled model, which really answers the three sub-questions.

The first half is expected to take the majority of the time, as it consists of building all the models as well as the initialization of these models. It is expected that initiating code will probably take quite long, but may be sped up due to code available from Martinez (2023) and Mol (2021). Including writing the relevant part of the thesis, it will probably take around 6-7 months.

The second half is, once the data is generated, focused mainly on post-processing and generating plots. It will also entail writing results, analyses and conclusions in the thesis, which can also prove to be time consuming. An estimated 2-3 months is reserved for this.

Note that there is no mention made of the specific system for which these work packages hold. The core code and applied algorithms for initialization are not expected to differ greatly between the Earth-Moon system and the Jupiter system, but may require some small tweaks or modifications. It is by this reasoning that the expectation is that once the models have been built, they may readily be applied to the Jupiter system and thus also generate results for this system. Then the analyses can be done concurrently. Naturally, initialization may also prove to be far more complex due to the aforementioned Laplace resonance. This is an unknown factor that is hard to determine, and hence no time-estimate will be placed upon this, other than including a possible deviation in the time spent for the two parts.

The software development for this thesis will be done in Python, where code will be developed based on previous code created by Martinez (2023) and Mol (2021). Both of their codes contain snippets that may be useful for creation of the models at hand, and thus it makes sense to use these.

For the set up of the coupled translational and rotational dynamics simulator, it may be validated against the TU Delft Astrodynamics Toolbox[1] (Tudat), which is a C++ software package with a Python wrapper readily available maintained by staff and students from TU Delft. It contains implementations of integrators, propagators, translational and rotational dynamics simulators and more. It is a proven tool and hence will be useful in validating the self-made coupled translational-rotational dynamics simulator to ensure no bugs are present. Tudat unfortunately does not contain a tidal dynamics simulator, at least not coupled with translational and rotational dynamics. Hence, the coupled model must be developed without using Tudat. For the translational-rotational dynamics simulator, Tudat will be used to compute the undamped initial state that will have no normal modes in its propagation, since it has a function that allows to do so, see Section 5.4. It also has functionality regarding the damping of the normal modes in rotational dynamics.

[1] Documentation: https://tudat-space.readthedocs.io. Source code: https://github.com/tudat-team/tudat-bundle.

3

Paper

The following standalone paper contains the main research performed.

On the coupled modelling of the influence of tidal effects in natural satellites' dynamics

Soufyan Roubiou[1]

[1] *Delft university of Technology, Kluyverweg 1, Delft, 2629HS, The Netherlands*

Context. Future missions like JUICE and Europa Clipper are set to increase the quality and quantity of measurements through improved instruments and new estimation methods, resulting in improved orbit determination and parameter estimation. To exploit the data to its fullest, the underlying dynamical models must be improved. To obtain consistent estimates of physical parameters driving long-term evolution of planetary systems from spacecraft data, a satellite's orbit, rotation and tidal deformation must be consistently modelled. While approximations exist to do so for natural satellites, these very same approximations fail when applied to a spacecraft, hence possibly causing inconsistent estimates from the spacecraft data and calling for a coupled modelling approach.
Aims. This works aims to develop a fully coupled model and compare it to simpler, uncoupled implementations and leverage this comparison to analyse the effect of tides on a planetary system's orbital evolution.
Methods. A complete and consistent modelling of a satellite's orbit, rotation and tidal deformation of the gravity field, novel for the field of natural satellites' dynamics, is introduced and applied to the Earth-Moon system as a test case. It is a good candidate because it is a well-known system and the coupled model does not rely on severe underlying assumptions, making it easily applicable to other planetary systems.
Results. For the same initial state, the uncoupled and coupled trajectories show an along-track position difference up to 20 m over 13 years and 8 months. Furthermore, for the tides raised on the Moon by itself, the coupled model predicts values for the orbital evolution in agreement with simplified, uncoupled models available in literature. It also helps shed light on a common discussion between approximations for the evolution of the semi-major axis of a satellite. The orbital energy dissipated $\dot{E}_{orb}$ from the coupled model agrees well with theory, with the values being -14.89 GJ/s and -14.44 GJ/s respectively, although tidal dissipation manifests itself differently in the coupled model. The results in this work show that for the coupled model it is the periodic variations of the degree two coefficients that are solely responsible for the orbital energy dissipated, with no 'constant offset' accompanying the tidal dissipation. The results in this work demonstrate the suitability of the proposed coupled implementation for future missions and data analyses, which has the advantage of circumventing most of the practical and theoretical limitations of current, uncoupled models.

I. INTRODUCTION

The determination of satellites' ephemerides provide information about the formation and evolution of planetary systems by extracting key information on the properties of the bodies in the planetary system, such as their composition, interior structure and rheology (e.g., Lainey et al. (2007); Lainey et al. (2012); Folkner et al. (2014); Dirkx et al. (2016)). A rheology model is a way to model the body's deformation and response to any stresses applied. Accurate natural satellite ephemerides carry importance with it for scientific missions; knowing the positions of celestial bodies currently, and, more importantly, knowing where they *will* be at a later time, is relevant for mission design (for example, for flyby's) and orbit navigation of artificial satellites.

With the launch of satellites like Europa Clipper (Pappalardo et al. (2024)) and JUICE (Grasset et al. (2013), Dirkx et al. (2017)) the accuracy of observational data for certain bodies is set to increase beyond the level of accuracy of state-of-the-art dynamical models (e.g., Dirkx et al. (2016), Fayolle et al. (2023), Magnanini et al. (2024)) due to development of new observation methods (e.g., Dirkx et al. (2019)) and better instruments (e.g., Dirkx et al. 2017).

Ideally, the error arising from the mis-modelling in the underlying dynamical models should be substantially smaller than for the observations. As a result, dynamical models need to be improved in two areas. Firstly, higher fidelity models may be required to exploit the data quality to its fullest. Secondly, and maybe more importantly, the modelling of tides is crucial, especially in the context of these missions. They are imperative to investigate the long-term evolution of a system: tides affect both the spacecrafts and the orbits of natural satellites themselves. The effects of tides on the satellites' orbits are extremely sensitive to the modelling of the satellite's translational and rotational motion, which calls for a coupled modelling approach.

Traditionally, the most extensive dynamical models concurrently propagate the translational and rotational dynamics, while approximating the effect of tides using a tidal force (e.g., Park et al. 2021) (i.e. the deformation of extended bodies' gravity field due to gravitational forcing); this model is only consistently used for the calculation of the ephemeris of the Moon. Developments throughout history have seen the effect of tides on a body's dynamics be modeled in various ways. Kant (1754) introduced the concept of tidal dissipation, an effect caused by the tides raised on Earth due to gravita-

tional forcing of the Moon, that slows the Earth's rotation. The deformation of bodies due to a tide-generated disturbing potential is not instantaneous, because bodies are not perfectly elastic; rather, its behaviour can conveniently be approximated with a tidal *time lag* between the time t at which a disturbing potential exerts a force on the perturbed body, and the time $t + \Delta t$ at which the perturbed body actually experiences the force and deforms accordingly. In reality the deformation cannot be modelled with a constant Δt, as will be elaborated upon in the next paragraphs.

Darwin (1880) modelled this tidal dissipation by assuming a homogeneous Earth consisting of an incompressible fluid with constant viscosity (e.g., Correia et al. 2014), from which he derived an expression for the tide-generated disturbing potential raised on a body expanded as a Fourier series. The work of Darwin laid the foundation for the modelling of tidal dissipation, and many authors have since improved upon this work, with the most notable being the introduction of frequency dependency in the expression for the disturbing potential by Kaula (1964).

The tidal lag depends on a body's interior's rheological properties, and hence, different bodies will have different frequencies at which their tidal forcing is exerted on a perturbed body. Kaula (1964) introduced frequency dependency in the expression by allowing the time lag to be frequency dependent. Many authors have tried to simplify this model, with the most well known being the constant phase lag and constant time lag models; these models however rely on much disputed simplifying assumptions (e.g., Efroimsky et al. 2013).

Crucially, the time lag of the tidal forcing of a body is *not* constant, despite approximations of the time lag using constant values (e.g., Lainey et al. (2007), Efroimsky et al. (2013), Lari (2018)). In some scenarios a constant time lag can be a reasonable assumption, such as for more massive central bodies and satellites in a (near-)circular orbit. However, for eccentric satellites, and *especially* synchronous satellites in an eccentric orbit, it becomes crucial to account for the variability in Δt. Non-circularity leads to an infinitude of forcings. Furthermore, tidal dissipation is the driving factor behind orbital migration of natural satellites (e.g., Lainey et al. (2009), Dirkx et al. (2017)). As a result, when the semi-major axis a of a satellite changes, the frequency of the tidal forcing changes and hence the time lag will vary too; the body's viscoelastic response to tidal forcing is frequency dependent. The influence of tidal effects on the gravity field of synchronous satellites is not easily determined with current expressions for the tidal force as they are extremely sensitive to the rotation rate of the satellite (e.g., Efroimsky (2012), Fayolle (2025)), making it absolutely crucial that the modelling of tides and rotation is consistent; any inconsistencies would result in an erroneous residual tidal torque over one orbit. This breaks the conservation of angular momentum and generates a secular along-track drift, which has a very similar signature as tidal dissipation on the satellite's orbit (e.g., Souchay et al. (2013), Fayolle (2025)). A widely used trick used by Murray et al. (1999) offers a way to circumvent this consistency issue by creating a force formulation independent of the rotation rate. While this has been a useful strategy until now, it raises another problem for future missions like JUICE and Europa Clipper. The spacecrafts are affected by tides in two different ways: through the moon's orbit as well as through the time variations of the moon's gravity field. However, the force formulation introduced by Murray et al. (1999) is specifically designed to model the effects of satellite tides on its own orbit, and does not model the effects of tides from the moon's gravity field. In order to obtain good estimates of tidal dissipation parameters from these missions, it is vital that both effects are modelled consistently. This is something current models fail to do, and calls for a coupled modelling approach.

In an attempt to create a complete and consistent dynamical model for a body including tidal deformations of the gravity field, Correia et al. (2014) and Boué et al. (2016) model the instantaneous deformation of the gravity field due to a tide-raising body using a differential equation for the gravity field coefficients. This allows for concurrent propagation of the translational and rotational dynamics including tidal deformation of the gravity field. The effects of tides are thus entirely modelled through the variations of the body's gravity field that they induce, making for a model that is consistent in modelling the orbit, rotation and tidal response of a body. This model furthermore does not rely on an additional tidal force term acting on the orbit and the simplifications necessary.

It hence becomes a good candidate for a more accurate dynamical model - especially in the given context of future missions - by, theoretically, having a decreased mis-modelling with reality by providing a complete and consistent modelling of the orbit, rotation and tidal deformation of the gravity field of a satellite. Since the model does not require a tidal force acting on the orbit, it also does not depend on any of the simplifying assumptions that have been made in the derivation of the tidal force (e.g., Darwin 1880), making it very generally applicable. It only requires the modelling of the rheology of a body.

Correia et al. (2014) and Boué et al. (2016) test this model for long-term propagations of exoplanets. Short-term propagations have not yet been performed using this model, but are of interest for future missions. The novel use of this model in the field of natural satellite dynamics will mostly lend itself to relatively short-term propagations. As a result, while the coupled model ensures consistent frequency dependence of the tidal response of a body over time, it is not the primary benefit for future missions. This work will apply this model to the Earth-Moon system. Since the coupled model has no significant underlying assumptions, the model can easily be extended to other planetary systems regardless of the

specifics of the orbit (eccentricity of the orbit, rotation rates, etc.) making the specifics of the planetary system considered less relevant to an extent, and the general tidal behaviour more so. Furthermore, the Earth-Moon system is a relatively stable and very well known system, allowing for the results of the coupled model to be compared to theoretical approximations and known literature. This work analyzes the effect of the introduced couplings and investigates to what extent tidal dissipation is properly emulated, with the goal of determining whether implementing such a dynamical model is a worthwhile investment for the data analysis of future mission data. It also offers more detailed insights into how tides affect the orbit of a synchronous satellite, using a more complete and consistent modelling approach.

Section 2 introduces the dynamical model used in this work, along with formulations for the uncoupled and coupled approaches. Subsequently, Section 3 introduces theoretical equations and definitions used in the validation of the dynamical model. Section 4 will present the results. Lastly, Section 5 and Section 6 will discuss the results and place it in context of future missions and finally conclude this work.

II. DYNAMICAL MODEL

This chapter describes the translational and rotational dynamics of natural satellites using equations of motion. It furthermore introduces the effect tides have on the dynamics of natural satellites. Lastly, this section will cover both the uncoupled and coupled modelling approaches by introducing decoupled and coupled sets of equations of motion to model the dynamics of bodies.

A. Reference frame definitions

To start, for the sake of clarity some nomenclature and reference frames that will be used throughout this work are introduced.

The motion of the Earth and the Moon will be described with respect to the other; if the Moon is propagated, a quasi-inertial reference frame will be centered on the Earth and vice versa. The orientation of this reference frame is inertial. Each body is also assigned a body-fixed reference frame, with its origin at the center of mass. The orientation of the axes of the reference frame is not constrained.

A vector $\boldsymbol{x}$ going from a body i to a body j in the body-fixed frame of i is expressed as $\boldsymbol{x}_{ij}$. A subscript i in the gradient ∇_i indicates that the gradient is taken with respect to coordinates associated with the body-fixed frame of body i, requiring a rotation matrix $\boldsymbol{R}^{I/i}$ to convert results to a common, inertial frame. Lastly, a gradient in the inertial reference frame is written as ∇.

B. Gravitational interactions

Following Correia et al. (2014), a simplified Earth-Moon system is considered with no perturbations. Consider a body-fixed reference frame ($\boldsymbol{I}$, $\boldsymbol{J}$, $\boldsymbol{K}$) centered on body i. It is assumed that the rotation rate Ω of the body is along $\boldsymbol{K}$ and that $\boldsymbol{K}$ is orthogonal to the orbital plane, implying zero obliquity (i.e. the equatorial plane and the orbital plane coincide). The setting of this problem is displayed in Fig. 1 and discussed in Correia et al. (2014). The inertial frame and body-fixed frame have the same origin.

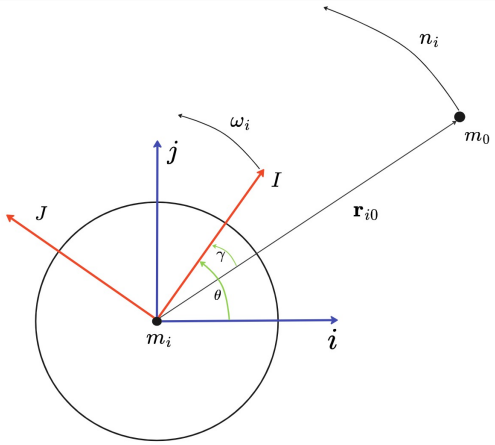

Figure 1: Schematic overview of the extended two-body problem with central body 0 and perturbing body i. The reference frames $\boldsymbol{F_I} = (\boldsymbol{i}, \boldsymbol{j}, \boldsymbol{k})$ and $\boldsymbol{F_i} = (\boldsymbol{I}, \boldsymbol{J}, \boldsymbol{K})$ are introduced, where $\boldsymbol{F_i}$ is fixed to body i and rotating with angular velocity $\boldsymbol{\omega}_i$. $\boldsymbol{r}_{i0}$ is the position vector going from i to 0, n_i is the mean motion of body 0 in the frame of body i and θ and γ are the rotation angle between the reference frames and the angular direction of body 0 as seen from F_i respectively.

In the following equations, U_i is the gravitational potential of body i and is expressed using spherical harmonic expansions. U_i can, outside its smallest circumscribing sphere, be expressed as (e.g., Dirkx et al. 2019)

$$U_i(\boldsymbol{r}) = U_i(r, \vartheta, \phi) = \frac{\mu_i}{r} \sum_{l=0}^{\infty} \sum_{m=0}^{l} \left(\frac{R_i}{r}\right)^l \times P_{l,m} \sin(\phi)(C^i_{l,m} \cos(m\vartheta) + S^i_{l,m} \sin(m\vartheta)). \quad (1)$$

r, ϑ and ϕ are the distance to the origin, the body-fixed longitude and body-fixed latitude of the position vector $\boldsymbol{r}$. They express the position at which the potential is evaluated in a body-fixed frame attached to body i in spherical coordinates. μ_i and R_i are the gravitational parameter and the reference radius of body i. $P_{l,m}$ are the associated unnormalized Legendre polynomials of degree l and order m and $C^i_{l,m}$ and $S^i_{l,m}$ are the associated unnormalized cosine and sine coefficients.

The spherical harmonic expansion is truncated to degree 2 for this work, as for most natural satellites (such as the Galilean moons) only the degree 2 gravity field coefficients are known. The terms for $l = 1$ drop off if the body-fixed reference frame is centered on the center of mass of the body, a common assumption (Murray et al. (1999)). Furthermore, $S_{2,1}$ and $C_{2,1}$ are equal to 0 when the body has a rotational symmetry about its polar axis, which is assumed here. Through similar reasoning $S_{2,2}$ can be assumed equal to zero on average, but it will still be included because tidal effects will be modelled through gravity field variations which can be non-zero. Furthermore, $S_{2,2}$ and tidal dissipation have very similar signatures in natural satellites' dynamics, making it critical to include. This will be elaborated upon in Section 2.4.

Fundamentally, the acceleration exerted on body 0 by the gravitational potential of body i in a common inertial frame can be described by Newton's second law:

$$\ddot{\boldsymbol{r}}_{i0} = \boldsymbol{R}^{I/i} \nabla_i U_i(\boldsymbol{r}_{i0}), \tag{2}$$

where $\ddot{\boldsymbol{r}}_{i0}$ is the second time-derivative of $\boldsymbol{r}_{i0}$. Assuming the body-fixed latitude at which the potential is evaluated equal to zero, the acceleration between central body 0 and perturbing body i is given as (e.g., Correia et al. 2014)

$$\begin{aligned}\ddot{\boldsymbol{r}}_{i0} = R^{I/i} \cdot \Big(&-\frac{\mu}{r_{i0}^2}\hat{\boldsymbol{r}} - \frac{3\mu R_i^2}{2r_{i0}^4} J_2^i \hat{\boldsymbol{r}} \\ &- \frac{9\mu R_i^2}{r_{i0}^4}(C_{2,2}^i \cos 2\gamma_0 - S_{2,2}^i \sin 2\gamma_0)\hat{\boldsymbol{r}} \\ &- \frac{6\mu R_i^2}{r_{i0}^4}(C_{2,2}^i \sin 2\gamma_0 + S_{2,2}^i \cos 2\gamma_0)\hat{\boldsymbol{\vartheta}}\Big),\end{aligned} \tag{3}$$

where $\hat{\boldsymbol{r}}$ and $\hat{\boldsymbol{\vartheta}}$ correspond to the radial and tangential unit vectors in the body-fixed frame and where $\mu = G(m_i + m_0)$.

A second, more complex situation arises when the effect of perturbations on the Earth-Moon system are included. Eq. 3 does not hold anymore since the latitude varies now, so Eq. 1 is used to derive the complete potential for $l_{max} = 2$. Then, a full expression for the acceleration any body i experiences in a planetary system can be given. Consider the case of a moon i orbiting a central body 0 along with other bodies j, the total acceleration exerted on body i can then be given as

$$\ddot{\boldsymbol{r}}_i = R^{I/0}\left((\ddot{\boldsymbol{r}}_{0i})_0 + \sum_j^{j\neq i,0} (\ddot{\boldsymbol{r}}_{ji})_0\right), \tag{4}$$

This work includes the point mass accelerations exerted on the Earth-Moon system by the Sun and Jupiter. The explicit expression of the acceleration acting on the Moon is given in Appendix A.

Where accelerations govern the translational state, torques dictate how the rotational state of the body evolves. The gravitational torque driving the rotational evolution of the satellite i is exerted by the central body 0 on the non-spherical shape of the satellite. For the general case of an extended body i, the gravitational torque exerted by N bodies in the frame of body i can be described as

$$\bar{\boldsymbol{\Gamma}}_i^{(i)} = -\sum_j^N m_j \boldsymbol{r}_{ij} \times (\nabla_i U_i(\boldsymbol{r}_{ij})). \tag{5}$$

where $\bar{\boldsymbol{\Gamma}}_i^{(i)}$ is the gravitational torque exerted by N bodies on body i, in the reference frame of body i.

In this work, a quaternion $\boldsymbol{q}$ is used to express the orientation of a body. Following Fukushima (2008), the time derivative of $\boldsymbol{q}$ is given as

$$\dot{\boldsymbol{q}}_i = \boldsymbol{Q}(\boldsymbol{q}_i)\boldsymbol{\omega}_i, \tag{6}$$

$$\boldsymbol{Q}(\boldsymbol{q}) = \frac{1}{2}\begin{bmatrix} -q_1 & -q_2 & -q_3 \\ q_0 & -q_3 & q_2 \\ q_3 & q_0 & -q_1 \\ -q_2 & q_1 & q_0 \end{bmatrix}, \tag{7}$$

with $\boldsymbol{\omega}_i$ the rotation rate of body i. $\boldsymbol{\omega}_i$ is governed by the Euler equation, which, for a non-rigid body in rotation experiencing torques, is given as (e.g., Dirkx et al. 2019)

$$\dot{\boldsymbol{\omega}}_i = \boldsymbol{I}_i^{-1} \cdot (\bar{\boldsymbol{\Gamma}}_i^{(i)} - \dot{\boldsymbol{I}}_i\boldsymbol{\omega}_i - \boldsymbol{\omega}_i \times (\boldsymbol{I}_i\boldsymbol{\omega}_i)). \tag{8}$$

Here, $\boldsymbol{I}_i$ and $\dot{\boldsymbol{I}}_i$ are the inertia tensor and its derivative of body i. When only degree 2 gravity field coefficients are considered, the following relation exists between $\boldsymbol{I}_i$ and these equations (e.g., Lambeck 1980):

$$\boldsymbol{I}_i = m_i R_i^2 \begin{pmatrix} \frac{C_{20}^i}{3} - 2C_{22}^i & -2S_{22}^i & -C_{21}^i \\ -2S_{22}^i & \frac{C_{20}^i}{3} + 2C_{22}^i & -S_{21}^i \\ -C_{21}^i & -S_{21}^i & -\frac{2C_{20}^i}{3} \end{pmatrix} + \bar{I}_i \mathbf{1}_{3x3}, \tag{9}$$

with $S_{2,1}^i = 0$ and $C_{2,1}^i = 0$ and for the given assumptions and $\bar{I}_i$ the normalized mean moment of inertia.

C. Tides

The equations derived in the last section assume rigid bodies in their derivations - which is true of the gravity field coefficients are constant - thus neglecting tidal effects that have an influence on the time-variability of the gravity field. However, tides play a crucial role in

the long-term orbital evolution of natural satellites, and hence are a key part of natural satellite dynamics in the context of future missions. This section introduces the concept of the tides and the tidal potential, which sets up one way the effect of tides is approximated in current, simplified models.

Tidal deformations express themselves in variations in the mass distribution, and thus the gravity field, shape and rotation. For the body i, the tidal deformations induced by the perturbing body j are determined by the tidal potential $U_j^T(\boldsymbol{r})$ and the tidal Love numbers $k_{l,m}^i$ of i, where l and m are the degree and order of the spherical harmonic expansion. The gradient of the tidal potential yields the tidal force, which dictates the relative motion between two points on body i, resulting in tides. $k_{l,m}^i$ describe the body's response to tidal forcing. They are frequency-dependent complex numbers; the imaginary part defines the phase lag of the tidal response. Approximating body j as a point mass allows the tidal potential of body j to be given as (e.g., Kaula 1964):

$$U_j^T(\boldsymbol{r}) = \frac{Gm_j}{r_{ij}} \sum_{l=2}^{\infty} \left(\frac{|\boldsymbol{R}|}{r_{ij}}\right)^l P_l(\cos(\Psi)), \qquad (10)$$

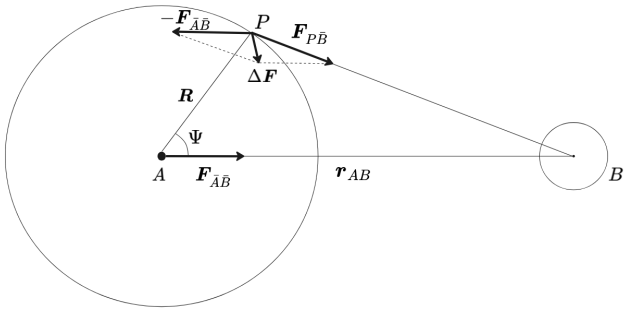

Figure 2: Schematic decomposition of the gravitational force exerted by body B, where the difference between $\boldsymbol{F}_{P\bar{B}}$ and $\boldsymbol{F}_{\bar{A}\bar{B}}$ is responsible for the tidal force $\Delta\boldsymbol{F}$. $\boldsymbol{R}$ is the position vector pointing to point P and $\boldsymbol{r}_{AB}$ is the vector connecting the centers of A and B, and Ψ is the angle between $\boldsymbol{R}$ and $\boldsymbol{r}_{AB}$.

where $\boldsymbol{R}$ is a position vector from the center of the body to a surface point and Ψ is the angle between $\boldsymbol{R}$ and $\boldsymbol{r}_{ij}$, see Fig. 2. P_l are the Legendre polynomials of degree l. Apart from deformations due to external forces, body i also deforms under its own centrifugal potential caused by its rotation (Murray et al. (1999), Correia et al. (2013)). The induced gravitational potential on body i, $\delta U_{i,l}(\boldsymbol{r})$, and, when expanded, $\delta U_{i,l,m}(\boldsymbol{r})$ then depends on both the centrifugal potential $U_i^{cf}(\boldsymbol{r})$ and $U_j^T(\boldsymbol{r})$:

$$\begin{aligned}\delta U_{i,l,m}(\boldsymbol{r}) &= \left(\frac{|\boldsymbol{R}|}{|\boldsymbol{r}|}\right)^{l+1} k_{l,m}^i U_{l,m}^{'}(\boldsymbol{r}) \\ &= \left(\frac{|\boldsymbol{R}|}{|\boldsymbol{r}|}\right)^{l+1} k_{l,m}^i (U_{i,l,m}^{cf}(\boldsymbol{r}) + U_{j,l,m}^T(\boldsymbol{r})), \qquad (11)\end{aligned}$$

Eq. 1 and Eq. 10 substituted in Eq. 11 can, when neglecting the centrifugal potential -which is often done - be expanded into a series, yielding the time-variable spherical harmonic coefficients (e.g., Petit et al. 2010):

$$\begin{aligned}\Delta\bar{C}_{l,m}^i - i\Delta\bar{S}_{l,m}^i = \frac{k_{l,m}^i}{2l+1} \times \\ \times \sum_j \frac{\mu_j}{\mu_i} \left(\frac{R_i}{r_j}\right)^{l+1} \bar{P}_{l,m}(\sin\phi_j) e^{-im\vartheta_j}, \qquad (12)\end{aligned}$$

where the summation runs over j bodies that raise a tide on body i. Eq. 12 is a common representation, especially in the field of gravity field analyses, of the variations in the gravity field coefficients $C_{l,m}^i(t)$ and $S_{l,m}^i(t)$ of a body i under the tidal influence of j other bodies.

For (almost) synchronous bodies, the coefficients consist of a large static component and a small varying component, where $C_{l,m}^i(t) = C_{l,m}^{i,0} + \Delta C_{l,m}^i$ and $S_{l,m}^i(t) = S_{l,m}^{i,0} + \Delta S_{l,m}^i$, giving rise to a large permanent tide and a relatively small varying tide, since θ and ϕ are constant to first-order approximation, specifically for synchronously rotating bodies. Hence, measuring varying tides is more difficult for synchronously rotating bodies than it is for non-synchronously rotating bodies as the static and time-varying components must be separated.

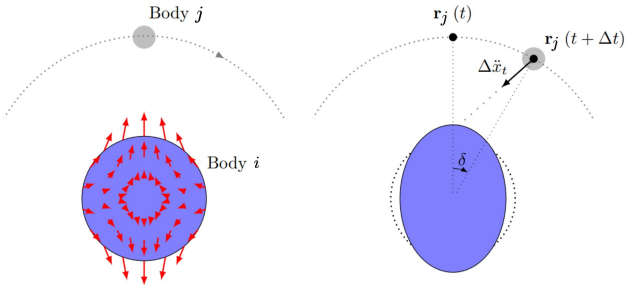

Figure 3: Left: Schematic overview of tide-generating body j and the tidal deformation of body i. Right: Time-lag between perturbing potential and the raised tide on body i, quantified by a lag angle δ. This gives raise to an additional acceleration $\Delta\ddot{x}_t$ exerted on j by the induced gravitational potential of i. This figure has been adopted from Dirkx (2015).

Eq. 11 implicitly assumes body i to be elastic and its response instantaneous, which is generally not true. Fig. 3 displays how the response and induced tidal deformation might actually look. The tidal deformation caused

by body j raises an additional tidal potential for body i as in Eq. 11, which again exerts an influence on body j. In reality, body i's response to this perturbing potential is not instantaneous, but rather, it takes time for it to deform due to its viscosity; its response is viscoelastic. As a result, there is a time lag between the perturbing potential and the raised tide, which in turns gives raise to a tidal geometric lag angle δ. An exaggerated depiction is shown in Fig. 3.

This effect is commonly expressed through a quality factor Q, which is defined as (e.g., Khan et al. 2004):

$$Q_i^j = \frac{|k_2^i|}{\mathrm{Im}(k_2^i)}, \tag{13}$$

where $\mathrm{Im}(k_2^i)$ specifies the imaginary part of k_2^i (See Appendix B for an explanation how the imaginary part of k_2^i quantifies the tidal lag). It is common practice to simplify the Love numbers to k_l (e.g., Zhang (1992); Williams et al. (2015)), as variations of k in m for a set l caused by the body's asphericity are typically small. The imaginary part quantifies the tidal lag δ, resulting in tidal dissipation. Q is frequency-dependent and depends on the body's rheology, and is used to signify what a body's tidal response may look like (e.g. it defines the amount of energy dissipated in the system) (e.g., Efroimsky et al. 2007). Q_i^j then denotes the quality factor of body i at the forcing frequency of the tides raised by body j. The time lag in raising the tidal bulge due to the viscoelastic response is dependent on Q and given as (e.g., Lainey et al. 2007):

$$\Delta t_i^j = \frac{T_i^j \sin^{-1}(1/Q_i^j)}{2\pi}, \tag{14}$$

where Δt_i^j is the time lag and T_i^j refers to the period of the forcing, for which the expressions are given in Lainey et al. (2007). For a synchronous satellite, its forcing period is - different from a central body - equal to its rotational period, which is why the effect of tides on satellites is different from central bodies, and results in difficulties when trying to model tidally-locked satellites.

D. Decoupled model

Having introduced the concept of tides and the tidal potential in the last section, this section introduces the tidal force and gives the equations of motion for the decoupled model. Furthermore, the limitations of the current model and the effects thereof will be discussed, providing context for the introduction of the coupled model.

Assuming that the body's tidal response is linear (e.g. no higher order terms are considered) and isotropic in its body-fixed frame, an expression can be found for the induced gravitational potential at time t (see Eq. 19). From this expression an expression for the tidal force can be derived by assuming a constant time lag, meaning that the induced tidal potential at time t is generated by a perturbing potential at $t - \Delta t$, with Δt the time lag (e.g., Efroimsky et al. 2013). The tidal force F_i^j, when reduced to degree $l = 2$, can then be given as (e.g., Lainey et al. 2007):

$$\boldsymbol{F}_i^i = -\frac{3Gm_0^2 k_2^i R_i^5}{|\boldsymbol{r}_{i0}|^8}\left(\boldsymbol{r}_{i0} + \Delta t_i^0 \times \right. \\ \left. \times \left(\boldsymbol{r}_{i0} \times \boldsymbol{\omega}_i + \boldsymbol{v}_i + \frac{2}{|\boldsymbol{r}_{i0}|^2}(\boldsymbol{r}_{i0} \cdot \boldsymbol{v}_i)\boldsymbol{r}_{i0}\right)\right). \tag{15}$$

for the tides raised on the satellite i by the itself, where $\boldsymbol{v}_i$ denotes the velocity vector of body i. By Newton's third law, the satellite will also raise tides on the central body, with the magnitude of the force being same but the direction opposite of the force in Eq. 15. This equation is preferred over using Eq. 12 with Eq. 3 in the field of natural satellites' dynamics due to its relative simplicity and low computational complexity.

Applying Eq. 15 to model the tides on a satellite is, however, not straightforward due to the intricate dependency between the tides and rotation. Since any mismodelling of the tides may result in a residual tidal torque over one orbit, applying this expression may result in the wrong amount of energy being dissipated, and thus result in a non-physical contribution to the orbital migration of the satellite. To circumvent this, Murray et al. (1999) states that the librational tides dissipate exactly 4/3 times as much energy as the radial tides. Following Lari (2018), the tidal force due to the radial tides is retrieved by substituting $\boldsymbol{\omega}_i = \boldsymbol{r}_{i0} \times \boldsymbol{v}_i / |\boldsymbol{r}_{i0}|^2$ in Eq. 15. Adding 4/3 times this force from the librational component results in

$$\boldsymbol{F}_i^i = -\frac{3Gm_0^2 k_2^i R_i^5}{|\boldsymbol{r}_{i0}|^8}\left(\boldsymbol{r}_{i0} + \Delta t_i^0 \times \right. \\ \left. \times \left(\frac{7}{|\boldsymbol{r}_{i0}|^2}(\boldsymbol{r}_{i0} \cdot \boldsymbol{v}_i)\boldsymbol{r}_{i0}\right)\right). \tag{16}$$

This circumvents the need to use the rotation rate to calculate the tidal force and results in, after averaging, the right amount of energy dissipated over one orbit. Due to the previous discussion, Eq. 16 is an attractive way to model the satellite's natural dynamics and is done so in both ephemeris and natural satellite dynamics studies (e.g., Lainey et al. (2007), Lari (2018), Fayolle (2025)).

However, while this expression works to model the effect on the satellite's orbit of the tides raised on the it by itself, it fails for spacecrafts like JUICE and Europa Clipper. Since it cannot model the effect of the time-varying gravitational potential as measured by the spacecraft, an inconsistency arises between the models applied. As mentioned before, this may result in erroneous residual torques which may influence the measurements aboard the spacecrafts; it is especially a big issue

for radio-science analyses. Furthermore, albeit less relevant for this work, it also poses a problem for long-term dynamical modelling. Since the orbit expands or shrinks due to tidal dissipation, the frequency of the tidal forcing, and thus Q_i^j, will change, as follows from Eq. 13. As a result, the amount of tidal energy the system will dissipate also changes over time. These issues call for the need of a more sophisticated coupled modelling approach to ensure full consistency between the orbit, rotation and tides of both the satellites and spacecrafts.

The additional torque induced by the tidal bulge raised on the satellite influences the rotational dynamics of the system (more specifically, it induces a transfer in energy and angular momentum between the two bodies), and can be expressed as:

$$\boldsymbol{\Gamma}_i^i = \boldsymbol{r}_{i0} \times \boldsymbol{F}_i^0 = -\frac{3Gm_i^2 k_2^0 R_i^5}{|\boldsymbol{r}_{i0}|^8}\Delta t \times \\ \times ((\boldsymbol{r}_{i0}\cdot\boldsymbol{r}_{i0})\boldsymbol{\omega}_i - \boldsymbol{r}_{i0}(\boldsymbol{r}_{i0}\cdot\boldsymbol{\omega}_i) - \boldsymbol{v}_i|\boldsymbol{r}_{i0}|^2 + \boldsymbol{r}_{i0}\times\boldsymbol{v}_i). \tag{17}$$

This torque gives rise to a change in $\boldsymbol{\omega}_i$ while simultaneously also depending on $\boldsymbol{\omega}_i$. This again reiterates the importance of accurately modelling the rotation rate of the satellite for accurate propagation of the satellite's dynamics. To this end, it may be beneficial to instead model the gravity field coefficients as a differential equation, and introduce a fully coupled model between the translational, rotational and tidal dynamics.

E. Coupled model

In this section, a differential equation -based on the work of Correia et al. (2014) and Boué et al. (2016) - that governs the evolution of the gravity field coefficients is introduced, removing the need for a direct tidal force expression. Through this differential equation a body's dynamics are influenced, directly incorporating any influence tides would have on its dynamics. The problems mentioned in last section, such as the extreme sensitivity of the tidal force expressions to the rotation rate of the satellite and the resulting approximations necessary to apply it to the satellite's dynamics are circumvented using this method, while it also allows for a more complete modelling of the body's frequency-dependent response to tidal forcing.

1. *Rheology*

As mentioned repeatedly, using the tidal force to express tides as in Eq. 15 is an approximation (e.g., Efroimsky et al. 2013) and to properly model the response of a body to tidal forcing an adequate rheology model is necessary. For natural satellites in a spin-orbit resonance, a *viscoelastic* model is used to model their response to stress. Whether the body responds as a viscous fluid or elastic solid then depends on the frequency of the perturbation. One of the simplest forms is to consider that the body behaves like a Maxwell material. The Maxwell model has been used numerous times before to describe a planetary body's structure and its response to forces applied to it (e.g. Correia et al. (2014), Ferraz-Mello (2015), Boué et al. (2016)), making it a relatively well known model. Following Turcotte et al. (2002), the Maxwell model describes the body's response by the following relation (e.g., Henning et al. 2009):

$$\frac{d\epsilon}{dt} = \frac{1}{\mu_0}\frac{d\sigma}{dt} + \frac{\sigma}{\eta}, \tag{18}$$

which describes the body's response by a purely viscous damper with viscosity η and a purely elastic spring with modulus μ_0 connected in series, with ϵ the strain and σ the stress applied to the body.

2. *Gravity field coefficients in a differential equation*

Eq. 11 assumes a body deforms instantaneously under applied stress, but since bodies are visco-elastic in reality the expression becomes a convolution. Assuming that the body's tidal response is linear (e.g. no higher order terms are considered) and isotropic in its body-fixed frame, a body i's induced gravitational potential at time t, $\delta U_i(\boldsymbol{r},t)$ (note the explicit time-dependence now) depends linearly on all past tidal perturbations with $t' \leq t$, $U_0^{'}(\boldsymbol{r},t')$, giving raise to a convolution (e.g., Boué et al. 2016):

$$\delta U_i(\boldsymbol{r},t) = \sum_{l=2}^{\infty}\delta U_{0,l}(\boldsymbol{r},t) \tag{19}$$

$$= \sum_{l=2}^{\infty}\left(\frac{|\boldsymbol{R}|}{|\boldsymbol{r}|}\right)^{l+1} k_l(t) * U_{0,l}^{'}(\boldsymbol{r},t) \tag{20}$$

$$= \sum_{l=2}^{\infty}\left(\frac{|\boldsymbol{R}|}{|\boldsymbol{r}|}\right)^{l+1}\int_{-\infty}^{t} k_l(t-t')U_{0,l}^{'}(\boldsymbol{r},t')\mathrm{d}t', \tag{21}$$

When a body's response is assumed to behave like a Maxwell model, one can simplify the convolution by transforming the equation into the Fourier domain, yielding a point-wise multiplication. By following the steps performed by Correia et al. (2014) in his work, this eventually results in a differential equation for the l-th term of the induced gravitational potential:

$$\delta U_l + \tau_l \delta\dot{U}_l = k_l^0(U_l^{'} + \tau_e\dot{U}_l^{'}), \tag{22}$$

with τ_l and τ_e the global and Maxwell relaxation times and k_l^0 the fluid Love number. They are properties of a body and express how it responds to an applied stress.

The induced potential δU is again caused by the perturbing tidal potential $U^{'}$. Eq. 22 shows that when $\tau_l = \tau_e = 0$, the raised potential reduces to an equilibrium potential δU_l^e - i.e. the response is instantaneous or there is a static perturbation as in Eq. 11 - defined as:

$$\delta U_l^e = k_l^0 U_l^{'}. \tag{23}$$

Substituting Eq. 23 in Eq. 22 then expresses the instantaneous variation of the induced potential as a function of the equilibrium potential:

$$\delta U_l + \tau_l \delta \dot{U}_l = \delta U_l^e + \tau_e \delta \dot{U}_l^e. \tag{24}$$

The relaxation times τ_l and τ_e can be related to k_2 and Q as introduced in Section 2.3 - for $l = 2$, so it follows that τ_l simplifies to τ_2 - and:

$$k_2 = k_2^0 \sqrt{\frac{1 + \tau_e^2 \chi^2}{1 + \tau_2^2 \chi^2}}, \tag{25}$$

$$\tan\left(\arcsin\left(\frac{1}{Q}\right)\right) = \tan\delta = \frac{(\tau_2 - \tau_e)\chi}{1 + \tau_2 \tau_e \chi^2}, \tag{26}$$

$$\frac{k_2}{Q} = k_2^0 \frac{(\tau_2 - \tau_e)\chi}{1 + (\tau_2 \chi)^2}. \tag{27}$$

The differential equation as defined in Eq. 24 governs the instantaneous change in the induced gravitational potential, described by the gravity field coefficients, that follows from any perturbing potential. Since these gravity field coefficients are decomposed in spherical harmonics and the spherical harmonic functions form an orthogonal basis, the differential equation as defined for the induced gravitational potential must also hold for the gravity field coefficients (e.g., Correia et al. 2014). For convenience, these differential equations can also be noted down as one equation by introducing the notation:

$$Z_{l,m} = C_{l,m} - iS_{l,m} \quad \text{and} \quad Z_{l,m}^e = C_{l,m}^e - iS_{l,m}^e. \tag{28}$$

Since Eq. 24 holds for $C_{l,m}$ and $S_{l,m}$, it will also hold for any linear combination of them, thus (e.g., Boué et al. 2016):

$$Z_{l,m} + \tau_l \dot{Z}_{l,m} = Z_{l,m}^e + \tau_e \dot{Z}_{l,m}^e, \tag{29}$$

where $Z_{l,m}^e$ is the coefficient at equilibrium. Following Ferraz-Mello (2015) and Boué et al. (2016), Eq. 29 can be conveniently reordered to

$$Z_{l,m} = \left(1 - \frac{\tau_e}{\tau_l}\right) Z_{l,m}^\nu + \frac{\tau_e}{\tau_l} Z_{l,m}^e, \quad \text{with} \quad Z_{l,m}^\nu + \tau_l \dot{Z}_{l,m}^\nu = Z_{l,m}^e, \tag{30}$$

ensuring that there is no more dependency on $\dot{Z}_{l,m}^e$ and reducing the equation to a first order differential equation. Note that this differential equation, inherently describing the induced tidal potential, only depends on the body's own rotation vector and the position of the perturbing body through the equilibrium coefficients, meaning that Eq. 30 should hold for any trajectory (both 2-dimensional and 3-dimensional - the formulation of the perturbing potential simply differs), as long as the initial conditions are valid (see Section 2.4). Similarly to Eq. 24, the equilibrium coefficient $Z_{l,m}^e$ is given for a static perturbation or instantaneous response; the love number k_2 then simplifies to k_2^0 for their expressions as the centrifugal potential also results in a static response. For the J_2, $S_{2,2}$ and $C_{2,2}$ coefficients, it follows that their equilibrium values are given as (e.g., Correia et al. 2013):

$$J_2^e(\boldsymbol{\omega}, \boldsymbol{r}) = k_2^0 \left[\frac{\omega_i^2 R_i^3}{3\mu_i} + \frac{1}{2}\frac{m_0}{m_i}\left(\frac{R_i}{|\boldsymbol{r}_{i0}|}\right)^3\right], \tag{31}$$

$$C_{2,2}^e(\boldsymbol{\omega}, \boldsymbol{r}) = k_2^0 \frac{m_0}{4m_i}\left(\frac{R_i}{|\boldsymbol{r}_{i0}|}\right)^3 \cos(2\gamma_0), \tag{32}$$

$$S_{2,2}^e(\boldsymbol{\omega}, \boldsymbol{r}) = -k_2^0 \frac{m_0}{4m_i}\left(\frac{R_i}{|\boldsymbol{r}_{i0}|}\right)^3 \sin(2\gamma_0). \tag{33}$$

3. *Coupled equations of motion*

Having derived a differential equation for the gravity field coefficients, the coupled equations of motion for the unperturbed and perturbed case can be set up. The most general equations are given instead, applicable to any system. Consider a body k undergoing forces from a body 0 and j additional bodies, its dynamics are described by (e.g., Correia et al. (2014), Dirkx et al. (2019)):

$$\dot{\boldsymbol{x}}_t = \begin{bmatrix}\dot{\boldsymbol{r}}_i \\ \dot{\boldsymbol{v}}_i\end{bmatrix} = \begin{bmatrix}\boldsymbol{v}_i \\ \boldsymbol{R}^{I/0}(\boldsymbol{q})\left(\sum_j^{j\neq i}(\ddot{\boldsymbol{r}}_{ji})_0\right)\end{bmatrix}, \tag{34}$$

$$\dot{\boldsymbol{x}}_r = \begin{bmatrix}\dot{\boldsymbol{q}}_i \\ \dot{\boldsymbol{\omega}}_i\end{bmatrix} = \begin{bmatrix}\boldsymbol{Q}_i(\boldsymbol{q})\boldsymbol{\omega}_i \\ \boldsymbol{I}_i^{-1} \cdot (\bar{\boldsymbol{\Gamma}}_i^{(i)} - \dot{I}_i\boldsymbol{\omega}_i - \boldsymbol{\omega}_i \times (I_i\boldsymbol{\omega}_i))\end{bmatrix}, \tag{35}$$

$$Z_{l,m} = \left(1 - \frac{\tau_e}{\tau_l}\right) Z_{l,m}^\nu + \frac{\tau_e}{\tau_l} Z_{l,m}^e \text{for } l = 2 \text{ and } m \in \{0, 2\}, \quad \text{with} \quad Z_{l,m}^\nu + \tau_l \dot{Z}_{l,m}^\nu = Z_{l,m}^e, \tag{36}$$

with $\dot{\boldsymbol{x}}_t$ and $\dot{\boldsymbol{x}}_r$ the translational and rotational state vectors respectively. In summary, the state vector of the problem as introduced in Section 2.1 is given as $y = [\boldsymbol{r},$

$\boldsymbol{v}$, $\boldsymbol{\omega}$, $\boldsymbol{q}$, ΔJ_2^ν, $\Delta S_{2,2}^\nu$, $\Delta C_{2,2}^\nu$]. $\boldsymbol{r}$ and $\boldsymbol{v}$ denote the position and velocity of the perturbing body as seen from the inertial reference frame set in the center of the tidal body (the body experiencing the tides). $\boldsymbol{\omega}$ and $\boldsymbol{q}$ denote the rotation rate and the orientation vector of the tidal body and the gravity field coefficients are given by their relations as described in Eq. 36. Note that the $Z_{l,m}^e$ coefficients are not part of the state vector, as their expressions are retrieved from Eq. 31-33. For this work, these equations have been numerically integrated using a DOP853 integrator working in a fixed-step regime of 160 minutes, resulting in a sub-millimeter accuracy over a propagation period of 500 days.

4. *Initialization of the coupled model*

In order to propagate the coupled equations of motion, an initial state vector must be defined. Not every state vector will lend itself to this purpose. Numerically integrating the rotational equations of motion starting from an arbitrary, undamped initial state will give rise to rotational normal modes; they are non-physical oscillations that occur at the forcing frequency of a body's normal mode, which depends on its interior properties. These normal modes have been assumed to be damped out for the Solar System bodies over a long time scale. In order to damp them in the coupled model, an algorithm as introduced by Rambaux et al. (2012) and implemented by Martinez (2023) is used, which introduces a virtual torque into the equations of motion. This torque is designed to preserve rotation about the z-axis of the body, while damping rotations about the other axes. This torque has however only been applied to a system consisting of rigid bodies, and has been untested for bodies that deform under tidal forces.

Hence, a second step is added to aid in finding a physically realistic initial state. Analogously to how a virtual torque is introduced to damp the rotation, a similar equation should be used to damp the normal modes in the gravity field coefficients, to ensure that the initial values of the rotational state and gravity field coefficients together describe a damped state. The details and results of the algorithm can be found in Appendix D.

III. VALIDATION

Once implemented, the coupled equations of motion Eq. 34-36 can be compared to approximations derived from the simplified, uncoupled tidal force approach for relevant parameters. The goal is to ensure the results of the coupled model are consistent with that of simpler formulations, but also to investigate possible deviations between the coupled and uncoupled model, which could possibly indicate that some (coupled) effects are captured better by the coupled model. This includes the evolution of the semi-major axis a and the eccentricity e of the satellite. Next to that, comparison of the gravity field coefficients with theoretical approximations from Eq. 12 are made in order to evaluate their behaviour under the influence of tidal effects. The tidal lag and lag angle will be compared against approximations. Lastly, the influence of physical librations on the orbital migration of the satellite will be discussed.

A. Linear approximations for the semi-major axis and eccentricity evolution

The resulting tidal torques raised by the planet and satellite tides and the tides themselves induce secular variations in the satellite's semi-major axis a_i and eccentricity e_i (Goldreich et al. (1966)). For the tides raised by the satellite i on the planet 0, the evolution of the semi-major axis and eccentricity are commonly described as (e.g. Souchay et al. (2013), Boué (2019)):

$$\frac{de_i^0}{dt} = \text{sign}\left(3\omega_0 - 2n_i\right)\frac{57}{8}\frac{k_2^0 m_i}{Q_0^i m_0}\left(\frac{R_0}{a_i}\right)^5 n_i e_i, \tag{37}$$

$$\frac{da_i^0}{dt} = \text{sign}(\omega_0 - n_i)3\frac{k_2^0 m_i}{Q_0^i m_0}\left(\frac{R_0}{a_i}\right)^5 n_i a_i, \tag{38}$$

where all parameters are as defined in previous Section. The derivation of these equations can be found in Souchay et al. (2013)'s Section 5.3.2 and requires the following assumptions: the orbit to be equatorial, prograde and circular, the time lag to be constant and independent of the tidal frequency (i.e. the constant time lag model is used), the moment of inertia of the central body to be constant, the spin vector of the central body to be aligned with its polar axis and the mass of the central body to be much larger than the mass of the satellite. This further highlights the flexibility of the coupled model, which does not rely on any of these assumptions. Note that for Eq. 37 the circularity assumption is dropped.

For the tides raised by a satellite in spin-orbit resonance on itself, the evolution of a_i and e_i are respectively given as (e.g., Lainey et al. (2009), Lari (2018)):

$$\frac{da_i^i}{dt} = -21\frac{k_2^i m_0}{Q_i^0 m_i}\left(\frac{R_i}{a_i}\right)^5 n_i a_i e_i^2, \tag{39}$$

$$\frac{de_i^i}{dt} = -\frac{21}{2}\frac{k_2^i m_0}{Q_i^0 m_i}\left(\frac{R_i}{a_i}\right)^5 n_i e_i. \tag{40}$$

It is useful to note that another expression for the rate of change of a_i exists in literature (e.g., Souchay et al. (2013), Boué (2019)):

$$\frac{da_i^i}{dt} = -57\frac{k_2^i m_0}{Q_i^0 m_i}\left(\frac{R_i}{a_i}\right)^5 n_i a_i e_i^2, \tag{41}$$

Where Eq. 41 and Eq. 39 differ by a factor 57/21. As explained by Fayolle (2025), this difference follows from the fact that angular momentum over one orbit is not conserved as the averaged tidal torque over one orbit is not exactly equal to zero. This non-zero tidal torque can be compensated for by a small shift in the pointing direction of the long axis of the satellite (e.g., Yoder (1981), Souchay et al. (2013)). This corresponds to a non-zero $S^i_{2,2}(t)$ coefficient, which would affect the orbit of the satellite similar to tidal dissipation.

In other words, following Fayolle (2025), Eq. 41 accurately models the effect of the satellite tides on the evolution of the semi-major axis. However, the effective semi-major axis evolution follows from the combined effect of tidal dissipation and a non-zero $S^i_{2,2}(t)$ coefficient, which cancels the non-zero tidal torque and leads to Eq. 39. This once more highlights the sensitivity of the used models to the rotation rate of the satellite and also again shows the advantage of the coupled model, from which this effect should follow automatically. To conclude, Eq. 39 and Eq. 40 accurately model the evolution of the satellite's semi-major axis and eccentricity due to its own tides and will be used in this work to compare the results from the coupled model. The coupled model can, on the other hand, also provide insight on which of the two equations provides a more accurate description of the effective orbital migration of a satellite.

Since a_i and e_i are governed by the orbital E_{orb} and rotational energy E_{rot}, their evolution is governed by the amount of energy dissipated (assuming that energy dissipation is completely caused by tidal effects) (e.g., Correia et al. 2014):

$$\dot{E} = -(\dot{E}_{rot} + \dot{E}_{orb}) \approx -\frac{\Delta E_{rot} + \Delta E_{orb}}{\Delta t} = \frac{\int_{t_0}^{t_f} \Big(\boldsymbol{F} \cdot \boldsymbol{v} - \boldsymbol{\omega} \cdot (\boldsymbol{r} \times \boldsymbol{F}) \Big) \mathrm{d}t}{\Delta t}, \quad (42)$$

with ΔE_{rot} and ΔE_{orb} the rotational and orbital energy dissipated over the period Δt, $\boldsymbol{F}$ the full force exerted by the perturber on the perturbed body (see Eq. 3), and t_0 and t_f the initial and final integration times. This equation can be used as validation to ensure that the system dissipates the expected amount of energy.

B. Gravity field coefficients

Next to the evolution of the orbital parameters, it will also be interesting to see how the gravity field coefficients of a body, calculated using Eq. 36, evolve due to the sudden stresses of the introduced bodies. Furthermore, it will be interesting to see how $S^i_{2,2}(t)$ evolves, especially given the discussion in the previous subsection. Currently, state-of-the-art approximations for the coefficients use a complex Love number to account for tidal lag, assuming a constant phase lag. They are given by (e.g., Petit et al. 2010):

$$J^i_2 = \left(\frac{\omega_i^2 R_i^3}{3\mu_i} + \frac{1}{2}\frac{m_i}{m_0}\left(\frac{R_i}{|\boldsymbol{r}_{i0}|}\right)^3 \right) \mathrm{Re}(k^i_2), \quad (43)$$

$$C^i_{2,2} = \frac{1}{4}\frac{m_i}{m_0}\left(\frac{R_i}{|\boldsymbol{r}_{i0}|}\right)^3 \times \times \Big(\mathrm{Re}(k^i_2)\cos 2\gamma_0 - \mathrm{Im}(k^i_2)\sin 2\gamma_0 \Big), \quad (44)$$

$$S^i_{2,2} = -\frac{1}{4}\frac{m_i}{m_0}\left(\frac{R_i}{|\boldsymbol{r}_{i0}|}\right)^3 \times \times \Big(\mathrm{Re}(k^i_2)\sin 2\gamma_0 + \mathrm{Im}(k^i_2)\cos 2\gamma_0 \Big). \quad (45)$$

Here $\mathrm{Re}(k^i_2)$ and $\mathrm{Im}(k^i_2)$ denote the real and imaginary part of k^i_2, accounting for the 'amplitude' and phase lag of the tidal bulge respectively. The following relations hold assuming a small phase lag δ:

$$k^i_2 = |k^i_2| \exp(-i \cdot 2\delta_i) = \mathrm{Re}(k^i_2) + i\mathrm{Im}(k^i_2), \quad (46)$$

$$\mathrm{Re}(k^i_2) = |k^i_2| \cos 2\delta_i \approx |k^i_2|, \quad (47)$$

$$\mathrm{Im}(k^i_2) = -|k^i_2| \sin 2\delta_i = -\frac{|k^i_2|}{Q^0_i}. \quad (48)$$

Here, the real part of the Love number is assumed equal to the literature value of the Love number.

Since the tidal coefficients completely dictate the gravitational shape of the body through the induced gravitational potential, they can be used to calculate geometric lag angle δ_i by the following relations:

$$\nu_i = \frac{1}{2}\arctan 2\left(\frac{S^i_{2,2}}{C^i_{2,2}}\right), \quad (49)$$

$$\gamma_i = (\mathrm{sign}(\hat{e}_A \cdot (\hat{r_{i0}} \times \hat{e}_C))) \cdot \arccos(\hat{e}_A \cdot \hat{r}) \mod 2\pi, \quad (50)$$

$$\delta_i = (\nu_i - \gamma_i) \mod \pi. \quad (51)$$

The first angle, ν_i, is the angle between the tidal bulge and the body-fixed I-axis.

The time lag Δt is assumed constant in current models, but the coupled model can also capture variations in Δt:

$$\Delta t_i = \frac{\delta_i |\boldsymbol{r}_{i0}|}{|\boldsymbol{\omega}_i \times \boldsymbol{r}_{i0} - \boldsymbol{v}_i|}. \tag{52}$$

The tidal time lag retrieved from Eq. 52 can be compared to the constant time lag retrieved from Eq. 14. Note that since it has been assumed constant, it will fail to capture intricate details that the coupled model might be able to desccribe, next to being a worse approximation. The constant time lag model is, however, a better approximation than the constant lag angle model, because the latter does not hold for eccentric orbits (e.g., Efroimsky et al. 2013).

C. Librations

Averaged over time, the Moon's rotation rate, as that of many other large (natural) satellites, is synchronous with its mean motion, implying that its rotational and orbital period are equal (e.g., Henrard 2006), also known as a spin-orbit resonance. A perfectly circular orbit would imply that the body-fixed longitude of the central body as seen from the satellite is always zero. However, perturbations prevent the satellite's long axis (i.e., principal axis of minimum inertia) from pointing towards the central body at all times; superimposed on the *once-per-orbit* rotation around its spin axis, these effects cause the satellite to oscillate and wobble around its three axes (e.g., Hoolst et al. 2020). These deviations are known as librations. In this work, only longitudinal librations will be considered, as latitudinal librations are small for most natural satellites and their effect on its orbit is limited.

Longitudinal librations can be decomposed into *optical* and *physical* librations. The former is caused due to the geometry of the orbit, while the latter can even occur for circular orbits as it is a result of the internal properties of a satellite (e.g., Hurford et al. 2009), which is of interest in this work. Important is to note that wrong initial conditions can add to the variations of the rotation angle, which can then yield unphysical librations (see Section 2.4 and 2.5). Efroimsky (2018) states that physical librations also contribute towards tidal dissipation, because they affect tidal torques through the dependency of the rotation rate on librations (see Fayolle (2025) for a more extensive discussion). Efroimsky (2018) gives a relation between this additional dissipation due to librations with respect to the tidally induced powers as if there were no librations. The coupled model should automatically incorporate this, so it will be interesting to see whether this effect can be correctly predicted by the relation proposed by Efroimsky (2018), assuming a once-per-orbit longitudinal libration:

$$\frac{\langle P \rangle_{\text{tide}}^{(\text{lib})}}{\langle P \rangle_{\text{tide}}^{(\text{main})}} = 1 - \frac{4\theta_\tau}{7e_i} + \frac{\theta_\tau^2 + \theta_f^2}{7e_i^2}, \tag{53}$$

where θ_f is the amplitude of the free librations, which should be approximately equal to 0 for most Solar System bodies and the (lib) and (tide) superscripts indicate the tidal power including librations and the tidal power as if there were no librations.

IV. RESULTS

This section will discuss the results gathered in this work. The results for the Earth and the Moon will be discussed separately. Secular rates of evolution for a and e will be analyzed and compared against theory. From the coupled model, some tidal parameters will be computed and compared against theory, and the behaviour of the system will be analyzed for varying tidal parameters. Furthermore, the evolution, and any discrepancy in, the gravity field coefficients will be analyzed. The perturbed and unperturbed cases will be compared to each other.

A. Earth

As a first step to propagate the Earth's dynamics (i.e. the tides raised by the Moon on the Earth), a damped initial state must be found. Unlike the case of propagating a satellite's dynamics, a central body such as the Earth will not experience librations. As a result, rotational normal modes are practically non-existent and need not be damped. Hence, the rotational state can be retrieved from existing data (see Appendix A for more information regarding the initial states used), while the translational state is retrieved from the damping performed from the Moon's initial state (see Appendix D for the damping algorithm). Subsequently, the uncoupled and coupled model have been propagated for 5000 days (around 13 years and 8 months). Table I denotes the exact propagations performed for the results gathered in this section.

1. *State propagation*

To get a first impression of how the uncoupled and coupled model differ, Fig. 4a displays the norm of the position difference between the uncoupled and coupled model, growing up to ∼20 m over the propagation period with a quadratic trend. The tidal parameters used in the uncoupled model have been derived from the tidal parameters of the coupled model using Eq. 25-27, ensuring consistency in the used parameters.

Fig. 4b shows the position-components, projected in the *RSW* frame. For a given trajectory, a point can be defined by the right-handed triad $\{\hat{\boldsymbol{r}}, \hat{\boldsymbol{s}}, \hat{\boldsymbol{w}}\}$, with the unit vector $\hat{\boldsymbol{r}}$ along the position vector, $\hat{\boldsymbol{w}}$ along the angular momentum vector and $\hat{\boldsymbol{s}}$ completing the reference frame. It is apparent that the along-track direction shows a secular quadratic trend (the coupled trajectory's along-track position gets ahead of the uncoupled one) growing

Table I: Specific propagation settings used and propagations performed for the results gathered in this section.

	Propagation period	Equations of motion	Integrator settings
Coupled model	5000 days	Eq. 34, 35, 15	DOP583, 160 minute step size
Uncoupled model	5000 days	Eq. 34-36	DOP583, 160 minute step size

up to ∼20 m superimposed by oscillations of increasing amplitude. Although there are oscillations in the order of centimeters present for the radial and perpendicular components, their mean values remain the same between the two models. The frequency decomposition of the differences is displayed in Fig. 4c. They oscillate at the frequency of n - with some smaller peaks at its integer multiples - and thus the two models differ at this frequency, resulting in the oscillations with increasing amplitude in the time domain. This is expected, as the introduction of varying gravity field coefficients (see the next subsection) results in additional oscillations in the position through their influence on the dynamics in Eq. 34-36. The secular trend is in line with the expectations laid out in the introduction and Section 2.4; the inconsistent modelling of rotation and tides in the decoupled model results in a secular along-track drift, and is indeed shown in Fig. 4b.

Fig. 4d shows that there is a secular trend in the difference of the semi-major axis superimposed by oscillations of constant amplitude growing up to $\sim$ 1 cm over the propagation period, meaning that both models dissipate a different amount of orbital energy. Note that this difference is small compared to the evolution rates of the semi-major axis according to both models, see Table V. The oscillations occur at the orbital frequency of n suggesting that they are possibly a result of the periodic variation of the gravity field coefficients. The uncoupled model assumes constant gravity field coefficients and uses a tidal force expression, while the coupled model captures time-variations in these coefficients; they result in changing dynamics that contribute towards a change in position.

2. *Gravity field coefficients and tidal parameters*

The frequency content of the converged gravity field coefficients of the damped propagation for the coupled model is displayed in Fig. 5. All three coefficients have converged around a certain equilibrium value superimposed by oscillations of constant amplitude at the orbital frequency of the mean motion n for J_2, and the period of the tidal forcing for C_{22} and S_{22}. The coefficients presented here are as determined in Eq. 30, i.e. the variation in gravity field coefficients from their initial *static* value upon introduction of tidal forcings. J_2 converges to a non-zero value, while C_{22} and S_{22} oscillate around zero. As a result, the comparison with the theoretical approximation of the coefficients (Eq. 43-45) is not really relevant for J_2 but can be done for C_{22} and S_{22}, shown in the Table II. The values displayed are the mean values of the coefficients over time over an integer number of orbits to ensure consistency. Fig. 6 shows the gravity field coefficients as a function of the mean anomaly of the Moon's orbit. As expected, J_2 has a once-per-orbit oscillation, while the behaviour for C_{22} and S_{22} is distinctly different from J_2, since they oscillate at the frequency of the tidal forcing period. Furthermore, C_{22} and S_{22} are close to being in-phase, having mean values over time of $2.574 \cdot 10^{-11}$ and $2.752 \cdot 10^{-11}$ respectively at $M = 0$ rad. The time variations in C_{22} and S_{22} coefficients are also in good accordance with the results from Eq. 44 and 45; the mean amplitude of the time variations for the gravity field coefficients is displayed in Table III. The behaviour of C_{22} and S_{22} is thus in good accordance between the coupled model and approximations from Eq. 44 and 45. For J_2, the time variations are larger for the coupled model, possibly due to the inclusion of the centrifugal potential, whereas Eq. 43 does not include the centrifugal potential contribution towards J_2.

Table II: Mean values of the gravity field coefficients for the coupled model and the approximations (Eq. 44, 45) over the specified propagation period.

	$C_{2,0}$	$C_{2,2}$	$S_{2,2}$
Approximations	N/A	$-3.324 \cdot 10^{-14}$	$2.302 \cdot 10^{-14}$
Coupled model	$-1.075 \cdot 10^{-3}$	$-3.927 \cdot 10^{-14}$	$1.858 \cdot 10^{-14}$

Table III: Mean amplitudes of the gravity field coefficients for the coupled model and the approximations (Eq. 43-45) over the specified propagation period.

	$C_{2,0}$	$C_{2,2}$	$S_{2,2}$
Approximations	$1.66 \cdot 10^{-9}$	$5.285 \cdot 10^{-9}$	$5.285 \cdot 10^{-9}$
Coupled model	$4.701 \cdot 10^{-9}$	$5.273 \cdot 10^{-9}$	$5.269 \cdot 10^{-9}$

As introduced in Section 2.3, the viscoelastic nature of bodies results in a measurable tidal time lag (and lag angle), providing valuable information about the rate of energy dissipation in a body. For the coupled model, the tidal time lag is determined through Eq. 52 and compared to Eq. 14. The resulting mean tidal time lag and lag angle for both are given in Table IV, while the time-dependent behaviour of the time lag and lag angle is seen in Fig. 7. The mean values coincide well between Eq. 52 and Eq. 14, with the difference in the tidal time lag being less than 0.5%. Note that, as expected, the theoretical approximation shows no time-dependency, while the coupled model captures time-variations in the tidal time lag. The variations in the tidal time lag are in line with the variations of the gravity field coefficients, with both having their largest oscillations occur at the orbital frequency of the mean motion.

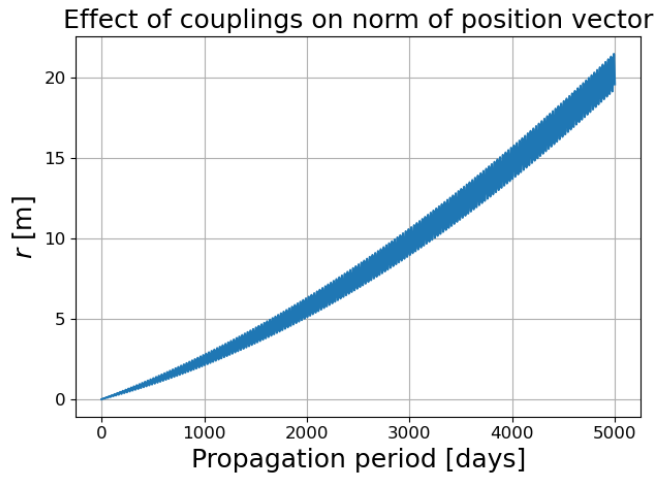

(a) Norm of the difference in the propagated position vector between the uncoupled and coupled model.

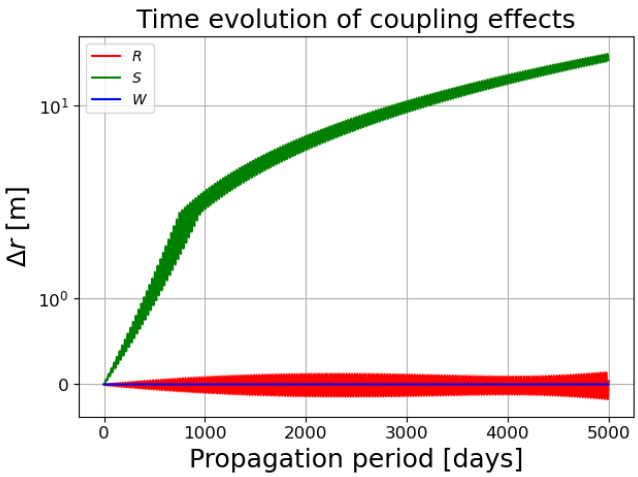

(b) Difference in the propagated position vector between the uncoupled and coupled model.

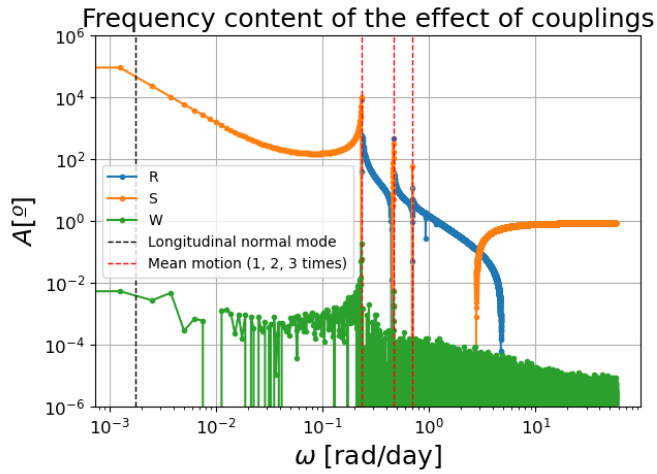

(c) Frequency decomposition of the position difference between the uncoupled and coupled model.

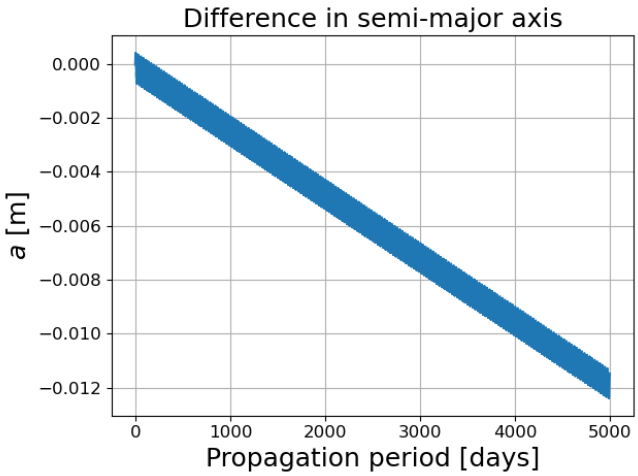

(d) Difference in semi-major axis between the uncoupled and coupled model.

Figure 4: Comparison of the uncoupled model and the coupled model over the specified propagation period in the following ways: norm of the difference in position (top left), components (top right), frequency spectrum of the component (bottom left) and the difference in semi-major axis (bottom right).

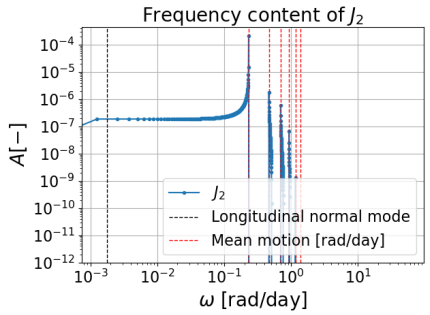

(a) Frequency content of J_2.

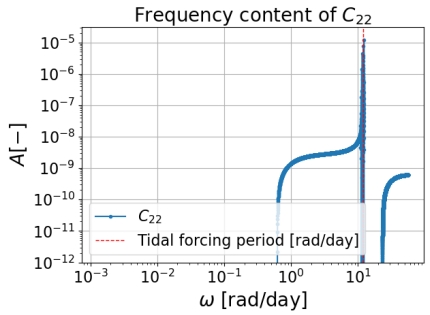

(b) Frequency content of C_{22}.

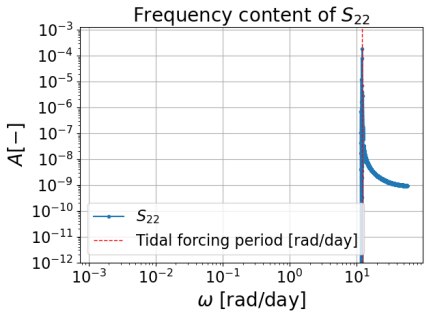

(c) Frequency content of S_{22}.

Figure 5: Frequency spectra of the gravity field coefficients of the Earth. Note the distinct difference in frequency of the peaks between J_2, and C_{22} and S_{22}.

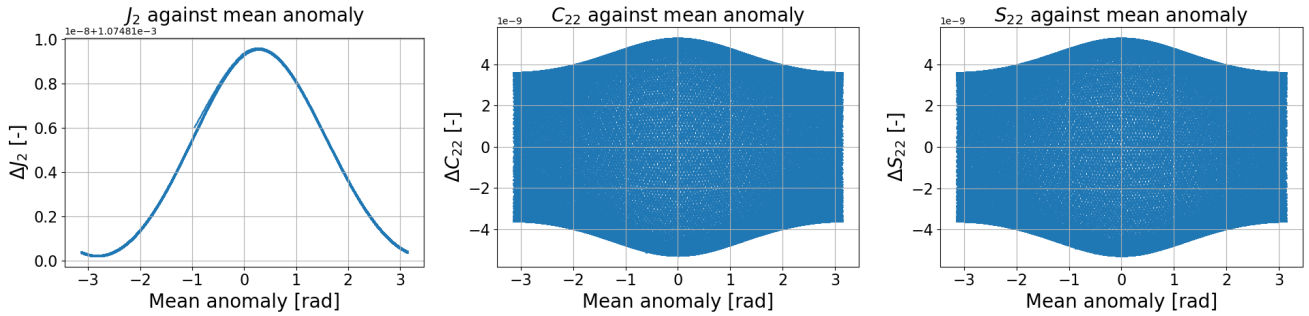

(a) J_2 over the mean anomaly. (b) C_{22} over the mean anomaly. (c) S_{22} over the mean anomaly.

Figure 6: The gravity field coefficients of the Earth over the mean anomaly of the orbit. Notice that the difference in J_2 is out of phase with respect to the mean anomaly, while C_{22} and S_{22} are not.

Table IV: Mean values of δ and Δt for the coupled model and the theoretical approximations (Eq. 14).

	δ [deg]	Δt [s]
Coupled model	2.39	596.1
Theory	2.40	599.0

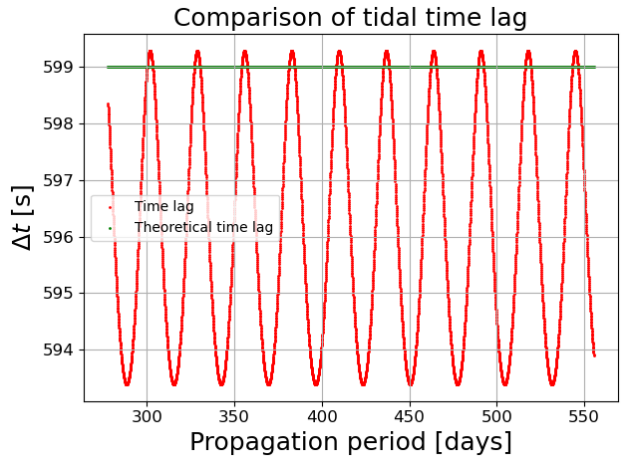

Figure 7: Tidal time lag from Eq. 14 and the coupled model. Note the explicit time-dependence that follows from the coupled model, which is not reproduced by Eq. 14. Part of the propagation is displayed for clarity.

3. *Semi-major axis and eccentricity evolution*

The semi-major axis and eccentricity evolution due to tides is compared by retrieving the values from the coupled model, the uncoupled model and the approximations in Eq. 37 and Eq. 38. For the coupled and uncoupled model, the rates of change of a and e are retrieved from the state history of both propagations using a linear fit. The results are gathered in Table V. The mean values are taken over time over an integer number of orbits to ensure consistency.

Table V: Mean values of $\frac{\mathrm{d}a}{\mathrm{d}t}$ and $\frac{\mathrm{d}e}{\mathrm{d}t}$ for the coupled model, uncoupled model and the theoretical approximations (Eq. 37 and Eq. 38).

	$\frac{\mathrm{d}a}{\mathrm{d}t}$ [nm/s]	$\frac{\mathrm{d}e}{\mathrm{d}t}$ [-/y]
Uncoupled model	1.311	$1.805 \cdot 10^{-11}$
Coupled model	1.284	$-5.738 \cdot 10^{-12}$
Eq. 37, 38	1.248	$1.545 \cdot 10^{-11}$

The results show that the evolution of the semi-major axis is generally in good accordance between the theory, uncoupled model and coupled model. The difference may (partly) stem from the fact that the theoretical approximation assumes a circular orbit, while the Moon's orbit is relatively eccentric. The difference between the coupled model and the approximations in Eq. 37 and 38 is less than 3%. It is also interesting to note that the coupled model seems in better agreement with these equations than the uncoupled model. The difference between the coupled model and uncoupled model is in accordance with the difference seen in Fig. 5d, and may be attributed to the effect of couplings on the orbit.

Interestingly, however, the rate of change for eccentricity does not show similar accordance. The uncoupled model and theoretical approximation are relatively close, differing by 16.8%. However, for a shorter propagation time of 500 days, the difference between the two is much larger; indicating that this difference is coincidentally small. Similarly, the coupled model's $\frac{\mathrm{d}e}{\mathrm{d}t}$ is also quite off. Both values are well above the integrator error, with the error being in the order of 10^{-11} m and 10^{-14} respectively for a and e over a propagation period of 500 days. It is thus likely that the signature of $\frac{\mathrm{d}e}{\mathrm{d}t}$ is too small to properly detect compared to the relatively large once-per-orbit variation of the eccentricity, especially because the uncoupled model also fails to produce the correct rate of change. The secular change in eccentricity is in the order of 10^{-11} [-/y], while the once-per-orbit variations are

in the order of 10^{-6}, 5 orders of magnitude larger. In other words, the signature is impossible to extract from the period trend.

4. *Varying relaxation times*

The results that have been gathered until now have used set constants for the tidal parameters of the Earth and Moon, which are collected in Appendix A. It is of interest to see whether the coupled model can robustly handle a large variation of tidal parameters, partly because tidal parameters are not well known for many planets and satellites in the solar system (This is one of the goals for JUICE: to constrain the dissipation in Jupiter at the frequency of the Galilean moons (e.g., Magnanini et al. 2024)). This furthermore gives insight into how tidal energy is dissipated as the relaxation times - the tidal parameters of the coupled model - vary. The classical tidal parameters, k_2 and Q, are related to them through Eq. 25-27. By varying τ_2, the ratio k_2/Q is varied, which results in a different phase lag and thus, presumably, a different rate of energy dissipation. A range of values are taken around the true τ_2, and subsequently $\frac{\mathrm{d}a}{\mathrm{d}t}$ and $\frac{\mathrm{d}e}{\mathrm{d}t}$ are determined for every propagation, after which they are plotted against the ratio k_2/Q in Fig. 8.

Fig. 8 shows similar results to the single run results in Table V, where the evolution of the semi-major axis is in good accordance with theory for a range of relaxation times, but the evolution of the eccentricity remains off for all tested values. For the case of $\tau_2/\tau_e = 0$, at which point there should be no dissipation, which is what is visible in Fig. 8a, the eccentricity has a non-zero rate of change in Fig. 8b. The system correctly dissipates the most orbital energy for the largest value of k_2/Q, as the phase lag is then maximal. However, it becomes clear that, for the tides raised by the Moon on the Earth, the method used to extract the evolution of the eccentricity fails to do so correctly. Note that Fig. 8b does show a trend as a function of k_2/Q, it is however not clear what exactly this trend can be attributed to, and why the values of the evolution of e differ for the same values of $k_2/Q \approx 0.025$.

5. *Tidal effect of third-body perturbations*

This section aims to quantify and investigate how the coupled model captures the influence of additional perturbations when investigating the effect of tides raised by the Earth on the Moon's orbit. For this system, now including the perturbations of the Sun and Jupiter, is propagated and damped once more. With the final damped initial state, a propagation of 5000 days is performed.

In order to 'isolate' the effect of tides raised by perturbations (i.e. the Sun and Jupiter) on the Earth, the equations of motion in Eq. 34-36 are propagated in two different ways. In both propagations the perturbations are included in the translational and rotational dynamics (i.e. Eq. 34 and 35). In the first propagation (PC1), the perturbations are also included in calculating the equilibrium gravity field coefficients as in Eq. 36. In the second propagation (PC2), the perturbations are included, but the contribution of the Moon towards the tides raised on the Earth is left out. The exact models used for these propagations are displayed in Table VI.

Table VI: Details of terms included in Eq. 36 used to isolate the influence of perturbations (i.e. the Sun and Jupiter) on the orbital evolution of the Earth-Moon system. *Both* models include the perturbations in the translational and rotational dynamics in Eq. 34 and 35

identifier	Moon	Jupiter	Sun
PC1	Yes	Yes	Yes
PC2	No	Yes	Yes

Then, taking the difference between these two propagations should give a good idea of what the effect of perturbations are on the tides raised on the Earth. The resulting difference in a between these two propagations is displayed in Fig. 9. Over the propagation period, the difference grows up to ∼7 m. Note that there is a small secular trend in the semi-major axis difference, superimposed by oscillations of ever-increasing amplitude. It is this secular change, which is approximately ∼1 m, that may be attributed to tidal effects from the perturbations, but cannot be concluded.

A caveat in using this method is that the same initial state is used for both propagations. However, for one of the two propagations, the initial state used is not perfectly damped, as the dynamics have changed slightly by leaving out the Moon's contribution in Eq. 31-33. Hence, the results may not truly isolate the effect of perturbations, but part of the effect seen may also be attributed to the model converging to a new damped state, resulting in changing dynamics and incorrectly attributing changes in the semi-major axis to tidal effects. If this is the case, this should be visible in Fig. 10. While it is not, this may be due to the relatively short propagation period not allowing all terms 'time' to show up on the frequency spectrum. The frequency decomposition of the tidal forcing of the two propagations displayed in Fig. 10. The frequency content of the tidal forcing of the two propagations is quite similar, with no apparent new peaks introduced. This may suggest that there are no larger periodic variations that should be taken into account, but the propagation period may be too short to conclude this. However, when moving to more complex systems, such as the Galileans moons, where the moons have a much larger influence on each other due to the Laplace resonance, it is a certainty that perturbations must be included in modelling the tides and that the coupled model is a suitable candidate to do so. It remains, however, a topic for further research on what the best way is to extract the secular evolution rates of

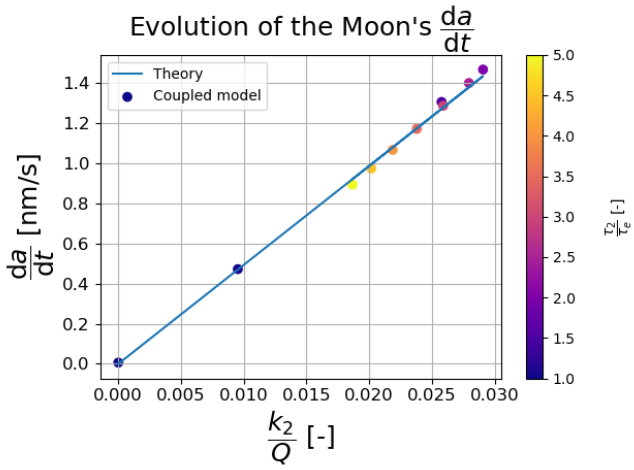

(a) $\frac{da}{dt}$ as a function of k_2/Q

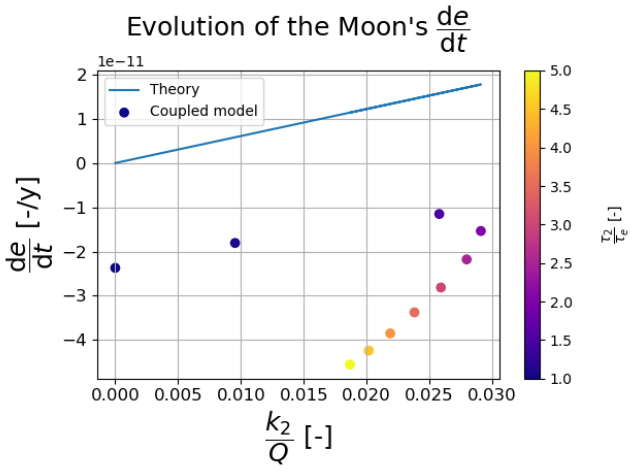

(b) $\frac{de}{dt}$ as a function of k_2/Q

Figure 8: The evolution of the orbital parameters as a function of k_2/Q. Note that the behaviour agrees well with the theoretical approximation for the semi-major axis evolution, but breaks down for the eccentricity evolution.

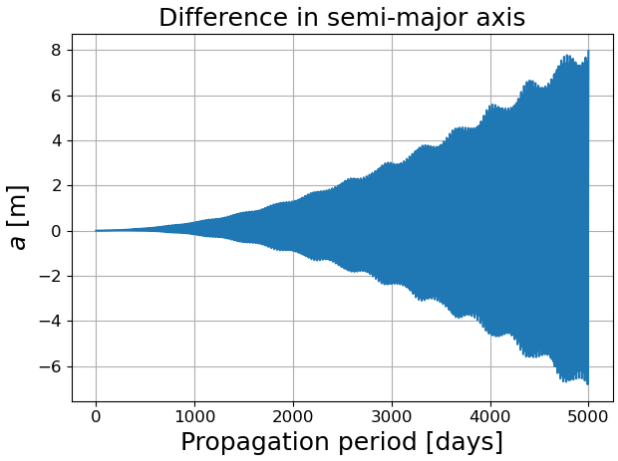

Figure 9: Difference in a between a propagation with and without the Moon's influence on the tides raised on the Earth.

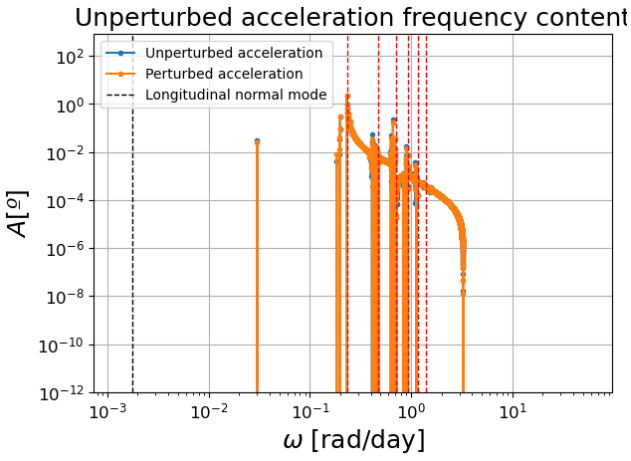

Figure 10: Frequency decomposition of the tidal forcing of the unperturbed and perturbed propagations respectively.

the semi-major axis and eccentricity from such results.

B. Moon

As a first step to propagate the Moon's dynamics (i.e. tides raised on the Moon by itself), a damped initial state has been found using the damping algorithm described in Appendix D. Since the satellite's internal properties result in significant rotational normal modes, it is imperative they are sufficiently damped, and if not completely possible, taken into account during the discussion of the results. Appendix D quantifies how well the rotational normal modes have been damped for the investigated case. Subsequently, the uncoupled and coupled model are propagated for 5000 days (approximately 13 years and 8 months) each with the same initial state. The specifics of the propagations performed are displayed in Table VII.

Before discussing results, it is important to ensure that the results from the coupled model is in the same reference frame as the equations it will be compared to assume in their derivations. Specifically, all results are rotated to a body-fixed frame with the Moon's x-axis pointing towards the Earth at $M = 0$, and the z-axis along the angular momentum vector. The y-axis completes the right handed triad. See Appendix C for the verification of this rotation.

Table VII: Specific propagation settings used and propagations performed for the results gathered in this section.

	Propagation period	Equations of motion	Integrator settings
Coupled model	5000 days	Eq. 34, 35, 16, 17	DOP583, 160 minute step size
Uncoupled model	5000 days	Eq. 34-36	DOP583, 160 minute step size

1. State propagation

Figure 11a shows that the frequency composition of differences between the uncoupled and coupled model for the tides raised by the Moon on itself also occur at the orbital frequency - and integer multiples - of the mean motion n, in line with the results of the previous section.

However, the difference in semi-major axis shows that, on top of the secular trend that is expected based on theory and the results in the previous section, there is a larger oscillatory trend as well; these oscillations occur at the frequency of the rotational normal modes. For satellites, rotational normal modes arise quickly even if the dynamics or initial state is *slightly* modified. As a result, the damped initial state used in the coupled model is *not* a damped initial state for the uncoupled model, giving rise to the rotational normal modes displayed. Furthermore, note that there is a secular change in the difference in semi-major axis between the two models, which grows up to 10 cm. This difference is about 10 times larger than the difference in semi-major axis between the two models for the tides raised by the Earth on the Moon, displayed in Fig. 4. This might indicate, as discussed in Chapter 2, that the uncoupled model has more difficulty modelling natural satellites than it does for central bodies. Furthermore, it is important to place these numbers in context with respect to the evolution rate of the semi-major axis, displayed in Table X, which shows that that is much smaller, making the difference in semi-major axis between the uncoupled and coupled model even more significant.

2. Tidal parameters

The frequency content of the converged tidal coefficients of the damped propagation for the coupled model is displayed in Fig. 12. Note that again all three coefficients have converged to a certain equilibrium value superimposed by oscillations with a constant amplitude at the orbital frequency of the mean motion n and its integer multiples. Different than for the Earth's tides raised by the Moon, J_2 and C_{22} converge to non-zero values, while S_{22} seems to oscillate around zero. Thus the comparison to the approximations in Eq. 43-45 is only interesting for S_{22}. The relevant values are displayed in Table VIII. Fig. 13 shows the gravity coefficients as a function of the Mean anomaly. Note the large amplitude of the variation in S_{22} compared to its mean value. The time variations are in very good accordance with the results from Eq. 43-45, with the mean amplitudes of the time variations displayed in Table IX.

Remarkably, the difference between the mean value over time over integer orbits of S_{22} from Eq. 45 and the coupled model is significant, with Eq. 45 yielding a S_{22} equal to $1.972 \cdot 10^{-08}$ and S_{22} from the coupled model being $-3.778 \cdot 10^{-13}$, effectively equal to 0. Circling back to the discussion in Section 3, this indicates that during the propagation of the Moon's dynamics, a very small shift in the pointing direction of the long axis of the satellite occurs, but on average appears to be much smaller than Eq. 45 predicts, and is practically equal to zero. Since this shift has an influence on the amount of energy dissipated due to tides, it becomes interesting whether the coupled model can still correctly predict the semi-major axis and eccentricity evolution.

Table VIII: Mean values of the gravity field coefficients for the coupled model and the approximations (Eq. 45) over the specified propagation period.

	$C_{2,0}$	$C_{2,2}$	$S_{2,2}$
Approximations	N/A	N/A	$1.972 \cdot 10^{-08}$
Coupled model	$9.238 \cdot 10^{-06}$	$2.720 \cdot 10^{-06}$	$-3.778 \cdot 10^{-13}$

Table IX: Mean amplitudes of the gravity field coefficients for the coupled model and the approximations (Eq. 43-45) over the specified propagation period.

	$C_{2,0}$	$C_{2,2}$	$S_{2,2}$
Approximations	$5.274 \cdot 10^{-7}$	$2.639 \cdot 10^{-7}$	$3.512 \cdot 10^{-7}$
Coupled model	$5.274 \cdot 10^{-7}$	$2.639 \cdot 10^{-7}$	$3.512 \cdot 10^{-7}$

3. Semi-major axis and eccentricity evolution

Similar to when analyzing the secular changes in a and e due to the tides raised by the Moon on the Earth, the tides raised on the Moon by itself also give rise to secular rates of change in a and e. The values are gathered in Table X.

Table X: Mean values of $\frac{\mathrm{d}a}{\mathrm{d}t}$ and $\frac{\mathrm{d}e}{\mathrm{d}t}$ for the coupled model, uncoupled model and the theoretical approximations (Eq. 39 and Eq. 40).

	$\frac{\mathrm{d}a}{\mathrm{d}t}$ [nm/s]	$\frac{\mathrm{d}e}{\mathrm{d}t}$ [-/y]
Coupled model	-0.149	$-9.330 \cdot 10^{-11}$
Theory	-0.142	$-9.294 \cdot 10^{-11}$

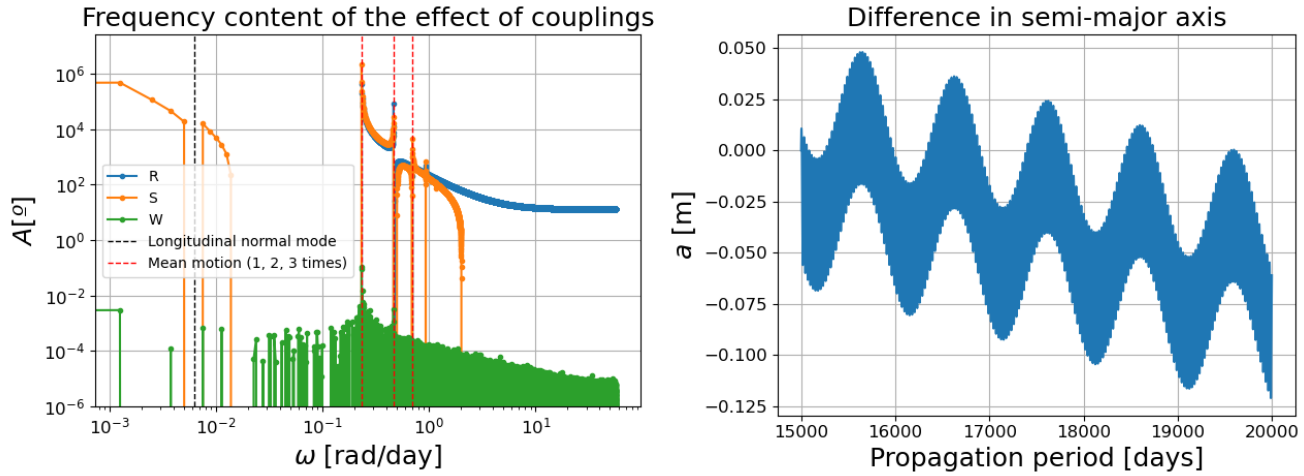

(a) Frequency decomposition of the position difference between the uncoupled and coupled model.

(b) Difference in semi-major axis between the uncoupled and coupled model.

Figure 11: Comparison of the uncoupled model and the coupled model in the following ways: frequency spectrum of the difference in position components (left) and the difference in semi-major axis (right).

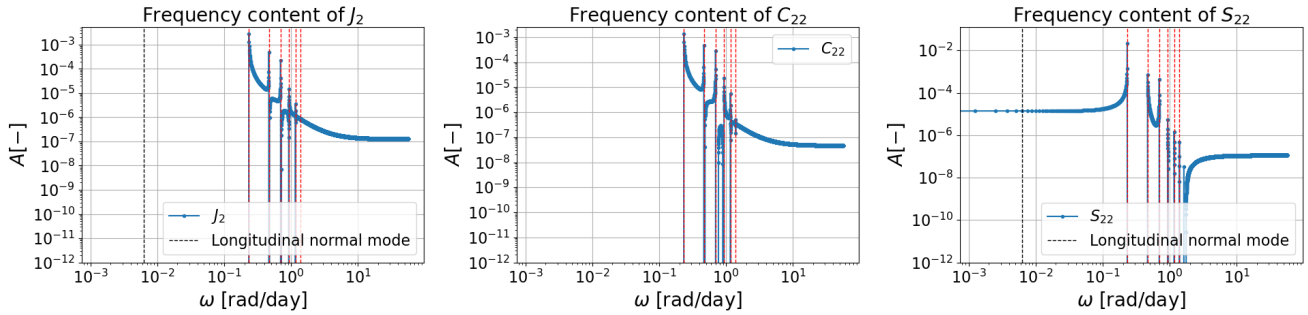

(a) Frequency content of J_2.

(b) Frequency content of C_{22}.

(c) Frequency content of S_{22}.

Figure 12: Frequency spectra of the gravity field coefficients of the Moon. The red dashed lines are the mean motion n and integer multiples in rad/day.

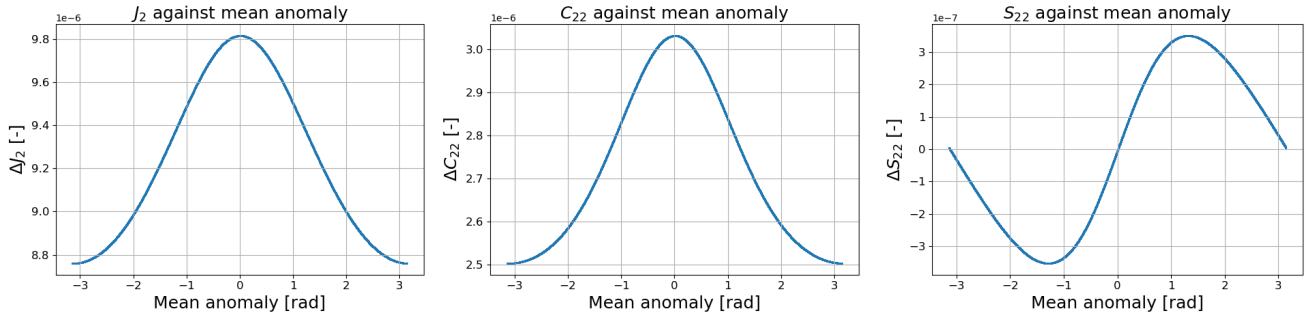

(a) J_2 over the mean anomaly.

(b) C_{22} over the mean anomaly.

(c) S_{22} over the mean anomaly.

Figure 13: The gravity field coefficients of the Earth over the mean anomaly of the orbit. Notice that the difference in J_2 is out of phase with respect to the mean anomaly, while C_{22} and S_{22} are not.

The evolution of the eccentricity agrees very well between the coupled model and Eq. 40, whereas it did not for the case of tides raised on the Earth, despite both rates of change being similar in magnitude. The time variations in the eccentricity due to the Moon's gravity field coefficients is two orders of magnitude smaller than due to the gravity coefficients of the Earth, and hence the signature is relatively larger in this case, making it easier to detect in this situation. Hence, this adds confidence in that the coupled model functions correctly in both cases, but the signature was simply too small to detect for the tides raised on the Earth by the Moon.

Despite the large disparity between S_{22} from Eq. 45 and the coupled model in Table VIII, the coupled model produces the correct values for $\frac{\mathrm{d}a}{\mathrm{d}t}$ and $\frac{\mathrm{d}e}{\mathrm{d}t}$ compared to Eq. 39 and Eq. 40, demonstrating that the model still dissipates the right amount of energy due to tides. The coupled model hence confirms the discussion in Section 3, stating that Eq. 39 and *not* Eq. 41 models the effective semi-major axis evolution. Furthermore, the additional dissipation due to physical librations as given in Eq. 53 is included when using Eq. 39. The coupled model thus correctly and automatically includes this effect, making it even more attractive to use.

In order to verify that the correct amount of orbital energy is dissipated, Eq. 42 is used to calculate the rate of change of orbital energy dissipated due to tides and is compared to a linear fit of the orbital energy calculated from the semi-major axis output by the coupled model. From the linear fit, the rate of change of the orbital energy is $\dot{E}_{orb}$ = -14.89 GJ/s. The results from using Eq. 42 are gathered in Table XI. Two separate cases are analyzed. First, the calculation is performed with the full state history of $C_{22}(t)$ and $S_{22}(t)$, i.e. the periodic variations are taken into account. Second, the same calculation is performed with the mean values over time over integer orbits of $C_{22}(t)$ and $S_{22}(t)$, $\bar{C}_{22}$ and $\bar{S}_{22}$, denoted in Table VIII. For both cases, the separate contributions of $C_{22}(t)$ and $S_{22}(t)$ towards the tidal dissipation are also denoted.

Table XI: $\dot{E}_{orb}$ in GJ/s calculated using Eq. 42 for various cases.

	$C_{22}(t)$ and $S_{22}(t)$	C_{22} and S_{22}
Total effect	-14.44	-0.0006
C_{22} contribution	-5.36	0.00004
S_{22} contribution	-9.08	-0.00064
Coupled model	-14.89	

Two interesting conclusions can be drawn from these results. First of all, $C_{22}(t)$'s influence on the tides has a significant contribution towards $\dot{E}_{orb}$, and thus the change in E_{orb} (and thus a) is not completely caused by S_{22}, which is a common assumption when working with the *mean* values of these gravity field coefficients (e.g., Fayolle 2025). Apparently, this does not hold for time-variable gravity field coefficients. Secondly, and maybe even more remarkable, using $\bar{C}_{22}$ and $\bar{S}_{22}$ as input in Eq. 42 results in almost no tidal dissipation compared to the first case, with $\dot{E}_{orb}$ being almost 5 orders of magnitude smaller than $\dot{E}_{orb}$ from the first case. This result suggests that it is the time variation in $C_{22}(t)$ and $S_{22}(t)$ that is solely responsible for this behaviour, and that this behaviour cannot be reproduced by working with their respective mean values.

4. *Varying relaxation times*

Similar to when investigating the tides raised by the Moon on the Earth, the tidal parameters can again be varied for the tides raised by the Moon on itself. Again, a broad range of values are taken around the true τ_2, and subsequently $\frac{\mathrm{d}a}{\mathrm{d}t}$ and $\frac{\mathrm{d}e}{\mathrm{d}t}$ are determined for every propagation, after which they are plotted against the ratio k_2/Q in Fig. 14.

From the figure it follows that the rates of change obtained from the coupled model are in line with the theory for all investigated values of the relaxation times. This confirms that the coupled model correctly and robustly dissipates the correct energy due to tides raised on the Moon by itself.

Similar to how $\frac{\mathrm{d}a}{\mathrm{d}t}$ changes as a function of k_2/Q, it also becomes interesting to see how $\bar{S}_{22}$ behaves as a function of k_2/Q. The results are gathered in Fig. 15. Interestingly, there seems to be no significant relation between the Moon's $\bar{S}_{22}$ and k_2/Q. Rather, the values of $\bar{S}_{22}$ actually have decreased by at least an order of magnitude and, within the accuracy of the averaging computation, is likely statistically consistent with 0. This might hint at the following hypothesis: $\bar{S}_{22}$ is actually equal to zero over one orbit regardless of the value of k_2/Q, and it is the time-variation and magnitude of the periodic oscillations in S_{22} (and C_{22}) that change and give rise to tidal dissipation. Further study is required in this direction.

V. CONCLUSION

This paper has investigated how couplings between translational, rotational and tidal dynamics influences the orbital migration of natural satellites for a given initial state. The results were compared to a simplified, 'uncoupled' model, where the translational and rotational dynamics are propagated concurrently, but the influence of tides on the dynamics is modelled using a tidal force. The difference between these two trajectories was largest in the along track direction, growing up to 20 m after 13 years and 8 months. There was no secular evolution present in the radial and tangential direction, and all three components experienced oscillations at the orbital frequency of the mean motion.

The results of the orbital evolution of the semi-major

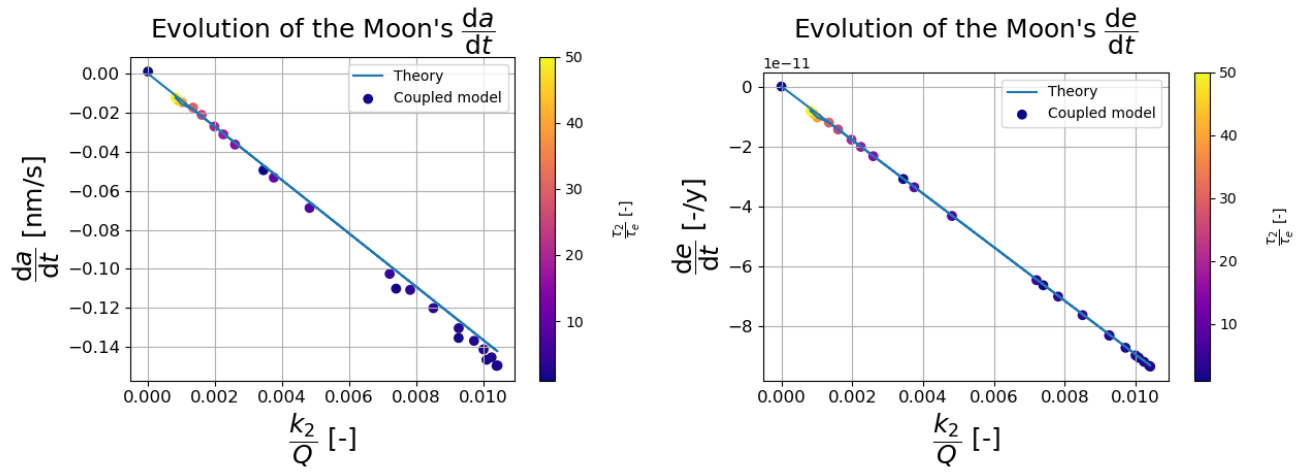

(a) $\frac{\mathrm{d}a}{\mathrm{d}t}$ as a function of k_2/Q

(b) $\frac{\mathrm{d}e}{\mathrm{d}t}$ as a function of k_2/Q

Figure 14: The evolution of the orbital parameters as a function of k_2/Q. The behaviour agrees well for the orbital evolution of both parameters for all values investigated.

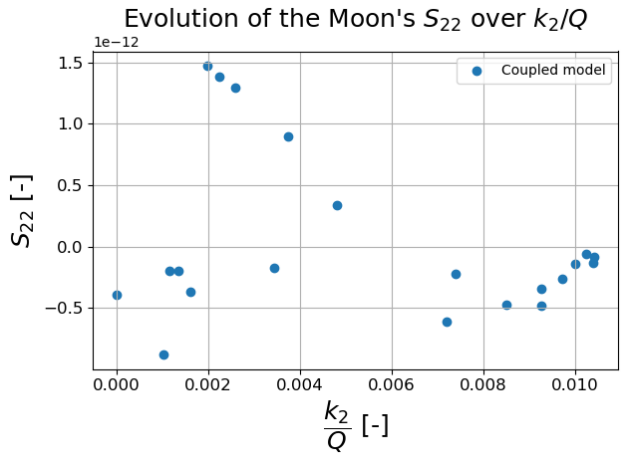

Figure 15: $\bar{S}_{22}$ in the corrected reference frame, where $\gamma_0(M=0)=0$. Note that now there seems to be no relation with k_2/Q.

axis for the tides raised on the Earth by the Moon and the tides raised on the Moon by itself match well between the uncoupled model, coupled model and Eq. 37 and Eq. 39; the evolution of the eccentricity matches for the tides raised on the Moon by itself only with Eq. 40. Due to the large once-per-orbit variation of the eccentricity, the signature of $\frac{\mathrm{d}e}{\mathrm{d}t}$ is too small to detect for the tides raised on the Earth. For a wide range of tidal input parameters τ_2 and τ_e (compared to the classical tidal parameters k_2 and Q) this behaviour is reproduced, showing the robustness of the coupled model and demonstrating its validity. Furthermore, while modelling perturbations showed to be of limited importance in this work, it is almost a certainty that they will be much more relevant in more complex systems such as the Galilean moons, and that the coupled model will be a good candidate to do so.

The coupled model manifests the tidal dissipation differently from simplified, uncoupled approaches and approximations in literature. The Moon's mean $S_{22}(t)$ over time over an integer number of orbits from the coupled model is equal to zero, while literature approximations result in a mean $S_{22}(t)$ of $1.972 \cdot 10^{-8}$. The orbital energy dissipated by the coupled model matches the theoretical orbital energy dissipation rate as in Eq. 42, with the values being -14.89 GJ/s and -14.44 GJ/s respectively. This makes sense, as the orbital evolution parameters match the literature approximations. Hence, it is concluded that the time variations in the gravity field coefficients play a crucial role in tidal dissipation in the coupled model. Interestingly, when calculating the orbital energy dissipation rate via Eq. 42 using the mean value for $C_{22}(t)$ and $S_{22}(t)$, almost no energy is dissipated, supporting the fact that it is indeed the time variations in the gravity field coefficients that are solely responsible for the tidal dissipation. Further study is required in this direction.

REFERENCES

Boué (2019). "Tidal evolution of the Keplerian elements". In: *Celestial Mechanics and Dynamical Astronomy* 131.7.

Boué, Correia, and Laskar (2016). "Complete spin and orbital evolution of close-in bodies using a Maxwell viscoelastic rheology". In: *Celestial Mechanics and Dynamical Astronomy* 126, pp. 31–60.

Correia and Rodríguez (Apr. 2013). "On the equilibrium figure of close-in planets and satellites". In: *The Astrophysical Journal* 767.2, p. 128.

Correia et al. (Nov. 2014). "Deformation and tidal evolution of close-in planets and satellites using a Maxwell viscoelastic rheology". In: *Astronomy & Astrophysics* 571, A50.

Darwin (1880). "On the Secular Changes in the Elements of the Orbit of a Satellite Revolving about a Tidally Distorted Planet". In: *Philosophical Transactions of the Royal Society of London Series I* 171, pp. 713–891.

Dirkx (2015). "Interplanetary laser ranging: Analysis for implementation in planetary science missions". PhD thesis. Delft University of Technology.

Dirkx, Mooij, and Root (Feb. 2019). "Propagation and Estimation of the Dynamical Behaviour of Gravitationally Interacting Rigid Bodies". In: *Astrophysics and Space Science* 364.2, p. 37.

Dirkx et al. (2016). "Dynamical modelling of the Galilean moons for the JUICE mission". In: *Planetary and Space Science* 134, pp. 82–95. ISSN: 0032-0633.

Dirkx et al. (2017). "On the contribution of PRIDE-JUICE to Jovian system ephemerides". In: *Planetary and Space Science* 147, pp. 14–27.

Efroimsky (2012). "Bodily tides near spin-orbit resonances". In: *Celestial Mechanics Dynamical Astronomy* 112.3, pp. 283–330.

– (2018). "Dissipation in a tidally perturbed body librating in longitude". In: *Icarus* 306, pp. 328–354.

Efroimsky and Lainey (2007). "Physics of bodily tides in terrestrial planets and the appropriate scales of dynamical evolution". In: *Journal of Geophysical Research* 112.E12.

Efroimsky and Makarov (Jan. 2013). "Tidal friction and tidal lagging. Applicability limitations of a popular formula for the tidal torque". In: *The Astrophysical Journal* 764.1, p. 26.

Fayolle (2025). "T.B.D." To be defended January 24th 2025. PhD thesis. Delft University of Technology.

Fayolle et al. (2023). "Combining astrometry and JUICE – Europa Clipper radio science to improve the ephemerides of the Galilean moons". In: *Astronomy & Astrophysics* 677, A42.

Fecher, Pail, Gruber, et al. (2017). "GOCO05c: A New Combined Gravity Field Model Based on Full Normal Equations and Regionally Varying Weighting". In: *Surveys in Geophysics* 38.3, pp. 571–590.

Ferraz-Mello (2015). "The small and large lags of the elastic and anelastic tides: the virtual identity of two rheophysical theories". In: *Astronomy & Astrophysics* 579.

Fienga et al. (2019). *INPOP19a planetary ephemerides*. Research Report. IMCCE.

Folkner et al. (2014). "The Planetary and Lunar Ephemerides DE430 and DE431". In: *Interplanetary Network Progress Report* 196.

Fukushima (2008). "Simple, regular, and efficient numerical integration of rotational motion". In: *Astronomical Journal* 135.6, pp. 2298–2322.

Goldreich and Soter (1966). "Q in the solar system". In: *Icarus* 5.4, p. 375.

Goossens et al. (2020). "High-Resolution Gravity Field Models from GRAIL Data and Implications for Models of the Density Structure of the Moon's Crust". In: *Journal of Geophysical Research: Planets* 125.2.

Grasset et al. (2013). "JUpiter ICy moons Explorer (JUICE): An ESA mission to orbit Ganymede and to characterise the Jupiter system". In: *Planetary and Space Science* 78, pp. 1–21.

Henning, O'Connell, and Sasselov (2009). "Tidally Heated Terrestrial Exoplanets: Viscoelastic Response Models". In: *Astrophysical Journal* 707.2, pp. 1000–1015.

Henrard (2006). "The Synchronous Rotation of the Moon". In: ed. by J. Souchay. Vol. 682, pp. 261–276.

Hoolst, Van et al. (2020). "The librations, tides, and interior structure of Io". In: *Journal of Geophysical Research: Planets* 125.

Hurford et al. (2009). "Geological implications of a physical libration on Enceladus". In: *Icarus* 203.2, pp. 541–552.

Kant (1754). *Kant's Cosmogony: as in his Essay on the Retardation of the Rotation of the Earth and his Natural History and Theory of the Heavens*.

Kaplan (2006). *The IAU Resolutions on Astronomical Reference Systems, Time Scales, and Earth Rotation Models*.

Kaula (1964). "Tidal dissipation by solid friction and the resulting orbital evolution". In: *Reviews of Geophysics* 2.4, pp. 661–685.

Khan et al. (2004). "Does the Moon possess a molten core? Probing the deep lunar interior using results from LLR and Lunar Prospector". In: *Journal of Geophysical Research (Planets)* 109, p. 9007.

Lainey (2016). "Quantification of tidal parameters from Solar System data". In: *Celestial Mechanics and Dynamical Astronomy* 126.1-3, pp. 145–156.

Lainey, Arlot, Karatekin, et al. (2009). "Strong tidal dissipation in Io and Jupiter from astrometric observations". In: *Nature* 459, pp. 957–959.

Lainey, Dehant, and Pätzold (2007). "First numerical ephemerides of the martian moons". In: *Astronomy & Astrophysics* 465.3, pp. 1075–1084.

Lainey et al. (2012). "Strong tidal dissipation in Saturn and constraints on Enceladus' thermal state from astrometry". In: *Astrophysical Journal* 752.1.

Lambeck (1980). *The Earth's Variable Rotation: Geophysical Causes and Consequences*. Cambridge University Press.

Lari (2018). "A semi-analytical model of the Galilean satellites' dynamics". In: *Celestial Mechanics and Dynamical Astronomy* 130.8.

Magnanini et al. (2024). "Joint analysis of JUICE and Europa Clipper tracking data to study the Jovian system ephemerides and dissipative parameters". In: *AA* 687, A132.

Martinez (2023). "Translational-rotational couplings in the dynamics of Phobos". Master's thesis. Delft University of Technology.

Murray and Dermott (1999). *Solar system dynamics*.

Pappalardo, Buratti, Korth, et al. (2024). "Science Overview of the Europa Clipper Mission". In: *Space Science Reviews* 220.40.

Park et al. (2021). "The JPL Planetary and Lunar Ephemerides DE440 and DE441". In: *The Astronomical Journal* 161.3, p. 105.

Petit et al. (2010). *IERS Conventions (2010)*. Technical Note. IERS.

Rambaux et al. (2012). "Rotational motion of Phobos". In: *Astronomy & Astrophysics* 548, A14.

Souchay, Mathis, and Tokieda (2013). *Tides in Astronomy and Astrophysics*. Lecture Notes in Physics. Springer.

Turcotte and Schubert (2002). *Geodynamics*. 2nd. Vol. 139. Cambridge University Press, pp. xv + 456.

Williams (Aug. 1994). "Contribution to the Earth's Obliquity Rate, Precession, and Nutation". In: 108, p. 711.

Williams and Boggs (2015). "Tides on the Moon: Theory and determination of dissipation". In: *Journal of Geophysical Research: Planets* 120.4, pp. 689–724.
Williams, Newhall, and Dickey (1996). "Lunar moments, tides, orientation, and coordinate frames". In: *Planetary and Space Science* 44.10, pp. 1077–1080.
Yoder (1981). "The free librations of a dissipative Moon". In: *Philosophical Transactions of the Royal Society of London. Series A, Mathematical and Physical Sciences* 303.1477, pp. 327–338.
Zhang (1992). "Love numbers of the moon and of the terrestrial planets". In: *Earth, Moon, and Planets* 56, pp. 193–207.

Appendix A: Simulation definition

This appendix covers relevant information for the simulations performed, including constants used and the damped initial states for both the Earth and the Moon.

1. Translational equations of motion

For reproducibility purposes, Eq. A1 and Eq. A2 denote the specific equations used for the translational dynamics of the bodies in question, with and without perturbations respectively. Here, $P_{2,0}(x)$ and $P_{2,2}(x)$ define the associated Legendre polynomials for an input x.

$$\begin{aligned}\ddot{\boldsymbol{r}}_{i0} = R^{I/i}\cdot(&-\frac{\mu_i}{r_{i0}^2}\hat{\boldsymbol{r}} - \frac{3\mu_i R_i^2}{2r_{i0}^4}J_2^i\hat{\boldsymbol{r}} \\ &- \frac{9\mu_i R_i^2}{r_{i0}^4}(C_{2,2}^i\cos 2\gamma_0 - S_{2,2}^i\sin 2\gamma_0)\hat{\boldsymbol{r}} \\ &+ \frac{6\mu_i R_i^2}{r_{i0}^4}(C_{2,2}^i\sin 2\gamma_0 + S_{2,2}^i\cos 2\gamma_0)\boldsymbol{K}\times\hat{\boldsymbol{r}}),\end{aligned} \tag{A1}$$

$$\begin{aligned}\ddot{\boldsymbol{r}}_{i0} = \frac{-\mu_i R_i^2}{r_{i0}^2}\Bigg(&\left(\frac{1}{R_i^2} - \frac{3J_2^i}{r_{i0}^2}P_{2,0}(\sin(\phi_0))\right. \\ &\left. + \frac{3P_{2,2}(\sin(\phi_0))}{r_{i0}^2}(C_{2,2}^i\cos(2\vartheta_0) + S_{2,2}^i\sin(2\vartheta_0))\right)\hat{\boldsymbol{r}} \\ &+ \Bigg(\frac{3\sin(\phi_0)\cos(\phi_0)J_2^i}{r_{i0}^2} \\ &+ \frac{6\sin(\phi_0)\cos(\phi_0)}{r_{i0}^2}(C_{2,2}^i\cos(2\vartheta_0) + S_{2,2}^i\sin(2\vartheta_0))\Bigg)\hat{\boldsymbol{\phi}} \\ &- \left(\frac{2P_{2,2}(\sin(\phi_0))}{r_{i0}^2\cos(\phi_0)}(-C_{2,2}^i\sin(2\vartheta_0) + S_{2,2}^i\cos(2\vartheta_0))\right)\hat{\boldsymbol{\vartheta}}\Bigg) \\ &- \sum_j \mu_j\left(\frac{\hat{\boldsymbol{r}}_{ji}}{r_{ji}^2} - \frac{\hat{\boldsymbol{r}}_{j0}}{r_{j0}^2}\right).\end{aligned} \tag{A2}$$

In order to evaluate these equations, the positions of all bodies are required, as well as physical parameters of the propagated body, such as its radius and the gravity field coefficients. The rest of this section will define these values where necessary.

2. Earth

This section will denote the constants used for the Earth during the propagations.

- Gravity field: GOCO05c developed by Fecher et al. (2017). The Earth's reference radius is 6378.1km and its gravitational parameter $\mu_0 = 398600.4415$ km^3/s^2. The degree 2 coefficients have been included.
- Tidal parameters: The Maxwell relaxation time τ_e and global relaxation time τ_2 for the Earth from Correia et al. (2014).
- Inertia tensor: Calculated from the degree 2 gravity field coefficients using Eq. 9, where $\bar{I}_k$=0.3307007 is the mean moment of inertia, which is taken from Williams (1994).
- Rotation model: The orientation of the Earth is retrieved as it was at J2000 from the IAU (International Astronomical Union) Earth frame Kaplan (2006).

3. Moon

This section will denote the constants used for the Moon during the propagations.

- Gravity field: gggrx_1200b from GRAIL data Goossens et al. (2020). The Moon's reference radius is 1737.4km and its gravitational parameter $\mu_i = 4902.8001218468$ km^3/s^2. The degree 2 coefficients have been included.
- Tidal parameters: The degree 2 Love number k_2=0.024059 and quality factor Q=37.5 of the Moon are taken from Lainey (2016), from which τ_2 and τ_e are calculated using Eq. 44-46 of Section 4. It follows that τ_2= 12794424s and τ_e = 830598914s.
- Inertia tensor: Calculated from the degree 2 gravity field coefficients using Eq. 9, where $\bar{I}_k$=0.3929, which is taken from Williams et al. (1996).

4. Third bodies

This section will denote the constants used for the third bodies during the propagations.

- Sun: The mass of this body (and the Moon and Earth) is taken from the INPOP19a ephemerides product Fienga et al. (2019). Its location is determined from the same source in combination with the DE440 ephemerides Park et al. (2021).

- Jupiter: The mass of Jupiter and its position with respect to the Jovian barycenter is taken from the NOE-5-2021 ephemerides Fayolle et al. (2023). The INPOP19a ephemerides (Fienga et al. (2019)) are then used to compute its position with respect to the correct body-fixed frame.

5. Numerical integration

The equations of motion have been numerically integrated using custom software created by the author and validated with Tudat (TU Delft Astrodynamics Toolbox). In this work, all simulations have been performed using a DOP583 integrator with a fixed step-size of 80 minutes, which integrates the equations of motion in Eq. 34-36. For reproducibility purposes, some of the used initial states will be provided in this section. Eq. A3 denotes the nominal translational and rotational initial state as well as the initial value for the gravity field coefficients $Z^{\nu}_{l,m}$ for the Earth. Similarly, Eq. A4 the initial state used for the nominal propagation of the Moon.

$$\boldsymbol{x} = \begin{bmatrix} -359680329.2763155 \\ -82373776.21032083 \\ -1633942.954798689 \\ 278.35337268506817 \\ -953.4813336331438 \\ -379.1941059087945 \\ 0.43537911071282687 \\ 0.11317597257132578 \\ -0.1421998113314148 \\ 0.881711655133172 \\ 5.482513268821296 \cdot 10^{-20} \\ 1.3585528455022242 \cdot 10^{-19} \\ 7.262116762072311 \cdot 10^{-05} \\ 0.0010729669706076347 \\ -6.088364113441088 \cdot 10^{-10} \\ -4.730759190004066 \cdot 10^{-10} \end{bmatrix} \tag{A3}$$

$$\boldsymbol{x} = \begin{bmatrix} -382196934.10039043 \\ -89516988.5691146 \\ -2479200.1476683454 \\ 159.61840391207076 \\ -919.9155330758256 \\ -357.0089660106524 \\ -0.9816184698077 \\ -0.17958200435736416 \\ -0.027926528328146343 \\ -0.05827171233733275 \\ 2.5755725738338057 \cdot 10^{-15} \\ -4.552044969265712 \cdot 10^{-17} \\ 2.6919105511554092 \cdot 10^{-06} \\ 9.237956217201704 \cdot 10^{-06} \\ 2.720599025660953 \cdot 10^{-06} \\ 1.7398952470744585 \cdot 10^{-10} \end{bmatrix} \tag{A4}$$

There are several more initial states used during this work. In determining the behaviour of the coupled model for a range of relaxation times, each one of these scenarios has its own damped initial state associated with it. Since this would make the appendix quite lengthy, they are not included here and the interested user is referred to the linked code repository.

Appendix B: Quality factor and love numbers

This section aims to explain how Eq. 13 and Eq. 12 of the main paper body are consistent with each other. In other words, it aims to show how a complex Love number can be interpreted as a tidal lag. For comfort, Eq. 12 and Eq. 13 are repeated below in Eq. B1 and Eq. B2:

$$\Delta\bar{C}^{i}_{l,m} - i\Delta\bar{S}^{i}_{l,m} = \frac{k^{i}_{l}}{2l+1} \times \\ \times \sum_{j} \frac{\mu_j}{\mu_i} \left(\frac{R_i}{r_j}\right)^{l+1} \bar{P}_{l,m}(\sin\phi_j) e^{-im\vartheta_j}, \tag{B1}$$

$$Q^{j}_{i} = \frac{|k^{i}_{2}|}{\mathrm{Im}(k^{i}_{2})}. \tag{B2}$$

Here, Eq. B1 contains k^{i}_{l} instead of $k^{i}_{l,m}$ because, as discussed in the main body of the paper, variations in m for a given l are small for the Love numbers. In its most general form, and assuming a constant k^{l}_{i} for the remainder of this section, k^{i}_{l} can contain both a real and complex part:

$$k^{i}_{l} = \mathrm{Re}(k^{i}_{l}) + i\mathrm{Im}(k^{i}_{l}), \tag{B3}$$

with i the complex number. Splitting Eq. B1 in its real and imaginary part results in the following two equations:

$$\Delta\bar{C}^i_{l,m} = \frac{\mathrm{Re}(k^i_l)}{2l+1}\times \\ \times \sum_j \frac{\mu_j}{\mu_i}\left(\frac{R_i}{r_j}\right)^{l+1} \bar{P}_{l,m}(\sin\phi_j)\cos m\vartheta_j, \quad \text{(B4)}$$

$$\Delta\bar{S}^i_{l,m} = \frac{\mathrm{Im}(k^i_l)}{2l+1}\times \\ \times \sum_j \frac{\mu_j}{\mu_i}\left(\frac{R_i}{r_j}\right)^{l+1} \bar{P}_{l,m}(\sin\phi_j)\sin m\vartheta_j. \quad \text{(B5)}$$

Thus, the tidal variations of C^i_{22} depend on the real part of k^i_l, while the tidal variations of S^i_{22} depend on its imaginary part. As was shortly discussed in section 2.4 and section 3.1, variations in S^i_{22} lead to tidal dissipation. Hence, Eq. B5 demonstrates a direct correlation between the magnitude of $\mathrm{Im}(k^i_l)$ and the magnitude of the variations in S^i_{22} and hence the magnitude of the tidal dissipation and tidal lag. As a result, it follows that for a constant k^i_l, the magnitude of its complex part has a direct correlation with the tidal lag, which is expressed through the quality factor Q as given in Eq. B2.

Appendix C: Reference frame Moon

Before the results for the tides raised on the Moon by itself can be compared to approximations from literature, it is important for them to be in a common reference frame. Generally, the choice of reference frame is such that the body-fixed x-axis of the Moon coincides with the moon-to-planet line at $M = 0$. This has been ensured for the cases investigated (i.e. the various k_2/Q values investigated), with all *mean* values over time over integer normal modes of the longitude of the Earth as seen from the Moon γ at $M = 0$ equal to zero.

The whole propagation period (5000 days) contains almost 200 orbits, and hence it is worthwile to investigate several individual orbits, so see whether $\gamma(M = 0)$ is not too much influenced by normal modes to influence the results. To this end, Fig. 16a and Fig. 16b show $\gamma(M = 0)$ over a propagation period before and after rotating the reference frame as specified. As can be seen, the rotational modes are still present and actively being damped over the propagation period, but are substantially smaller than the static offset in the longitude. As a result, they are deemed to not influence the results significantly, and after rotating the reference frame such that the mean $\gamma(M = 0)$ over the propagated period, this reference frame is used to compare the results of the coupled model to the approximations from literature. Note that, ideally, these rotational normal modes are *completely* damped out, but that is very difficult to achieve.

Appendix D: Damping algorithm

The damping algorithm used in this work is derived from Rambaux et al. (2012). This algorithm is designed to find an initial state of a satellite in spin-orbit resonance where the normal modes have been damped, while preserving rotation around the z-axis. This is done by introducing a virtual torque into the equations of motion. Conceptually, this virtual torque $\boldsymbol{\Gamma}_d$ counteracts the rotation of a body around it's body fixed x- and y-axis, and is mathematically defined as

$$\boldsymbol{\Gamma}_d = -\frac{1}{\tau_d}\boldsymbol{I}(\boldsymbol{\omega} - \boldsymbol{\omega}_0), \quad \text{(D1)}$$

with τ_d a given dissipation time, $\boldsymbol{\omega}$ the rotation rate of the body expressed in its body-fixed frame and $\boldsymbol{\omega}_0$ its rotation rate in pure synchronous motion (i.e. the desired rotation rate), meaning it will only have a non-zero component along the z-axis. The equations of motion in Eq. 34-36 are then propagated with this additional virtual torque. Subsequently, the resulting final state is propagated backwards in time without the virtual torque, resulting in an initial state that should not give rise to normal modes when propagated. This does not work perfectly and thus it becomes an iterative process, and as Martinez (2023) points out, it will likely take several iterations to obtain an initial state with a sufficiently damped out normal mode.

This algorithm was initially designed by Rambaux et al. (2012) for damping rotational normal modes in rigid bodies. This algorithm is however ineffective for damping the normal modes in the gravity field coefficients, and specifically for S_{22}, which suffered the most from this. Hence, for this work the algorithm has been modified slightly to account for this. Analogously to how a virtual torque is introduced to damp the rotation, a similar equation can be used to damp the normal modes in the gravity field coefficients:

$$\dot{Z}^\nu_{l,m} = -\frac{1}{\tau_l}(Z_{l,m} - Z^e_{l,m}), \quad \text{(D2)}$$

with $Z_{l,m}$ the current value of the gravity field coefficient. The goal of this equation is to aid the process of the gravity field coefficients converging to stable values where the normal modes have been damped out. Combined with natural tidal dissipation occurring during the propagation, this should result in the normal modes being damped out in the gravity field coefficients.

The results of the damping algorithm have partly already been implicitly shown in the main body of this work, and will be supplemented in this appendix to add confidence to the results. Fig. 12 shows the frequency content of the gravity field coefficients of the Moon, showing peaks at the mean motion and integer multiples, but no peak at the rotational normal mode, indicating that

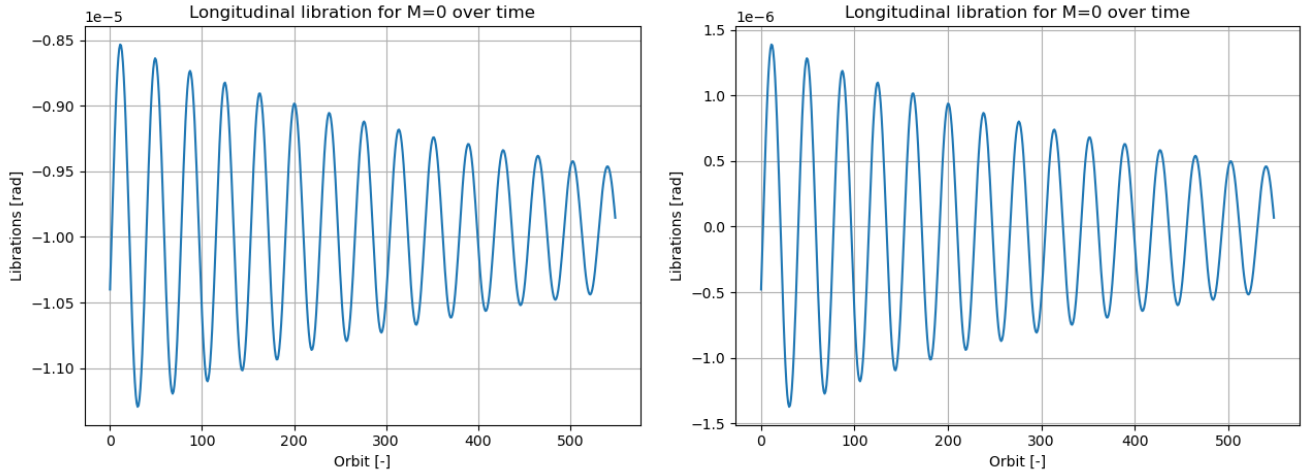

(a) $\gamma(M = 0)$ over a number of orbits before rotating the reference frame.

(b) $\gamma(M = 0)$ over a number of orbits after rotating the reference frame.

Figure 16: Quantification of the reference frame offset of the Moon's body fixed reference frame.

the effect of normal modes has been successfully damped in the gravity field coefficients.

In Fig. 16a and Fig. 16b, the Moon-fixed angular coordinates of the Earth are plotted in a longitude-latitude map before and after damping respectively, with the (0,0) coordinate being the moon-planet line. These figures show the effect of the damping algorithm on the rotation of the Moon, ensuring it is tidally-locked as it is in reality. Before the algorithm is applied, the Moon's body fixed x-axis is seen to deviate from the moon-planet line by about 15° in latitude and 30° in longitude as a result of librations and the rotational normal modes. The damping algorithm removes all oscillations occuring at the frequency of the normal mode and isolates the effect of librations due to forcings. Note that the deviation in latitude essentially becomes 0° as expected, considering the dynamics of the problem.

The difference in the frequency spectrum between the undamped and damped longitudinal librational motion of the Moon is displayed in Fig. 17, with Fig. 17a describing the undamped scenario and Fig. 17b describing the damped scenario. It is worth noting that the peak at the frequency of the normal mode is damped from ∼10 to ∼0.1 degrees after the damping algorithm is applied. These results add confidence in the fact that the tidal lock is conserved after applying the damping algorithm when propagating the Earth-Moon system using the coupled model. Furthermore, since the behaviour of S_{22} directly influences the evolution of the semi-major axis, any normal modes not damped will manifest themselves in the semi-major axis as oscillations at the frequency of the normal mode, which could influence the results for the rates of change of the semi-major axis. Fig. 18 and Fig. 19 display the semi-major axis of the Moon's orbit before and after the damping algorithm has been applied respectively. Before damping, it is clear that there is a periodic oscillation in the semi-major axis which can heavily influence the results depending on the interval over which the derivative is calculated. However, after the normal modes have been damped using the algorithm, the secular trend in the semi-major axis caused by tidal effects becomes clear, and it can reliably be extracted from the state history of the results.

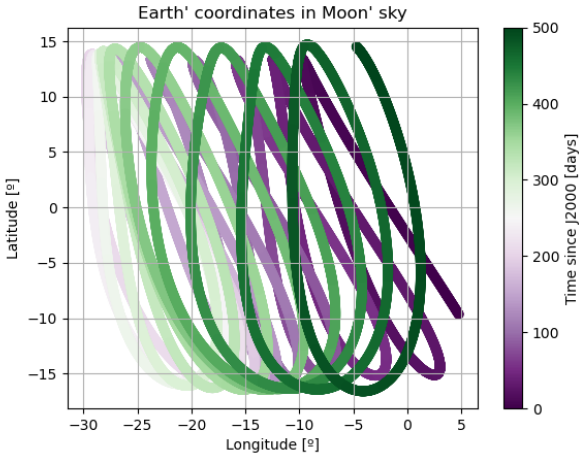

(a) Earth's coordinates in the Moon's sky before damping.

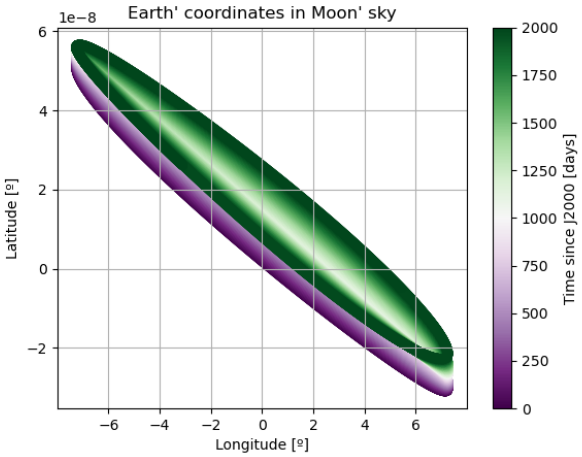

(b) Earth's coordinates in the Moon's sky after damping.

Figure 17: Quantification of the influence of the damping algorithm on the orientation of the Earth in the Moon's sky in a latitude-longitude map.

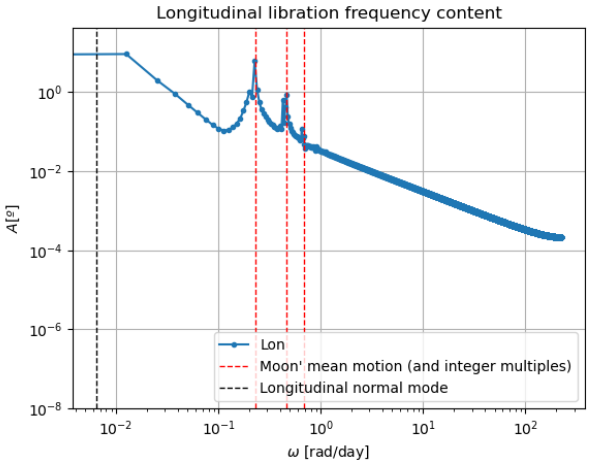

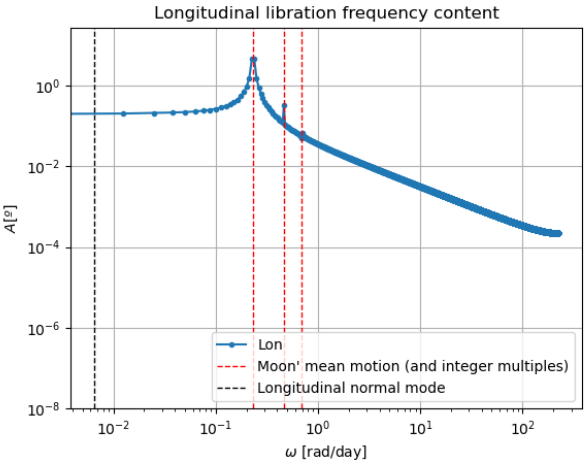

(a) Frequency spectrum of the longitudinal libration before damping. (b) Frequency spectrum of the longitudinal libration after damping.

Figure 18: Influence of the damping algorithm quantified in the frequency spectra of the longitudinal libration. Note the damping of the longitudinal normal mode by approximately two orders of magnitude.

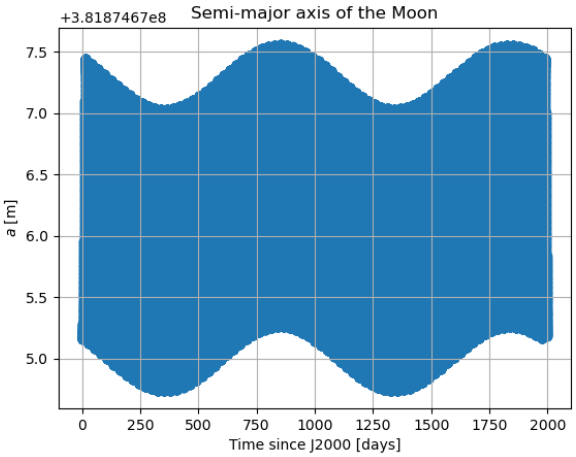

(a) Influence of the rotational normal modes on the semi-major axis for an arbitrary case.

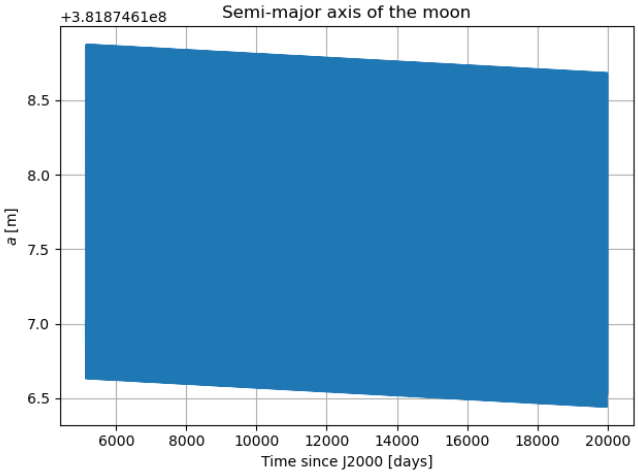

(b) Evolution of the semi-major axis after the rotational normal modes have been damped for an arbitrary case.

Figure 19: Influence of the damping algorithm quantified in the evolution of the semi-major axis. This figure demonstrates why the damping algorithm is such a crucial part of the coupled model, as its influence is far too large to detect any secular changes due to tidal effects. Note that these propagations have slightly different constants, but this does not change the message it conveys.

4

Conclusions and recommendations

This section will answer the research questions posed at the start of the thesis. Furthermore, recommendations for future research will be formulated based on the results obtained in this work.

4.1. Conclusions

This section will answer the research questions posed, starting with the sub-questions and working up to the main research question.

- **How can physically realistic initialization reliably be achieved for the system(s) in question?**

  In this work, it was found that a physically realistic initial state can be found by using a modified version of the algorithm proposed by Rambaux et al. (2012), with the goal of damping the rotational normal modes. Since the algorithm is designed for rigid bodies, it has been modified for this work to mimic tidal dissipation and ensure that the gravity field coefficients also become free of normal modes. Nevertheless, it must be noted that the normal modes, despite being significantly damped, still were present in the results, but were insignificant enough to not play a significant role in the results.

- **What is the effect of the coupled model for an unperturbed and perturbed system with tides raised on the primary?**

  In studying the position differences between the uncoupled and coupled trajectories, it was found that the coupled trajectory got ahead of the uncoupled trajectory by 20 m after 13 years and 8 months. In the radial and out-of-plane direction, small oscillations with an amplitude of several centimeters were detected. The difference in semi-major axis grew up to 1.2 cm over the same period.

  The investigated parameters are in good accordance with the equations they have been compared to. Specifically, the gravity field coefficients C_{22} and S_{22} from the coupled model showed mean values over time over an integer number of orbits of $-3.927 \cdot 10^{-14}$ and $1.858 \cdot 10^{-14}$ respectively; these are compared to approximations for C_{22} and S_{22} from Eq. 44 and 45 of the stand-alone paper, which yield mean values of $-3.324 \cdot 10^{-14}$ and $2.302 \cdot 10^{-14}$. Their time variations are also in good accordance, with C_{22} and S_{22} from the coupled model having a mean amplitude of $5.273 \cdot 10^{-9}$ and $5.269 \cdot 10^{-9}$ respectively. From Eq. 44 and 45, both C_{22} and S_{22} show a mean amplitude of $5.285 \cdot 10^{-9}$. This demonstrates that the coupled model can capture the time variations in gravity field coefficients well compared to simplified approaches used in literature.

  The evolution of the semi-major axis and eccentricity are compared to approximations used in literature, denoted as Eq. 37 and Eq. 38 in the stand-alone paper. The evolution of the semi-major axis shows good accordance with the uncoupled model and Eq. 37 for a range of tested relaxation times. Furthermore, its results are in closer accordance with Eq. 37 than the uncoupled model, and remaining differences are attributed to the assumptiosn that are made in deriving Eq.

37, which the coupled model does not need. For the eccentricity evolution, both the uncoupled and coupled model fail to capture the rate of change as projected by Eq. 38. This is not a failure of the coupled model, but rather, the secular signature in the evolution of the eccentricity is too small to detect compared to its large time variations. Lastly, when including perturbations their effect on the tidal response was limited as expected, and could be left out for the Earth-Moon system. However, more complex systems such as the Galilean moons would require the modelling of perturbations.

- **What is the effect of the coupled model for an unperturbed and perturbed system with tides raised on the secondary?**

  In studying the position differences between the uncoupled and coupled trajectories for tides raised on the Moon by itself, it was found that the difference in semi-major axis grew up to 10 cm over the propagation period of 13 years and 8 months, almost 10x as large as the difference was for tides raised on the Earth by the Moon. This indicates that the uncoupled model has much more difficulty accurately modelling the tides raised on the Moon by itself, and likely in general will have trouble to do so for any synchronous satellite.

  The evolution of the semi-major axis and eccentricity both showed good accordance with the approximations in Eq. 39 and Eq. 40 for a wide range of k_2/Q values for the tides raised on the Moon by itself, meaning the coupled model produces results in accordance with approximations used in literature regardless of the k_2/Q value that is considered. Interestingly, this also confirms that the effective evolution of the semi-major axis is modelled more accurately with Eq. 39 and not Eq. 41. Furthermore, Eq. 39 is multiplied with Eq. 53 to take into account the effect of physical librations on tidal dissipation, resulting in a closer approximation with the coupled model. Since the coupled model automatically includes this, this again confirms the idea that the coupled model provides an elegant manner to achieve the same results as simplified approximations do.

  Interestingly, while the orbital evolution rates matches what theory would dictate, the tidal dissipation manifests itself differently. The mean value $\bar{S}_{22}$ from the approximation in Eq. 45 and the coupled model are equal to $1.972 \cdot 10^{-8}$ and $-3.778 \cdot 10^{-13}$ respectively, differing by 5 orders of magnitude and with $\bar{S}_{22}$ of the coupled model effectively equal to zero. Despite this, the orbital energy dissipated $\dot{E}_{orb}$ due to tidal effects matches the theoretical orbital energy dissipation rate well, which is calculated using Eq. 42 of the stand-alone paper. The values from the coupled model and Eq. 42 are equal to -14.89 GJ/s and -14.44 GJ/s respectively. This is expected, as the orbital evolution rates match very well between the coupled model and Eq. 39 and 40. Curiously, calculating this same number using $\bar{C}_{22}$ and $\bar{S}_{22}$ displayed in Table 7 of the stand-alone paper (i.e., the mean values over time over an integer number of orbits of C_{22} and $S22$) results in almost no energy being dissipated ($-6.0 \cdot 10^{-4}$ GJ/s). This gives rise to the following preliminary hypothesis: $\bar{S}_{22}$ is actually equal to zero over one orbit regardless of the value of k_2/Q, and it is the time-variation and magnitude of the periodic oscillations in S_{22} (and C_{22}) that change and give rise to tidal dissipation. For the uncoupled model, the static offset from zero of S_{22} (i.e. a non-zero mean) causes tidal dissipation. Thus, in the coupled model tidal dissipation manifests itself differently through the time-variations of the gravity field coefficients, and not their mean values.

What is the effect of using a fully coupled model compared to current-day models in natural satellites' dynamics modelling in planetary systems?

After having answered the individual sub-questions, the main research question will now be answered in the following paragraphs.

This work has considered the usage of a coupled modelling approach that concurrently models the orbit, rotation and tidal deformation of the gravity field of a natural satellite and applies it to the Earth-Moon system. This model has been compared against simplified, uncoupled models and approximations used in literature, and has leveraged this comparison to draw conclusions regarding the orbital evolution of satellites and how tidal dissipation contributes towards this. This coupled model requires a coupled initial state, which, when undamped, contains rotational normal modes that heavily influence the rotation and tidal deformation of a natural satellites' gravity field. Hence, an algorithm has successfully been designed to reliably find damped initial states for specific dynamical environments.

When analysing the tides raised on the Earth by the Moon, it was found that, when comparing the uncoupled and coupled model, couplings induce along-track position differences growing up to 20 m. Furthermore, the evolution of the gravity field coefficients and orbital evolution parameter semi-major axis a matches well independently of the value of k_2/Q investigated between the results of the coupled model and approximations retrieved from literature (Eq. 37, 38, 43-45 of the stand-alone paper). The signature of the evolution of the eccentricity e was too small to detect.

Similarly, when analysing the tides raised on the Moon by itself, the orbital evolution parameters a and e agree well between the results of the coupled model and approximations retrieved from literature (Eq. 39, 40), although the tidal dissipation manifests itself differently compared to the uncoupled model and approximations (Eq. 45). For the coupled model, the mean value of S_{22} is equal to zero and it is the time variations of the coefficient (and of C_{22}) that cause tidal dissipation, whereas for simplified, uncoupled approaches it is the non-zero mean of the gravity field coefficients that is responsible for tidal dissipation. Note that despite this difference, the orbital energy dissipated matches theory (Eq. 42), which makes sense as the orbital evolution parameters are in line with approximations from literature. Lastly, note that the evolution of the semi-major axis is in line with Eq. 39 and not Eq. 41, and includes the tidal dissipation caused by physical librations, giving insights into what theoretical approximations are closer to reality and showing that the coupled model automatically includes them. This gives rise to the following preliminary hypothesis: $\bar{S}_{22}$ is actually equal to zero over one orbit regardless of the value of k_2/Q, and it is the time-variation and magnitude of the periodic oscillations in S_{22} (and C_{22}) that change and give rise to tidal dissipation.

4.2. Recommendations

This section will propose several further steps that could be taken based on this work.

- This thesis has shown that the behaviour of the Moon's $S_{22}(t)$ coefficient in the coupled model differs quite significantly from the approximation in Eq. 45 of the stand-alone paper, yet produces correct values for the orbital migration rates of the satellite. To gain a deeper understanding of this behaviour, it is worthwhile to perform a deeper analysis of the time variations of these coefficients, as well as applying this model to another satellite to see whether the same behaviour is reproduced. Interesting candidates could be the Jovian moons, or a moon of Saturn, as they have future relevance too with missions making their way there.
- In this thesis, the normal modes have been damped using the algorithm described in Appendix D of the research paper in Chapter 3. However, to *completely* damp the normal modes, the algorithm needs to be ran for an exceedingly long time. This algorithm has a lot of room for improvement, both in terms of computational speed and efficiency, and hence is an interesting candidate in speeding up computations using the coupled model. Furthermore, it is possible that the current algorithm itself can be refined by introducing a more efficient way of damping the rotational normal modes.
- The coupled model, having been verified for the perturbed Earth-Moon system, can now be applied to more difficult systems, with an interesting candidate being the Jovian system in light of future missions headed for this system. It will be interesting to see how it fares in such a system, especially when the full state of all moons are propagated concurrently.
- As a simple first test case, the algorithm proposed was applied to the Jovian system. It produced a damped initial state for Ganymede, but failed to converge to physically realistic initial states for Io and Europa, resulting in negative rotation rates for both. Before applying the coupled model to the Jovian system, it will be interesting to see whether it can be uncovered why the algorithm fails for these particular moons. This may in part be caused by the complexities of the Laplace resonance.
- For this work, a simple Maxwell model has been used as rheology, neglecting the fact that satellites generally consist of multiple layers and have a much more complex interior. Despite this not being the most relevant step for the coupled model, it is interesting to see how changing the rheology models results in physically different behaviour.
- In this work, perturbations were of limited influence on the results. However, it has become apparent that when perturbations are included, it becomes extremely difficult to reliably extract secular evolution rates for the semi-major axis and eccentricity caused by tidal effects. It hence

becomes a point of interest to try and develop a method that can do so, or move to different parameters to quantify the effect of tidal dissipation.

References

Altman (1972). “A unified state model of orbital trajectory and attitude dynamics”. In: *Celestial Mechanics* 6, p. 425.

Andrade (1910). “On the viscous flow in metals, and allied phenomena”. In: *Proceedings of the Royal Society of London. Series A* 84, pp. 1–12.

Bagheri et al. (2022). “Chapter Five - Tidal insights into rocky and icy bodies: an introduction and overview”. In: *Geophysical Exploration of the Solar System*. Vol. 63, pp. 231–320.

Bills et al. (2005). “Improved estimate of tidal dissipation within Mars from MOLA observations of the shadow of Phobos”. In: *Journal of Geophysical Research (Planets)* 110, p. 7004.

Bois, I. Wytrzyszczak, and A. Journet (1992). “Planetary and figure-figure effects on the moon’s rotational motion”. In: *Celestial Mechanics and Dynamical Astronomy* 53, pp. 185–201.

Boué (2019). “Tidal evolution of the Keplerian elements”. In: *Celestial Mechanics and Dynamical Astronomy* 131.7.

Boué, Correia, and Laskar (2016). “Complete spin and orbital evolution of close-in bodies using a Maxwell viscoelastic rheology”. In: *Celestial Mechanics and Dynamical Astronomy* 126, pp. 31–60.

Christensen (1971). *Theory of Viscoelasticity*. London, W1X6BA: Academic Press, pp. 16–20. ISBN: 9780121742508.

Colombo (1965). “Rotational Period of the Planet Mercury”. In: *Nature* 208, p. 575.

Correia and Rodríguez (Apr. 2013). “On the equilibrium figure of close-in planets and satellites”. In: *The Astrophysical Journal* 767.2, p. 128.

Correia et al. (Nov. 2014). “Deformation and tidal evolution of close-in planets and satellites using a Maxwell viscoelastic rheology”. In: *Astronomy & Astrophysics* 571, A50.

Danby (1988). *Fundamentals of Celestial Mechanics*. 2nd ed. Virginia: Willmann-Bell, Inc.

Darwin (1880). “On the Secular Changes in the Elements of the Orbit of a Satellite Revolving about a Tidally Distorted Planet”. In: *Philosophical Transactions of the Royal Society of London Series I* 171, pp. 713–891.

Dehant and Mathews (May 2015). *Precession, Nutation and Wobble of the Earth*. ISBN: 9781107092549.

Dirkx (2015). “Interplanetary laser ranging: Analysis for implementation in planetary science missions”. PhD thesis. Delft University of Technology.

Dirkx, Mooij, and Root (Feb. 2019). “Propagation and Estimation of the Dynamical Behaviour of Gravitationally Interacting Rigid Bodies”. In: *Astrophysics and Space Science* 364.2, p. 37.

Dirkx et al. (Sept. 1, 2014). “Phobos laser ranging: Numerical Geodesy experiments for Martian system science”. In: *Planetary and Space Science* 99, pp. 84–102.

Dirkx et al. (2016). “Dynamical modelling of the Galilean moons for the JUICE mission”. In: *Planetary and Space Science* 134, pp. 82–95. ISSN: 0032-0633.

Efroimsky (2012). “Bodily tides near spin-orbit resonances”. In: *Celestial Mechanics Dynamical Astronomy* 112.3, pp. 283–330.

— (2018). “Dissipation in a tidally perturbed body librating in longitude”. In: *Icarus* 306, pp. 328–354.

Efroimsky and Lainey (2007). “Physics of bodily tides in terrestrial planets and the appropriate scales of dynamical evolution”. In: *Journal of Geophysical Research* 112.E12.

Efroimsky and Makarov (Jan. 2013). “Tidal friction and tidal lagging. Applicability limitations of a popular formula for the tidal torque”. In: *The Astrophysical Journal* 764.1, p. 26.

Fayolle (2025). “T.B.D.” To be defended January 24th 2025. PhD thesis. Delft University of Technology.

Fayolle et al. (2023). “Combining astrometry and JUICE – Europa Clipper radio science to improve the ephemerides of the Galilean moons”. In: *Astronomy & Astrophysics* 677, A42.

Ferraz-Mello (2015). “The small and large lags of the elastic and anelastic tides: the virtual identity of two rheophysical theories”. In: *Astronomy & Astrophysics* 579.

Fienga et al. (2019). *INPOP19a planetary ephemerides*. Research Report. IMCCE.

Folkner et al. (2014). “The Planetary and Lunar Ephemerides DE430 and DE431”. In: *Interplanetary Network Progress Report* 196.

Fukushima (2008). “Simple, regular, and efficient numerical integration of rotational motion”. In: *Astronomical Journal* 135.6, pp. 2298–2322.
Goldman (2011). “Understanding quaternions”. In: *Graphical Models* 73, pp. 21–49.
Goldreich and Soter (1966). “Q in the solar system”. In: *Icarus* 5.4, p. 375.
Henning, O’Connell, and Sasselov (2009). “Tidally Heated Terrestrial Exoplanets: Viscoelastic Response Models”. In: *Astrophysical Journal* 707.2, pp. 1000–1015.
Henrard (2006). “The Synchronous Rotation of the Moon”. In: ed. by J. Souchay. Vol. 682, pp. 261–276.
Hoolst, Van et al. (2020). “The librations, tides, and interior structure of Io”. In: *Journal of Geophysical Research: Planets* 125.
Hurford et al. (2009). “Geological implications of a physical libration on Enceladus”. In: *Icarus* 203.2, pp. 541–552.
Hut (June 1981). “Tidal evolution in close binary systems.” In: 99, pp. 126–140.
Jeffreys (1976). *The Earth: Its Origin, History, and Physical Constitution*. 6th ed. Cambridge University Press.
Kant (1754). *Kant’s Cosmogony: as in his Essay on the Retardation of the Rotation of the Earth and his Natural History and Theory of the Heavens*.
Kaula (1964). “Tidal dissipation by solid friction and the resulting orbital evolution”. In: *Reviews of Geophysics* 2.4, pp. 661–685.
Khan et al. (2004). “Does the Moon possess a molten core? Probing the deep lunar interior using results from LLR and Lunar Prospector”. In: *Journal of Geophysical Research (Planets)* 109, p. 9007.
Konopliv et al. (2011). “Mars high resolution gravity fields from MRO, Mars seasonal gravity, and other dynamical parameters”. In: *Icarus* 211, pp. 401–428.
Konopliv et al. (2013). “The JPL lunar gravity field to spherical harmonic degree 660 from the GRAIL Primary Mission”. In: *Journal of Geophysical Research: Planets* 118.7, pp. 1415–1434.
Krasinsky (2002). “Dynamical History of the Earth–Moon System”. In: *Celestial Mechanics and Dynamical Astronomy* 84, pp. 27–55.
Lainey (2016). “Quantification of tidal parameters from Solar System data”. In: *Celestial Mechanics and Dynamical Astronomy* 126.1-3, pp. 145–156.
Lainey, Dehant, and Pätzold (2007). “First numerical ephemerides of the martian moons”. In: *Astronomy & Astrophysics* 465.3, pp. 1075–1084.
Lainey, Duriez, and Vienne (2004). “New accurate ephemerides for the Galilean satellites of Jupiter. I. Numerical integration of elaborated equations of motion”. In: *Astronomy & Astrophysics* 420.3, pp. 1171–1183.
Lainey et al. (2012). “Strong tidal dissipation in Saturn and constraints on Enceladus’ thermal state from astrometry”. In: *Astrophysical Journal* 752.1.
Lainey et al. (2019). “Interior properties of the inner saturnian moons from space astrometry data”. In: *Icarus* 326, pp. 48–62.
Lambeck (1980). *The Earth’s Variable Rotation: Geophysical Causes and Consequences*. Cambridge University Press.
— (1988). *Geophysical Geodesy: The Slow Deformations of the Earth*. Oxford Science Publications.
Lari (2018). “A semi-analytical model of the Galilean satellites’ dynamics”. In: *Celestial Mechanics and Dynamical Astronomy* 130.8.
Lemoine et al. (2013). “High□degree gravity models from GRAIL primary mission data”. In: *Journal of Geophysical Research: Planets* 118.8, pp. 1676–1698.
Love (1911). *Some Problems of Geodynamics*. University Press.
Magnanini et al. (2024). “Joint analysis of JUICE and Europa Clipper tracking data to study the Jovian system ephemerides and dissipative parameters”. In: *AA* 687, A132.
Maistre, Le et al. (2013). “Phobos interior from librations determination using doppler and star tracker measurements”. In: *Planetary and Space Science* 85, pp. 106–122.
Martinez (2023). “Translational-rotational couplings in the dynamics of Phobos”. Master’s thesis. Delft University of Technology.
Mignard (1979). “Evolution of the lunar orbit revisited I”. In: *Moon and the Planets* 20.3, pp. 301–315.
— (1980). “The evolution of the lunar orbit revisited II”. In: *Moon and the Planets* 23.2, pp. 185–201.
Mitchell (1995). “Anelastic structure and evolution of the continental crust and upper mantle from seismic surface wave attenuation”. In: *Reviews of Geophysics* 33.4, pp. 441–462.

Mol (2021). “A Coupled 2D Translational-Rotational-Tidal model on Solar system bodies using a Maxwell viscoelastic rheology”. Master’s thesis. Delft University of Technology.
Munk and MacDonald (1975). *The Rotation of the Earth: A Geophysical Discussion*. revised.
Murray and Dermott (1999). *Solar system dynamics*.
Park et al. (2021). “The JPL Planetary and Lunar Ephemerides DE440 and DE441”. In: *The Astronomical Journal* 161.3, p. 105.
Peale (Apr. 1969). “Generalized Cassini’s Laws”. In: 74, p. 483.
Peale and Cassen (1978). “Contribution of tidal dissipation to lunar thermal history”. In: *Icarus* 36.2, pp. 245–269.
Peltier (1974). “The impulse response of a Maxwell Earth”. In: *Rev. Geophys. Space Phys.* 12, pp. 649–669.
Petit et al. (2010). *IERS Conventions (2010)*. Technical Note. IERS.
Rambaux et al. (2010). “Librational response of Enceladus”. In: *Geophysical Research Letters* 37.L04202.
Rambaux et al. (2012). “Rotational motion of Phobos”. In: *Astronomy & Astrophysics* 548, A14.
Rao (2006). *Dynamics of Particles and Rigid Bodies: A Systematic Approach*. Equation (2–128). New York: Cambridge University Press, p. 47. ISBN: 978-0-511-34840-2.
Remus et al. (2012). “Anelastic tidal dissipation in multi-layer planets”. In: *Astronomy & Astrophysics* 54.
Schutz (1981). “The mutual potential and gravitational torques of two bodies to fourth order”. In: *Celestial Mechanics* 24, pp. 173–181.
Segatz et al. (1988). “Tidal dissipation, surface heat flow, and figure of viscoelastic models of Io”. In: *Icarus* 75.2, pp. 187–206.
Shito, Karato, and Park (2004). “Frequency dependence of Q in Earth’s upper mantle inferred from continuous spectra of body waves”. In: *Geophysical Research Letters* 31.12.
Souchay, Mathis, and Tokieda (2013). *Tides in Astronomy and Astrophysics*. Lecture Notes in Physics. Springer.
Stachnik, Abers, and Christensen (2004). “Seismic attenuation and mantle wedge temperatures in the Alaska subduction zone”. In: *Journal of Geophysical Research: Solid Earth* 109.B10.
Tiscareno, Thomas, and Burns (2009). “The Rotation of Janus and Epimetheus”. In: *Icarus* 204, pp. 254–261.
Turcotte and Schubert (2002). *Geodynamics*. 2nd. Vol. 139. Cambridge University Press, pp. xv + 456.
Williams and Boggs (2015). “Tides on the Moon: Theory and determination of dissipation”. In: *Journal of Geophysical Research: Planets* 120.4, pp. 689–724.
Williams et al. (2001). “Lunar rotational dissipation in solid body and molten core”. In: *Journal of Geophysical Research* 106, pp. 27933–27968.
Willner et al. (2010). “Phobos control point network, rotation, and shape”. In: *Earth and Planetary Science Letters* 294.3, pp. 541–546.
Yoder (1981). “The free librations of a dissipative Moon”. In: *Philosophical Transactions of the Royal Society of London. Series A, Mathematical and Physical Sciences* 303.1477, pp. 327–338.
Zhang (1992). “Love numbers of the moon and of the terrestrial planets”. In: *Earth, Moon, and Planets* 56, pp. 193–207.

A

Tidal modelling

This appendix contains derivations for the tidal potential, tidal force and a general equation for the instantaneous deformation of gravity field coefficients. The derivation of these quantities boast relevance for the work at hand since it is insightful to see how they are related, and which approximations are applied to derive the tidal potential and tidal force that are not used in the derivation of the differential equation for the gravity field coefficients. Due to the length of these derivations, they are placed in the appendix of the thesis. Furthermore, these derivations are not novel in literature, but are not collected in one place as is done here, especially the derivation in A.3.

A.1. Tidal Potential

To derive the tide-generating potential as given in Eq. 4.1, consider again Fig. 2.4, reiterated here:

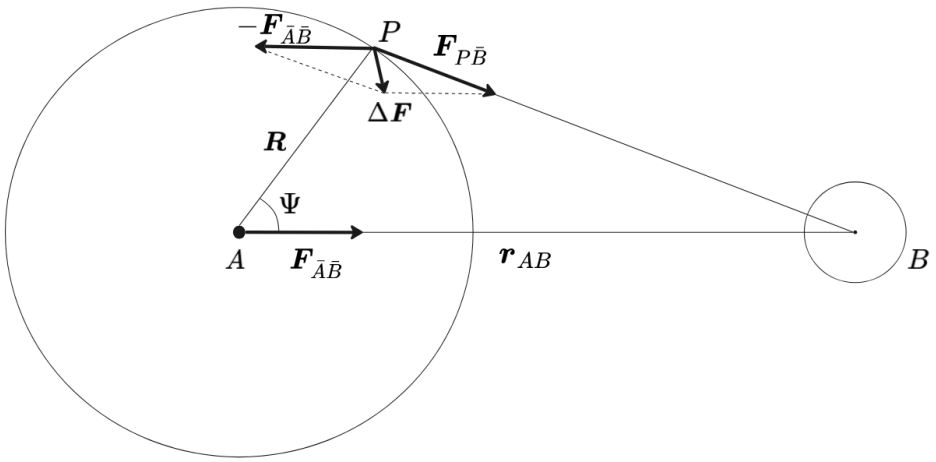

Figure A.1: Schematic decomposition of the gravitational force exerted by body B, where the difference between $\boldsymbol{F}_{P\bar{B}}$ and $\boldsymbol{F}_{\bar{A}\bar{B}}$ is responsible for the tidal force $\Delta\boldsymbol{F}$. $\boldsymbol{R}$ is the position vector pointing to point P and $\boldsymbol{r}_{AB}$ is the vector connecting the centers of A and B, and Ψ is the angle between $\boldsymbol{R}$ and $\boldsymbol{r}_{AB}$.

To derive $U_B^{'}(\boldsymbol{r})$, assume body B to be a point mass. Its potential is then given as

$$U_B(\boldsymbol{r}) = \frac{\mu_B}{r}, \tag{A.1}$$

with $r = |\boldsymbol{r}| = \sqrt{x_1^2 + x_2^2 + x_3^2}$. Taking the derivative of the gradient with respect to each component gives

$$\frac{\partial U_B}{\partial x_i} = -\frac{\mu_B}{r^3} x_i, \quad i = 1, \ldots, 3, \tag{A.2}$$

from which it is easy to see that the components of the Hessian matrix of this function is given by

$$\frac{\partial^2 U_B}{\partial x_i \partial x_j} = -3\frac{\mu_B}{r^5} x_i x_j - \delta_{ij}\frac{\mu}{r^3}, \tag{A.3}$$

where δ_{ij} is the Kronecker delta. Since U_B originates in B, $\Delta \boldsymbol{F}$ can be obtained by performing a Taylor expansion of $U_B(\boldsymbol{r})$ at the center of A, which can be found by linearizing at $x_1 = r$, $x_2 = x_3 = 0$, which is the most straightforward way of doing so. Linearization gives

$$\left.\frac{\partial^2 U}{\partial x_i \partial x_j}\right|_{\boldsymbol{r}=(r,0,0)^T} = \frac{\mu_B}{r^3}\begin{pmatrix} 2 & 0 & 0 \\ 0 & -1 & 0 \\ 0 & 0 & -1 \end{pmatrix}, \tag{A.4}$$

such that a first-order approximation of $\Delta \boldsymbol{F}$ is $\nabla U|_{\boldsymbol{r}=(r,0,0)^T}$:

$$\Delta \boldsymbol{F} = \nabla U|_{(r,0,0)^T} = \left.\frac{\partial^2 U}{\partial x_i \partial x_j}\right|_{(r,0,0)^T} \Delta \boldsymbol{x} = \frac{\mu}{r^3}\begin{pmatrix} 2 & 0 & 0 \\ 0 & -1 & 0 \\ 0 & 0 & -1 \end{pmatrix}\begin{pmatrix} \Delta x_1 \\ \Delta x_2 \\ \Delta x_3 \end{pmatrix}, \tag{A.5}$$

where $\Delta \boldsymbol{x}$ is a small displacement at the linearization point A. In order to find out the work

Since the force $\Delta \boldsymbol{F}$ can exert a force on each infinitesimal part $\mathrm{d}s$ along a direction $\bar{n}$, the required work provided by this force can be found. This work integral then yields the potential energy difference per mass, or the potential difference, which is exactly what is required in order to quantify the magnitude of the tidal potential at any point $\mathrm{d}s$ on A. To this end, it is logical then that

$$U_B^{'}(\boldsymbol{r}) = \int_{s=0}^{R} (\Delta \boldsymbol{F}, \bar{n}) ds, \tag{A.6}$$

where the implicit assumption is made that $U_B^{'}(\boldsymbol{r})$ is evaluated on a sphere with radius $R = |\boldsymbol{R}|$. $\bar{n}$ dictates the direction taken, and based on Fig. A.1 it makes sense to keep $\bar{n}$ two-dimensional and use the angle Ψ to split $\bar{n}$ into its components:

$$\bar{n} = \begin{pmatrix} \cos\psi \\ \sin\psi \\ 0 \end{pmatrix} \tag{A.7}$$

and

$$\begin{pmatrix} \Delta x_1 \\ \Delta x_2 \\ \Delta x_3 \end{pmatrix} = \begin{pmatrix} s\cos\psi \\ s\sin\psi \\ 0 \end{pmatrix} \tag{A.8}$$

with s a small displacement so that $(\Delta \boldsymbol{F}, \bar{n})$ becomes

$$\begin{aligned} (\Delta f, \bar{n}) &= \frac{\mu_B}{r_{AB}^3}\begin{pmatrix} 2s\cos\psi \\ -s\sin\psi \\ 0 \end{pmatrix} \cdot \begin{pmatrix} \cos\psi \\ \sin\psi \\ 0 \end{pmatrix} \\ &= \frac{s\mu_B}{r_{AB}^3}\left\{2\cos^2\psi - \sin^2\psi\right\} \\ &= \frac{s\mu_B}{r_{AB}^3}\left\{3\cos^2\psi - 1\right\}. \end{aligned} \tag{A.9}$$

The integral in Eq. A.6 then works out to be

$$\begin{aligned} U_B^{'}(\boldsymbol{r}) &= \int_{s=0}^{R} \frac{s\mu_B}{r_{AB}^3}\left\{3\cos^2\psi - 1\right\} ds \\ &= \frac{\mu_B R^2}{r_{AB}^3}\left\{\frac{3}{2}\cos^2\psi - \frac{1}{2}\right\} \\ &= \frac{\mu_B R^2}{r_{AB}^3} P_2(\cos\psi), \end{aligned} \tag{A.10}$$

where P_2 is the Legendre polynomial of degree 2. This is the first term of the Taylor series in question, it can be similarly shown that for degree 3 a relation exists too, for example:

$$\Delta \boldsymbol{F}_i = \frac{\partial^3 U_B}{\partial x_i \partial x_j \partial x_k} \frac{\Delta x_j \Delta x_k}{3!}, \tag{A.9}$$

where following the same method, Eq. 14.6 yields

$$U'_{B,l=3}(\boldsymbol{r}) = \frac{\mu_B R^3}{r_{AB}^4} P_3(\cos\psi). \tag{A.10}$$

By induction it follows that:

$$U'_B(\boldsymbol{r}) = \frac{\mu_B}{r_{AB}} \sum_{l=2}^{\infty} \left(\frac{R}{r_{AB}}\right)^l P_l(\cos\psi), \tag{A.11}$$

which is indeed the tidal potential of body B as given by Eq. 4.1.

A.2. Direct Tidal Force

Consider the tidal potential as introduced in Eq. 4.10, where, when the centrifugal force is left out, it reduces to

$$\delta U_A(\boldsymbol{r}, t) = \sum_{l=2}^{\infty} \left(\frac{|\boldsymbol{R}|}{|\boldsymbol{r}|}\right)^{l+1} k_l(t) * U^T_{B,l}(\boldsymbol{r}, t). \tag{A.12}$$

The direct tidal force is assumed by assuming the tidal lag to be a constant Δt, resulting in a Love distribution $k_l(t) = k_l \delta(t - \Delta t)$, which simplifies to

$$\delta U_A(\boldsymbol{r}, t) = \sum_{l=2}^{\infty} \left(\frac{|\boldsymbol{R}|}{|\boldsymbol{r}|}\right)^{l+1} k_l U^T_{B,l}(\boldsymbol{r}, t - \Delta t), \tag{A.13}$$

where the induced gravitational potential at time t is now caused by the perturbing potential of body B at time $t - \Delta t$. For clarity, it will be useful to indicate how exactly the time-dependence is related in both potentials (Mignard (1979)):

$$\delta U_A(\boldsymbol{r}, \boldsymbol{r}_{AB}(t - \Delta t)) = \sum_{l=2}^{\infty} \left(\frac{|\boldsymbol{R}|}{|\boldsymbol{r}|}\right)^{l+1} k_l U^T_{B,l}(\boldsymbol{r}, \boldsymbol{r}_{AB}(t - \Delta t)), \tag{A.14}$$

with $\boldsymbol{r}_{AB}(t-\Delta t)$ the position of the perturbing body at time $t-\Delta t$, specifically denoted by $\boldsymbol{r}_B$ instead of $\boldsymbol{r}$. Generally, Δt can be considered sufficiently small (Mignard (1980)) such that Eq. A.14 can be linearized around $\boldsymbol{r}_s(t - \Delta t)$, resulting in

$$\boldsymbol{r}_{AB}(t - \Delta t) = \boldsymbol{r}_{AB}(t) - \boldsymbol{v}_{AB}(t)\Delta t + \boldsymbol{\omega}_A \Delta t \times \boldsymbol{r}_{AB}(t), \tag{A.15}$$

where $\boldsymbol{\omega}_A$ is the angular velocity of the perturbed body, accounting for the fact that the body-fixed reference frame is rotating with angular velocity $\boldsymbol{\omega}_A$. Applying this linearization to the tidal potential in A.14 yields

$$\delta U_A(\boldsymbol{r}, \boldsymbol{r}_{AB}(t - \Delta t)) = \delta U_A(\boldsymbol{r}, \boldsymbol{r}_{AB}(t)) + \tag{A.16}$$

$$\nabla_{\boldsymbol{r}_{AB}} \delta U_A(\boldsymbol{r}, \boldsymbol{r}_{AB}(t)) \cdot (\boldsymbol{r}_{AB}(t - \Delta t) - \boldsymbol{r}_{AB}(t)) = \sum_{l=2}^{\infty} \left(\frac{R}{|\boldsymbol{r}|}\right)^{l+1} k_l W_l(\boldsymbol{R}, \boldsymbol{r}_{AB}(t)) + \tag{A.17}$$

$$\nabla_{\boldsymbol{r}_{AB}} \left[\sum_{l=2}^{\infty} \left(\frac{R}{|\boldsymbol{r}|}\right)^{l+1} k_l W_l(\boldsymbol{R}, \boldsymbol{r}_{AB}(t))\right] \cdot [(\boldsymbol{\omega}_A \times \boldsymbol{r}_{AB}(t) - \boldsymbol{v}_{AB})\Delta t]\,. \tag{A.18}$$

The gradient is worked out to be

$$\boldsymbol{\nabla}_{\boldsymbol{r}_{AB}}\delta U_A(\boldsymbol{r},\boldsymbol{r}_{AB}(t)) = \boldsymbol{\nabla}_{\boldsymbol{r}_{AB}}\sum_{l=2}^{\infty}\left(\frac{R}{|\boldsymbol{r}|}\right)^{l+1} k_l W_l(\boldsymbol{R},\boldsymbol{r}_{AB}(t)) \tag{A.19}$$

$$= -Gm_B\boldsymbol{\nabla}_{\boldsymbol{r}_{AB}}\sum_{l=2}^{\infty}\frac{k_l R^{2l+1}}{|\boldsymbol{r}|^{l+1}|\boldsymbol{r}_{AB}(t)|^{l+1}}P_l\left(\frac{\boldsymbol{r}\cdot\boldsymbol{r}_{AB}(t)}{|\boldsymbol{r}||\boldsymbol{r}_{AB}(t)|}\right) \tag{A.20}$$

$$= -Gm_B\sum_{l=2}^{\infty}\frac{k_l R^{2l+1}}{|\boldsymbol{r}|^{l+1}|\boldsymbol{r}_{AB}|^{l+1}}\Bigg[-\frac{(l+1)\boldsymbol{r}_{AB}P_l(x)}{|\boldsymbol{r}_{AB}|^2} \tag{A.21}$$

$$+\frac{dP_l}{dx}\bigg|^x\cdot\left(\frac{\boldsymbol{r}}{|\boldsymbol{r}||\boldsymbol{r}_{AB}|}-\frac{(\boldsymbol{r}\cdot\boldsymbol{r}_{AB})\boldsymbol{r}_{AB}}{|\boldsymbol{r}||\boldsymbol{r}_{AB}|^3}\right)\Bigg], \tag{A.22}$$

where for simplicity $x=\dfrac{\boldsymbol{r}\cdot\boldsymbol{r}_{\boldsymbol{AB}}}{|\boldsymbol{r}||\boldsymbol{r}_{\boldsymbol{AB}}|}$, it then follows that the tidal potential is given as

$$V_T(\boldsymbol{r},\boldsymbol{r}_{AB}(t-\Delta t)) = V_T(\boldsymbol{r},\boldsymbol{r}_{AB}(t)) - Gm_B\sum_{l=2}^{\infty}k_l\frac{R^{2l+1}}{|\boldsymbol{r}|^{l+2}|\boldsymbol{r}_{AB}|^{l+1}}\Delta t \tag{A.23}$$

$$\cdot\left[(l+1)\left(\frac{\boldsymbol{r}_{AB}\cdot\boldsymbol{v}_{AB}}{|\boldsymbol{r}_{AB}|^2}\right)|\boldsymbol{r}|P_l(x)+\frac{dP_l}{dx}\bigg|^x\right. \tag{A.24}$$

$$\left.\cdot\left(\frac{\boldsymbol{r}\cdot(\boldsymbol{\omega}_A\times\boldsymbol{r}_{AB})}{|\boldsymbol{r}_{AB}|}-\frac{\boldsymbol{r}\cdot\boldsymbol{v}_{AB}}{|\boldsymbol{r}_{AB}|}+\frac{(\boldsymbol{r}\cdot\boldsymbol{r}_{AB})(\boldsymbol{r}_{AB}\cdot\boldsymbol{v}_{AB})}{|\boldsymbol{r}_{AB}|^3}\right)\right], \tag{A.25}$$

where for simplicity time dependencies have also been removed. Finally, to find the force and consequently the torque, the gradient with respect to $\boldsymbol{r}$, and not $\boldsymbol{r}_{AB}$, has to be taken, resulting in

$$\boldsymbol{\nabla}_{\boldsymbol{r}}V_T(\boldsymbol{r},\boldsymbol{r}_{AB}(t-\Delta t)) = \boldsymbol{\nabla}_{\boldsymbol{r}}V_T(\boldsymbol{r},\boldsymbol{r}_{AB}(t)) - Gm_B\sum_{l=2}^{\infty}\Bigg(-\frac{(l+2)k_l R^{2l+1}\boldsymbol{r}}{|\boldsymbol{r}|^{l+4}|\boldsymbol{r}_{AB}|^{l+1}}\Delta t \tag{A.26}$$

$$\cdot\left[(l+1)\left(\frac{\boldsymbol{r}_{AB}\cdot\boldsymbol{v}_{AB}}{|\boldsymbol{r}_{AB}|^2}\right)P_l(x)|\boldsymbol{r}|+\frac{dP_l}{dx}\bigg|^x\cdot\left(\frac{\boldsymbol{r}\cdot(\boldsymbol{\omega}_A\times\boldsymbol{r}_{AB})}{|\boldsymbol{r}_{AB}|}-\frac{\boldsymbol{r}\cdot\boldsymbol{v}_{AB}}{|\boldsymbol{r}_{AB}|}\right.\right. \tag{A.27}$$

$$\left.\left.+\frac{(\boldsymbol{r}\cdot\boldsymbol{r}_{AB})(\boldsymbol{r}_{AB}\cdot\boldsymbol{v}_{AB})}{|\boldsymbol{r}_{AB}|^3}\right)\right]+\frac{k_l R_E^{2l+1}}{|\boldsymbol{r}|^{l+2}|\boldsymbol{r}_{AB}|^{l+1}}\Delta t \tag{A.28}$$

$$\cdot\left[(l+1)\left(\frac{\boldsymbol{r}_{AB}\cdot\boldsymbol{v}_{AB}}{|\boldsymbol{r}||\boldsymbol{r}_{AB}|^2}\right)P_l(x)+(l+1)\left(\frac{\boldsymbol{r}_{AB}\cdot\boldsymbol{v}_{AB}}{|\boldsymbol{r}_{AB}|^2}\right)|\boldsymbol{r}|\frac{dP_l}{dx}\bigg|^x\right. \tag{A.29}$$

$$\cdot\left(\frac{\boldsymbol{r}_{AB}}{|\boldsymbol{r}||\boldsymbol{r}_{AB}|}-\frac{(\boldsymbol{r}\cdot\boldsymbol{r}_{AB})\boldsymbol{r}}{|\boldsymbol{r}|^3|\boldsymbol{r}_{AB}|}\right)+\frac{d^2P_l}{dx^2}\bigg|^x \tag{A.30}$$

$$\cdot\left(\frac{\boldsymbol{r}_{AB}}{|\boldsymbol{r}||\boldsymbol{r}_{AB}|}-\frac{(\boldsymbol{r}\cdot\boldsymbol{r}_{AB})\boldsymbol{r}}{|\boldsymbol{r}|^3|\boldsymbol{r}_{AB}|}\right)\cdot\left(\frac{\boldsymbol{r}\cdot(\omega_A\times\boldsymbol{r}_{AB}}{|\boldsymbol{r}_{AB}|}-\frac{\boldsymbol{r}\cdot\boldsymbol{v}_{AB}}{|\boldsymbol{r}_{AB}|}+\frac{(\boldsymbol{r}\cdot\boldsymbol{r}_{AB})(\boldsymbol{r}_{AB}\cdot\boldsymbol{v}_{AB})}{|\boldsymbol{r}_{AB}|^3}\right) \tag{A.31}$$

$$\left.+\frac{dP_l^x}{dx}\cdot\left(\frac{\boldsymbol{\omega}_A\times\boldsymbol{r}_{AB}}{|\boldsymbol{r}_{AB}|}-\frac{\boldsymbol{v}_{AB}}{|\boldsymbol{r}_{AB}|}+\frac{\boldsymbol{r}_{AB}(\boldsymbol{r}_{AB}\cdot\boldsymbol{v}_{AB})}{|\boldsymbol{r}_{AB}|^3}\right)\right]\Bigg). \tag{A.32}$$

Note that, as discussed in Section 4.2, the force is evaluated at $\boldsymbol{r}=\boldsymbol{r}_{\boldsymbol{AB}}$, implying that $x=1$ and thus $P_l(1)=1$, which follows as a standardization condition, furthermore $\dfrac{dP_l}{dx}\bigg|^1=\dfrac{l(l+1)}{2}$. Under these conditions, the force results into

$$
\begin{aligned}
F_T &= -m_B \nabla_r \delta U(\boldsymbol{r}, \boldsymbol{r}_{AB}(t-\Delta t)) \\
&= G(m_B)^2 \sum_{l=2}^{\infty} \frac{k_l (R)^{2l+1}}{|\boldsymbol{r}|^{2l+4}} \cdot \left(-(l+1)\boldsymbol{r} + \frac{l(l+1)}{2}(\boldsymbol{r}-\boldsymbol{r}) \right) \\
&\quad + G(m_B)^2 \sum_{l=2}^{\infty} \{ - \left(\frac{(l+2) k_2 (R)^{2l+1} \boldsymbol{r}}{|\boldsymbol{r}|^{2l+5}} \Delta t \cdot \left[\frac{(l+1)}{2} \frac{(\boldsymbol{r}\cdot\boldsymbol{v})}{|\boldsymbol{r}|} + \frac{l(l+1)}{2} \cdot \left(0 - \frac{\boldsymbol{r}\cdot\boldsymbol{v}}{|\boldsymbol{r}|} + \frac{\boldsymbol{r}\cdot\boldsymbol{v}}{|\boldsymbol{r}|} \right) \right] \right\} \\
&\quad + \frac{k_l (R)^{2l+1}}{|\boldsymbol{r}|^{2l+4}} \Delta t \cdot \left[\frac{(l+1)(\boldsymbol{r}\cdot\boldsymbol{v})\boldsymbol{r}}{|\boldsymbol{r}|^2} + (l+1)(\boldsymbol{r}\cdot\boldsymbol{v}) \frac{l(l+1)}{2} \cdot \left(\frac{\boldsymbol{r}-\boldsymbol{r}}{|\boldsymbol{r}|^2} \right) \right] \\
&\quad + \frac{d^2 P_l}{dx^2} \Big|^1 \cdot \left\{ \frac{\boldsymbol{r}}{|\boldsymbol{r}|} - \frac{\boldsymbol{r}}{|\boldsymbol{r}|} \right\} \cdot \left(0 - \frac{\boldsymbol{r}\cdot\boldsymbol{v}}{|\boldsymbol{r}|} + \frac{\boldsymbol{r}\cdot\boldsymbol{v}}{|\boldsymbol{r}|} \right) + \frac{l(l+1)}{2} \cdot \left(\boldsymbol{\omega_c} \times \boldsymbol{r} - \boldsymbol{v} + \frac{\boldsymbol{r}(\boldsymbol{r}\cdot\boldsymbol{v})}{|\boldsymbol{r}|^2} \right) \\
&= -G(m_B)^2 \sum_{l=2}^{\infty} \frac{k_l (R)^{2l+1}}{|\boldsymbol{r}|^{2l+4}} \cdot (l+1)\boldsymbol{r} - G(m_B)^2 \sum_{l=2}^{\infty} \left(\frac{(l+2) k_l (R)^{2l+1}}{|\boldsymbol{r}|^{2l+4}} \Delta t \cdot \left(\frac{(l+1)(\boldsymbol{r}\cdot\boldsymbol{v})}{|\boldsymbol{r}|^2} \right) \right. \\
&\quad \left. - \frac{k_l (R)^{2l+1}}{|\boldsymbol{r}|^{2l+4}} \Delta t \cdot \left[\frac{(l+1)(\boldsymbol{r}\cdot\boldsymbol{v})\boldsymbol{r}}{|\boldsymbol{r}|^2} + \frac{l(l+1)}{2} \cdot \left(\boldsymbol{\omega_c} \times \boldsymbol{r} - \boldsymbol{v} + \frac{\boldsymbol{r}(\boldsymbol{r}\cdot\boldsymbol{v})}{|\boldsymbol{r}|^2} \right) \right] \right) \\
&= -G(m_B)^2 \sum_{l=2}^{\infty} \frac{k_l (R)^{2l+1}}{|\boldsymbol{r}|^{2l+4}} \cdot (l+1) \left[\boldsymbol{r} + \Delta t \left(\frac{(l+2)(\boldsymbol{r}\cdot\boldsymbol{v})}{|\boldsymbol{r}|^2} - \frac{\boldsymbol{r}(\boldsymbol{r}\cdot\boldsymbol{v})}{|\boldsymbol{r}|^2} - \frac{l}{2} \frac{(\boldsymbol{r}\cdot\boldsymbol{v})}{|\boldsymbol{r}|^2} - \frac{l}{2}(-\boldsymbol{r} \times \omega_c - \boldsymbol{v}) \right) \right] \\
&= -G(m_B)^2 \sum_{l=2}^{\infty} \left[(l+1) \frac{k_l (R)^{2l+1}}{|\boldsymbol{r}|^{2l+4}} \left(\boldsymbol{r} + \Delta t \left(\frac{l}{2}(\boldsymbol{r} \times \boldsymbol{\omega_c} + \boldsymbol{v}) + \frac{l+2}{2} \frac{(\boldsymbol{r}\cdot\boldsymbol{v})\boldsymbol{r}}{|\boldsymbol{r}|^2} \right) \right) \right],
\end{aligned}
$$

which agrees with literature (Mignard (1980)). As mentioned before in Section 4.2, it is common to truncate to degree $l = 2$ (e.g., Lari 2018), which then yields

$$
\boldsymbol{F}_T = -\frac{3 G m_A k_2^B R_E^5}{|\boldsymbol{r}_{AB}|^8} \left(r + \Delta t \left(\boldsymbol{r}_{AB} \times \boldsymbol{\omega}_B + \boldsymbol{v}_A + \frac{2}{|\boldsymbol{r}_{AB}|^2} (\boldsymbol{r}_{AB} \cdot \boldsymbol{v}_A) \boldsymbol{r}_{AB} \right) \right). \tag{A.33}
$$

A.3. Gravity field coefficients' instantaneous deformation

Correia et al. (2014) and Boué et al. (2016) mention that the differential equation for the gravity field coefficients as given by Eq. 5.14 can be written in a convolution such that

$$
\delta U_A(\boldsymbol{r}, t) = k(t) * U_B^T(\boldsymbol{r}, t), \tag{A.34}
$$

where the function is assumed to be evaluated at the surface and the centrifugal potential is left out. Transforming into the Fourier domain yields a point-wise multiplication:

$$
\delta U_A(\boldsymbol{r}, \omega) = k(\omega) \cdot U_B^T(\boldsymbol{r}, \omega), \tag{A.35}
$$

with ω the frequency. Note on the other hand that Correia et al. (2014) derives a relation between the induced gravitational potential and a perturbing potential:

$$
U_l^T + \tau_l \dot{U}_l^T = U_l^{T,e} + \tau_e \dot{U}_l^{T,e}, \tag{A.36}
$$

where this equation holds for each of the gravity field coefficients. Using the substitution in Eq. 5.13 it then follows that

$$
Z_{l,m} + \tau_l \dot{Z}_{l,m} = Z_{l,m}^e + \tau_e \dot{Z}_{l,m}^e. \tag{A.37}
$$

Where the Δ is left out and the degree l and order m will be left out for convenience. Note also that both Z and Z^e depend on time, but for convenience that will be left out at times. The homogeneous part solves to be $Z(t) = Z(0)\exp^{-t/\tau}$. The particular solution can be found as

$$e^{t/\tau}(Z + \tau_l \dot{Z}) = e^{t/\tau}(Z^e + \tau_e \dot{Z}^e) \tag{A.38}$$

$$=> \frac{d}{dt}(e^{t/\tau} Z(t)) = e^{t/\tau}(Z^e + \tau_e \dot{Z}^e). \tag{A.39}$$

Integrating this expression from 0 to t then yields

$$\int_0^t \frac{d}{dt'}(e^{t'/\tau} Z(t'))dt' = \int_0^t e^{t'/\tau}(Z^e + \tau_e \dot{Z}^e)dt' \tag{A.40}$$

$$=> e^{t/\tau} Z(t) = Z(0) + \frac{1}{\tau}\int_0^t e^{t'/\tau} Z^e(t')dt' + \frac{\tau_e}{\tau}\int_0^t e^{t'/\tau}\dot{Z}^e dt'. \tag{A.41}$$

The second integral can be partially integrated:

$$\frac{\tau_e}{\tau}\int_0^t e^{t'/\tau}\dot{Z}^e dt' = \frac{\tau_e}{\tau}\left[\left[e^{t'/\tau} Z^e(t')\right]_0^t - \frac{1}{\tau}\int_0^t e^{t'/\tau} Z^e(t')dt'\right], \tag{A.42}$$

filling this back in to Eq. A.41 gives

$$e^{t/\tau} Z(t) = Z(0) + \frac{1}{\tau}\int_0^t e^{t'/\tau} Z^e(t')dt' + \frac{\tau_e}{\tau} e^{t/\tau} Z^e(t) - \frac{\tau_e}{\tau} Z^e(0) - \frac{\tau_e}{\tau}\frac{1}{\tau}\int_0^t e^{t'/\tau} Z^e(t')dt' \tag{A.43}$$

$$=> Z(t) = \left(Z(0) - \frac{\tau_e}{\tau} Z^e(0)\right) e^{-t/\tau} + \frac{\tau_e}{\tau} Z^e(t) + \frac{1}{\tau}\left(1 - \frac{\tau_e}{\tau}\right)\int_0^t e^{(t'-t)/\tau} Z^e(t')dt', \tag{A.44}$$

where $Z(0) - \frac{\tau_e}{\tau} Z^e(0)$ will be called C (Correia et al. (2014)):

$$Z(t) = Ce^{-t/\tau} + \frac{\tau_e}{\tau} Z^e(t) + \frac{1}{\tau}\left(1 - \frac{\tau_e}{\tau}\right)\int_0^t e^{(t'-t)/\tau} Z^e(t')dt'. \tag{A.45}$$

The first term is the so-called transient mode and rapidly decays to zero with time. In a converged state this value can be neglected. In order to find a solution to Eq. A.45, an eigenfunction expansion of $Z^e(t)$ can be used, a method commonly used to solve differential equations. Generally, this involves assuming that the solution of $Z^e(t)$ is of the form $\sum_k \beta_k f_k(t)$. For gravity field coefficients, it may be a reasonable assumption to assume that the equilibrium solutions will have a periodic-like behaviour (Correia et al. (2014)), from which it then follows that the solution can be specified more: $Z^e(t) = \sum_k \beta_k e^{i\omega_k t}$, with ω_k a numerable set of frequencies. Plugging this into Eq. A.45 gives

$$Z(t) = Ce^{-t/\tau} + \frac{\tau_e}{\tau}\sum_k \beta_k e^{i\omega_k t} + \frac{1}{\tau}\left(1 - \frac{\tau_e}{\tau}\right)\int_0^t e^{(t'-t)/\tau}\sum_k \beta_k e^{i\omega_k t'} dt' \tag{A.46}$$

$$=> Z(t) = Ce^{-t/\tau} + \frac{\tau_e}{\tau}\sum_k \beta_k e^{i\omega_k t} + \frac{1}{\tau}\left(1 - \frac{\tau_e}{\tau}\right)\sum_k \beta_k e^{-t/\tau}\left[\frac{1}{i\omega_k + 1/\tau} e^{(i\omega_k + 1/\tau)t} - \frac{1}{i\omega_k + 1/\tau}\right], \tag{A.47}$$

where the third term can be simplified as

$$\frac{1}{\tau}\left(1 - \frac{\tau_e}{\tau}\right)\sum_k \beta_k e^{-t/\tau}\left[\frac{1}{i\omega_k + 1/\tau} e^{(i\omega_k + 1/\tau)t} - \frac{1}{i\omega_k + 1/\tau}\right] \tag{A.48}$$

$$= \sum_k \beta_k e^{-t/\tau}\left[\left(\frac{\tau - \tau_e}{\tau + i\omega_k \tau^2}\right) e^{(i\omega_k + 1/\tau)t} + \frac{\tau - \tau_e}{\tau + i\omega_k \tau^2}\right] \tag{A.49}$$

and thus

$$Z(t) = \sum_k \beta_k \left[\frac{\tau_e}{\tau} e^{i\omega_k t} + e^{-t/\tau} \left[\left(\frac{\tau - \tau_e}{\tau + i\omega_k \tau^2} \right) e^{(i\omega_k + 1/\tau)t} + \frac{\tau - \tau_e}{\tau + i\omega_k \tau^2} \right] \right] + Ce^{-t/\tau} \tag{A.50}$$

$$=> Z(t) = \sum_k \beta_k \left[\left(\frac{\tau_e}{\tau} + \left(\frac{\tau - \tau_e}{\tau + i\omega_k \tau^2} \right) e^{i\omega_k t} \right) \right] + \left(\sum_k \beta_k \frac{\tau - \tau_e}{\tau + i\omega_k \tau^2} + C \right) e^{-t/\tau} \tag{A.51}$$

$$=> Z(t) = \sum_k \beta_k \frac{1 + i\tau_e \omega_k}{1 + i\tau\omega_k} e^{i\omega_k t} + Ce^{-t/\tau}. \tag{A.52}$$

Note here that the pre-factor $\frac{1 + i\tau_e \omega_k}{1 + i\tau\omega_k}$ is synonymous to the Fourier transform of the Love distribution in case of a Maxwell rheology (e.g., Henning et al. 2009):

$$k_l(\nu) = k_l^0 \frac{1 + i\tau_e \nu}{1 + i\tau_l \nu}, \tag{A.53}$$

where this expression is now similar to Eq. A.35 but not entirely identical, since this expression still holds in the time-domain. It is at this point where Correia et al. (2014) and Boué et al. (2016) make use of the 'correspondence principle' for viscoelastic bodies as described by for example Efroimsky (2012), stating that the expression for the external gravitational potential when not static (e.g. induced variations due to gravity field deformations), Eq. A.34 can be tranformed into Eq. A.35 even for a point-wise multiplication in the time-domain. In that case, it is likely that similar reasoning is applied to Eq. A.52, since the variations in the gravitational potential can be decomposed into variations in the gravity field coefficients. Boué et al. (2016) seems to this line of reasoning to transform the convolution in his Eq. 4 into a differential equation as in Eq. 6, also by taking into account that $Ce^{-t/\tau}$ will rapidly decay, but an exact reproduction has unfortunately not be made.

B

Integrator selection

To achieve the goals laid out in this work, choosing a suitable integrator is imperative. From literature, it is clear that the effects of tides are extremely small, and the coupling effects will be even smaller, and thus integrator restrictions are tight on this problem. In order to get an idea of what the order of integrator error must be, the magnitude of the smallest effect that must be measured should be quantified first, which is the coupling between a body's tidal, rotational and translational equations of motion. This has been done in the following way.

The uncoupled and coupled model have both been propagated for 5000 days for the tides raised on the Earth by the Moon with the exact same initial state, which has been obtained after applying the damping algorithm described in Appendix D of the research paper. The difference in position between these two models is subsequently taken and the norm of this difference is projected in Fig. C.5a.

Over the roughly 13 years and 8 months of propagation, the position difference accumulates up to $\sim$ 20 m which, by all accounts, is a tight constraint. Note that the semi-major axis of the Moon is roughly 384000 km, about 8 orders of magnitude larger. A suitable integrator will have an error 3-4 orders below this error, so roughly in the order of $10^{-2} - 10^{-1}$ m over the same period. A more realistic period is shown in Fig. C.5b, with the error growing to around 10^{0} m, and hence the integrator error requirements being in the order of $10^{-4} - 10^{-3}$ m over this period.

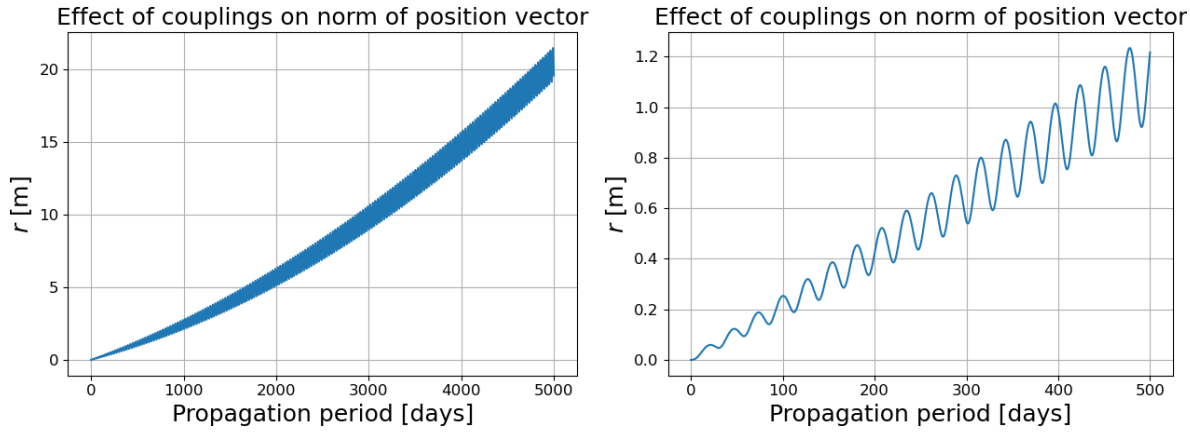

(a) Coupling effects over 13 years and 8 months.

(b) Coupling effects over 1 year and 5 months.

Figure B.1: Coupling effects.

Tudat, and similar astrodynamics packages, are commonly used within the field of propagation. However, since no models exist that can concurrently integrate the translational, rotational and tidal dynamics, this has been built from scratch for this work. The integrator could similarly be built from scratch to enable a wide range of choices, but since this is a time-consuming task prone to mistakes, the choice has been made to make use of existing integrators available in the SciPy package. SciPy

primarily provides the following relevant integrators applicable to the problem at hand: RK23, RK45 and DOP853. Based on previous experience, RK23 and RK45 are disregarded for the task at hand, as their accuracy is generally not sufficient for the requirements laid out for the task at hand. DOP853 is an explicit Runge-Kutta integrator of order 8 and hence its error will be lower than for the other two integrators. A downside is that this method is computationally more expensive. For the DOP853 integrator, a range of step sizes are compared to a nominal propagation using Tudat, with settings mentioned before. A fixed step-size is preferred over variable step-size to ensure consistent and uniform output of results. The results are displayed in Fig. B.2.

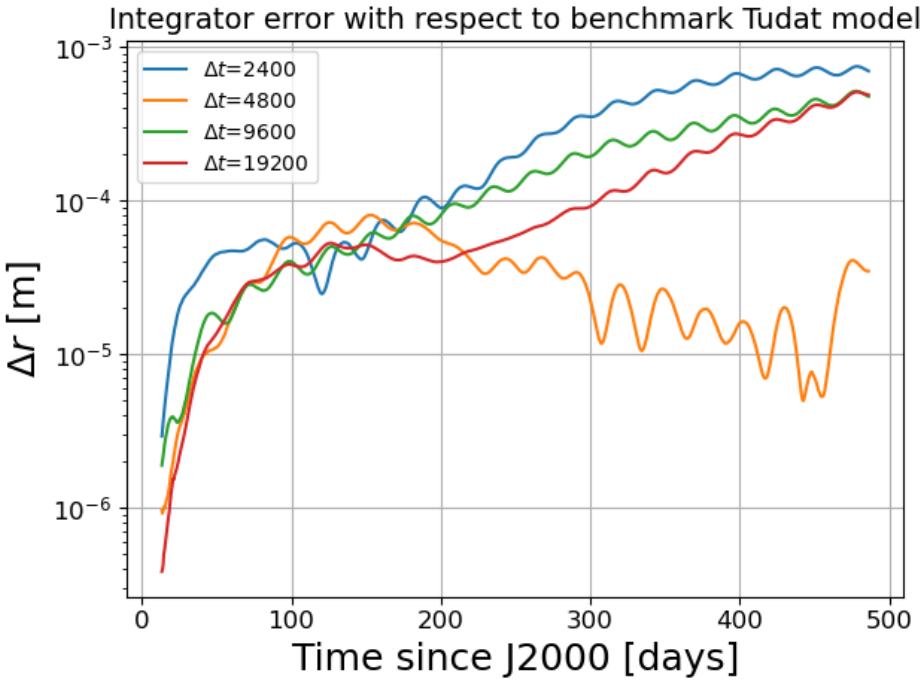

Figure B.2: Integrator error as a function of time for various step-sizes.

For an 8th order integrator, the general expected behaviour of the error would be that as the step-size doubles, the error increases with 2^8, or roughly two orders of magnitude. Surprisingly, this behaviour is not observed, and it is unclear why this is the case. Rather, the errors seem to increase almost identically, with the exception of the step size $\Delta t = 4800$ s. Based on this figure, the other 3 step sizes fulfill the integrator accuracy requirement. When they are equal, another constraint is placed: the step size is preferred to not be *too* large, simply in order to avoid the need of interpolating too much data during the data analysis of the obtained data. To this end, the step size $\Delta t = 9600$ s is chosen as integrator for this thesis.

C

Verification

This section will explain how the software developed for this work has been verified. The verification of the software can be divided into three parts: the translational dynamics, the rotational dynamics and the tidal dynamics. All three of these components will be compared with the existing software of Tudat. All Tudat features - translational and rotational propagation - are assumed to work correctly, as the software is developed by a professional community, and has been extensively tested and extensively used.

This work has made use of two models: an uncoupled model and a coupled model, where both models concurrently propagate the translational and rotational dynamics, but the uncoupled model expresses the influence of tides through the tidal force while the coupled model also concurrently propagates a differential equation for the gravity field coefficients. Both models have been implemented. Specifically, the uncoupled model is implemented using Eq. 34, 35, 15, 16, 17. The coupled model is implemented using Eq. 34-36. Since these equations have been implemented by the author from scratch, including the propagator, they are prone to mistakes and thus need to be tested against test cases to verify their implementation. The focus of this appendix lies in the comparison between the uncoupled model and Tudat, which has not been done yet. Note that the coupled model cannot be directly verified against a similar coupled implementation in Tudat, as that does not exist yet. For propagations of the uncoupled model, a DOP583 integrator is used with a fixed step-size of 80 minutes. For propagations with Tudat, a fixed RKF8 integrator (i.e. an RKF7(8) integrator with an eight order coefficient set) is used with a fixed step size of 20 minutes.

A large part of the verification and validation of the tides in the coupled model has been performed in the stand-alone research paper by analysing related parameters, such as the orbital evolution parameters and the gravity field coefficients in Chapter 4. The results displayed there are in good accordance with the uncoupled model and simplified approximations found in literature, adding confidence in that the coupled model has been implemented correctly. For a truly comprehensive test, the coupled model would be verified against a similar coupled implementation, but that is currently not yet available. Despite the tests not being comprehensive, the results in the main body of the stand-alone paper are a good indicator of the correct working of the model.

In this section, the translational dynamics of the uncoupled model will be verified in section C.1, the rotational dynamics of the uncoupled model will be verified in section C.2 and the effect of tides in the uncoupled model will be verified in section C.3.

C.1. Translational dynamics

The propagation of the translational dynamics will be compared to Tudat's implementation, where both will be propagated with an identical initial state. This will initially be done for the Earth and Moon both modelled as a point mass, and subsequently for the Moon extended to a degree and order 2/2 gravity field. The comparisons will be made in the cartesian state and the keplerian state.

The results for the point mass propagation are displayed in Fig. C.1a-d, where the difference between the uncoupled model's results and Tudat's results are displayed over a propagation period of one day. The differences in position components - Fig. C.1a - are in the order of numerical error, as the

position vector between the Earth and the Moon is in the order of 10^8 m. Similarly, the remaining Keplerian elements also are in the order of numerical error, with all of them being differences approximately 14 order of magnitude smaller than their nominal values. This verifies that the implemented equation of motion, along with the integrator used to integrate the equations of motion, behave as expected (i.e. the results are in agreement with Tudat up to numerical errors).

Secondly, the extended gravitational acceleration can now be verified. Extending the gravity field up to D/O 2/2 results in additional accelerations as described in Eq. 2.6 of the Literature Study in chapter 2. Implementing a D/O 2/2 gravity field and comparing the difference with Tudat's implementation of a D/O 2/2 gravity field results in the differences in FIg. C.1e-f. Note that similar to the previous scenario, differences between the uncoupled model and Tudat remain at the numerical level for the investigated quantities and does not substantially increase upon introduction of an extended gravity field. This verifies the translational equations of motion.

A second step to verifying a correct implementation of the translational equations of motion is to verify it also results in a physically scenario and does not result in the orbit blowing up. It will be useful to plot the evolution of the orbit and Kepler elements over time. The goal of this analysis is to verify that the Moon approximately follows a realistic orbit (i.e., Kepler elements close to its nominal values).

The top and side view of the orbit are displayed in Fig. C.2. At a first view, the orbit indeed has a relatively low eccentricity and inclination. A more detailed insight is gained from the Kepler elements displayed in Fig. C.3, which shows the orbit's semi-major axis and eccentricity oscillating around nominal values of $a = 381874$ km and $e = 0.06314$. Offsets still exist, as these plots are created with a very specific dynamical model with a limited gravity field and no perturbations considered, hence values for these quantities in literature may vary somewhat.

This work also considers third-body perturbations. Naturally, this piece of the software must also be validated and will be compared against Tudat. Similar to Fig. C.1, the position and Kepler elements will be used to measure the differene between the uncoupled model's results and Tudat's results. For the implementation of third body perturbations, the third bodies are assumed to be point masses acting only on the point mass of the propagated body as mentioned in the stand-alone paper in Chapter 3. Fig. C.4 shows that when perturbations are included, the error in all investigated quantities remains in the order of numerical errors, similar to Fig. C.1, hence verifying that perturbations have been added correctly to the translational equations of motion.

C.2. Rotational dynamics

In order to verify the rotational dynamics of the system, the translational and rotational states are concurrently integrated. Similar to the previous section, the Kepler elements can be analyzed to verify the software. Just like for the translational dynamics, the difference between Tudat and the uncoupled model is in the order of numerical errors. In addition, the angular velocity and quaternion vector can be analyzed, of which the results are displayed in Fig. C.2. The difference in the angular velocity is in the order of numerical error, while the same seems to hold for the quaternion vector. For the quaternion vector, there might be small differences due to different normalization conditions applied to the quaternion between Tudat and the uncoupled model. For convenience, the normalization conditions are gathered below in Eq. C.1 as a reminder:

$$\sum_{i=0}^{3} q_i^2 = 1, \tag{C.1}$$

with q_i the Euler parameters as introduced in section 2.2.2. of the Literature Study included in chapter 2.

This verifies the proper functioning of the coupled translational-rotational system. Note that this strictly verifies the underlying physics of the system, but does not necessarily verify that the system at hand is a realistic system (i.e. the orbit does not blow up, the normal modes are damped). In order to gain more confidence that it is, it is useful to visualize the orbit and orientation of the Moon through analyzing the Earth's position in the Moon's sky.

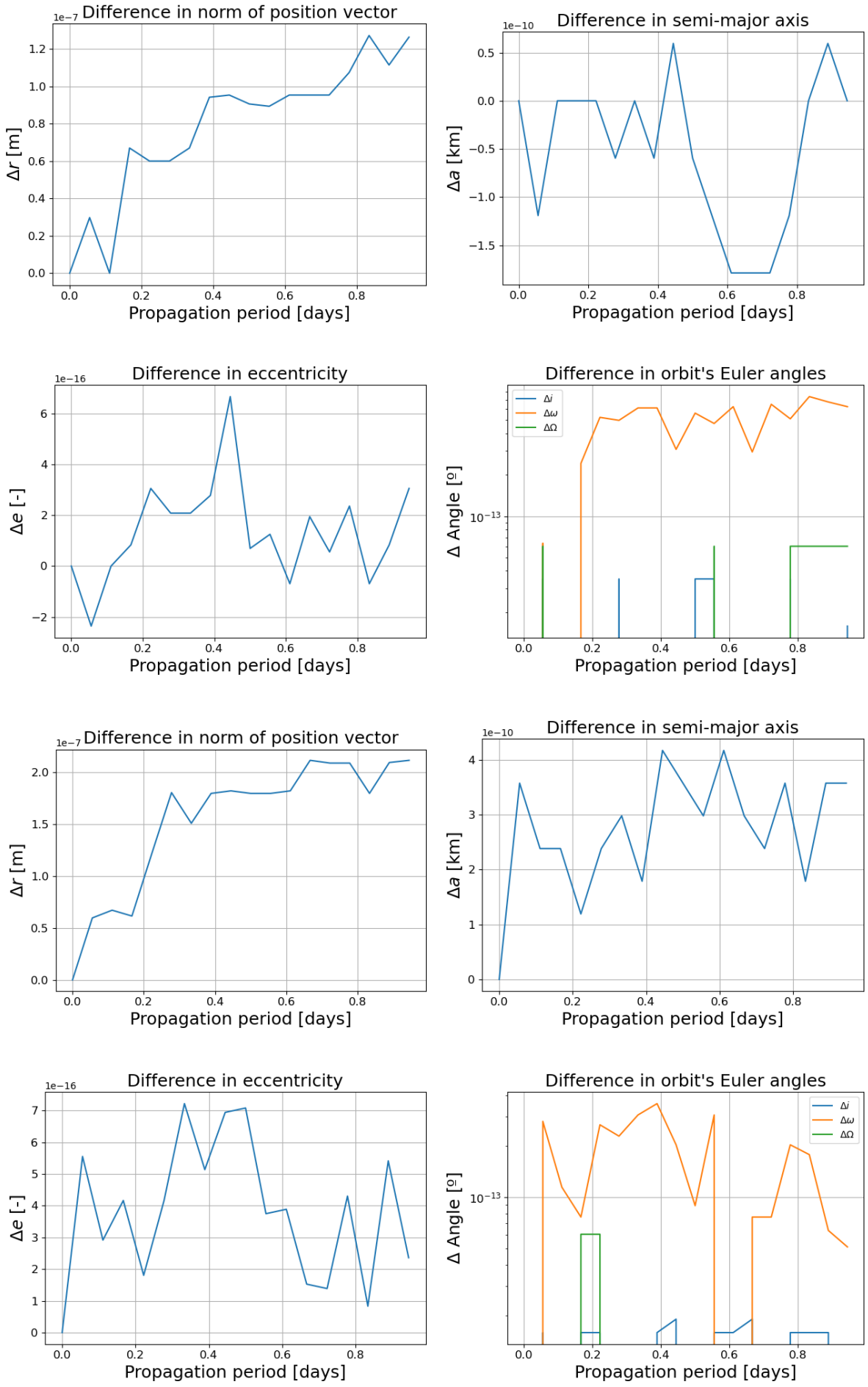

Figure C.1: Verification of the point mass and extended body dynamics by comparing the software created in this work with Tudat. Figures C.1a-C.1d show the verification for a point mass acceleration, while Figures C.1e-C.1h show the same for the accelerations exerted by a body with a gravity field extended to D/O 2/2.

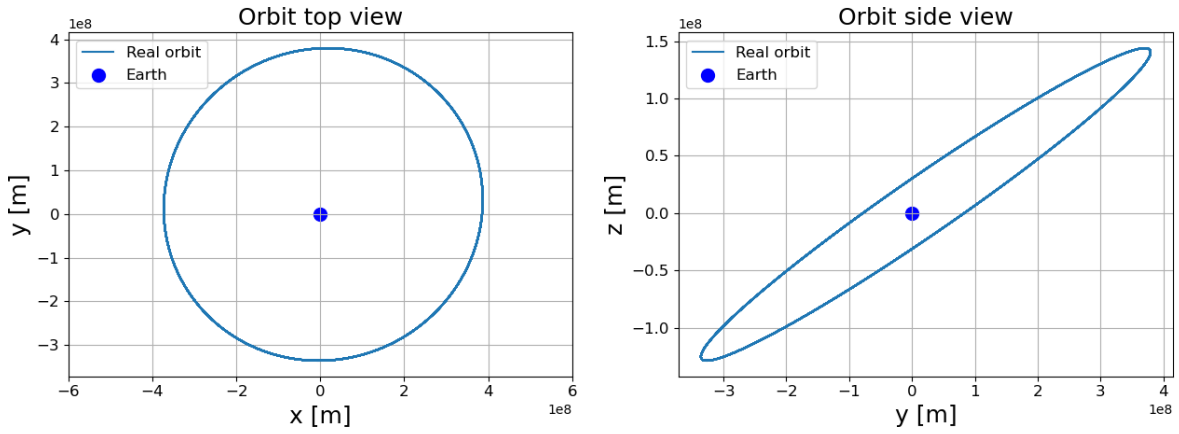

(a) Top view of the orbit

(b) Side view of the orbit

Figure C.2: Orbit visualization. This does not give quantitative information, but does qualitatively confirm that nothing weird happens with the orbit, and the physics generally behave as expected.

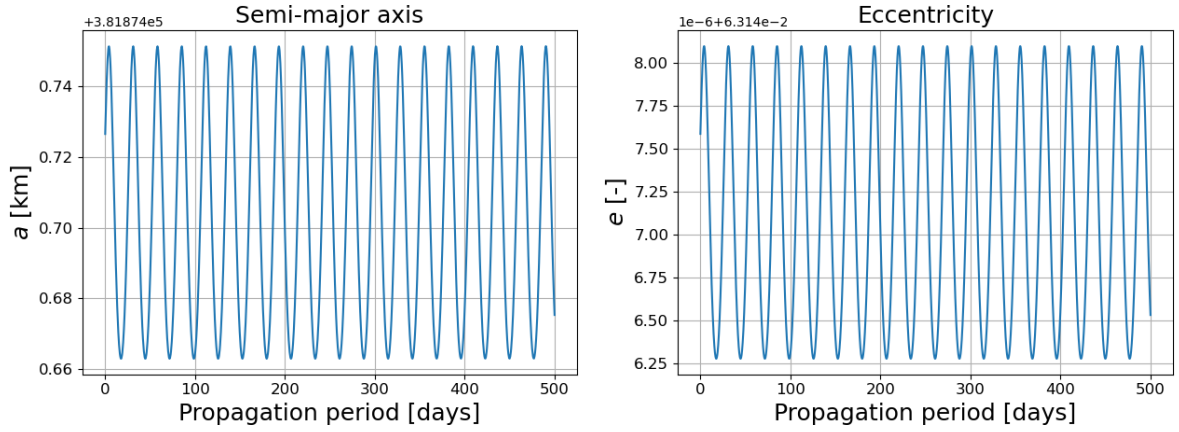

(a) Semi-major axis over time

(b) Eccentricity over time

Figure C.3: Keplerian elements over time. Once-per-orbit variations are presented due to the gravity field coefficients of degree 2.

C.3. Tidal dynamics

The validation and verification of the influence of tides on the dynamics of planetary systems has been performed mainly in the research paper in Chapter 3. The uncoupled and coupled model both produce good estimates of the secular evolution of the semi-major axis and eccentricity of the Moon compared to approximations from literature, implying that the influence of tidal effects likely has been incorporated correctly into the dynamics.

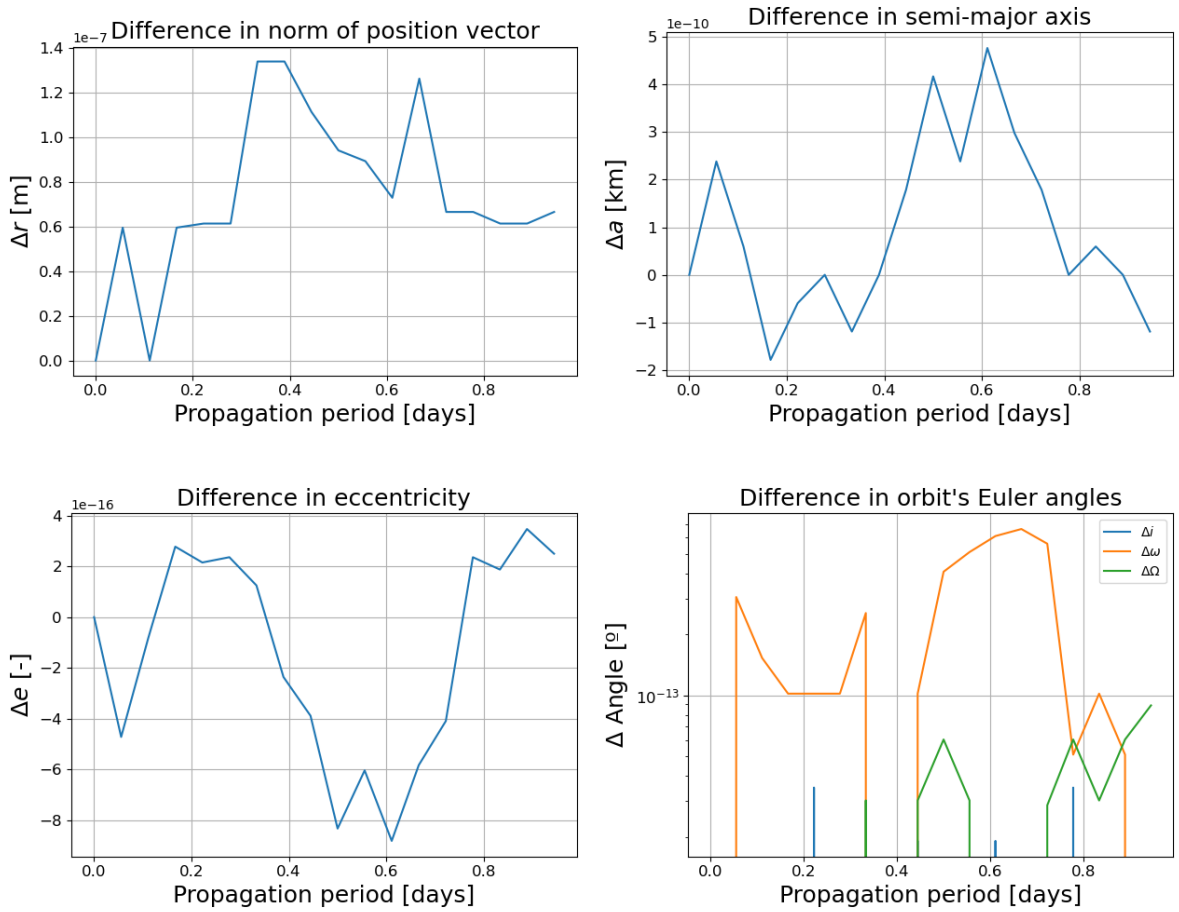

Figure C.4: Verification of the translational dynamics including perturbations by comparing the software created in this work with Tudat. The differences in the investigated quantities remain in the order of numerical errors.

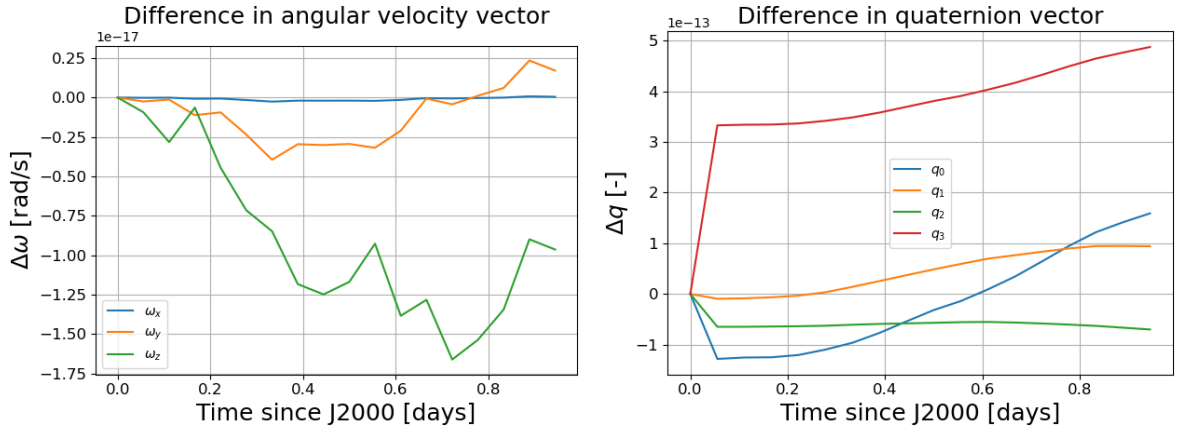

(a) Difference in the angular velocity vector.

(b) Difference in the quaternion vector.

Figure C.5: Difference between the created software and Tudat for a coupled translational-rotational propagation. The rotational state vector is compared and the differences remain at the order of numerical errors, validating the software.